Investigating the role of extended emission in Galactic compact and ultracompact H II regions

A thesis submitted

in partial fulfillment for the award of the degree of

Doctor of Philosophy

by

Jyotirmoy Dey

Department of Earth and Space Sciences
Indian Institute of Space Science and Technology
Thiruvananthapuram, India

February 2025

Certificate

This is to certify that the thesis titled ***Investigating the role of extended emission in Galactic compact and ultracompact H II regions*** submitted by **Jyotirmoy Dey**, to the Indian Institute of Space Science and Technology, Thiruvananthapuram, in partial fulfillment for the award of the degree of **Doctor of Philosophy** is a bona fide record of the original work carried out by him/her under my supervision. The contents of this thesis, in full or in parts, have not been submitted to any other Institute or University for the award of any degree or diploma.

Prof. Jagadheep D. Pandian
Professor
Department of Earth & Space Sciences

Prof. Anand Narayanan
Professor & Head
Department of Earth & Space Sciences

Place: IIST Thiruvananthapuram
Date: February 2025

Declaration

I declare that this thesis titled ***Investigating the role of extended emission in Galactic compact and ultracompact H II regions*** submitted in partial fulfillment for the award of the degree of **Doctor of Philosophy** is a record of the original work carried out by me under the supervision of **Prof. Jagadheep D. Pandian**, and has not formed the basis for the award of any degree, diploma, associateship, fellowship, or other titles in this or any other Institution or University of higher learning. In keeping with the ethical practice in reporting scientific information, due acknowledgments have been made wherever the findings of others have been cited.

Place: IIST Thiruvananthapuram
Date: February 2025

Jyotirmoy Dey
(SC18D051)

To the loving memory of my father...

Acknowledgements

At the end of this long journey, I would like to express my deepest gratitude to everyone who supported me and made my life easier during this period.

First and foremost, I would like to thank my advisor, Prof. Jagadheep D. Pandian, for his guidance, patience, and encouragement throughout this journey. His profound knowledge and deep intellect on topics related to this thesis have immensely helped me to carry out this research. Prof. Pandian's constant push toward accomplishing the goals of this project kept me motivated, especially during the uncertain times of this venture.

I am grateful to the members of my doctoral committee, Prof. Anandmayee Tej, Prof. Samir Mandal, and Prof. Naveen Surendran, for their insightful feedback and suggestions, which helped to improve the quality of this research.

I am deeply appreciative of the financial support provided by the Max Planck Society through their 'Max Planck Partner Groups with foreign institutions' initiative.

Many thanks to Prof. Dharam Vir Lal, Prof. C. H. Iswara Chandra, and Prof. Ruta Kale from the NCRA-TIFR, Pune, whose technical expertise and advice regarding radio data calibration and imaging were invaluable to my research.

I sincerely thank the present Director of IIST, Prof. Dipankar Banerjee, as well as the past Directors, Dr. V. K. Dadhwal, Dr. S. Somanath, Dr. D Sam Dayala Dev, and Dr. S Unnikrishnan Nair, for providing the necessary facilities for my research. I am also grateful to the present and past Registrars, Prof. Kuruvilla Joseph and Dr. Y. V. N. Krishna Murthy, as well as the Deans, Prof. A. Chandrasekar, Prof. Raju K. George, and Prof. Kuruvilla Joseph, for their support. I extend my appreciation to the administrative, library, hostel, canteen, and technical staff members of IIST for their assistance whenever needed. I am deeply grateful to the present and past Heads of the Earth and Space Sciences Department—Prof. Anand Narayanan, Prof. Rama Rao Nidamanuri, Prof. Samir Mandal, and Prof. Anandmayee Tej—as well as the faculty members, including Prof. Anandmayee Tej, Prof. Samir Mandal, Prof. Sarita Vig, Prof. Anand Narayanan, Dr. Resmi Lekshmi, and Dr. Vikram Khaire, for their guidance and support. Additionally, I appreciate the efforts of the department's office staff in handling official matters. Finally, I would like to thank the present Astronomy & Astrophysics lab instructor, Jinu Godwin, and the past instructor, Sai Krishnan, for their valuable assistance.

I also express my gratitude to the staff members at the NCRA and the uGMRT site for conducting the important observations related to this thesis. They were very friendly during my time there, especially Mr. Shriram Ramane, whom I remember vividly, as it was the 'first day in the trenches' for both of us.

I am forever grateful to my teachers for making me capable enough for this journey. I must mention the encouragement I received from my school teachers, especially from Abhijit *babu*, Hensh *babu*, Sougata *babu*, Subrata *babu*, Arnab *babu*, Angshuman *babu*, Bipul *da*, and Amitabha *babu*, whose curious minds and friendly behavior provided me an ideal beginning. I should also mention my respected mentor, Dr. Jagadish Chandra Roy (*dadu*), for inspiring me with his revered personality. Many thanks to Sampad *kaku*, Manas *mama*, and Buddhadeb *babu* for making learning exciting and fun.

I am highly indebted to the professors from my college days. Lectures, especially from Prof. Somnath Bharadwaj, Prof. Sayan Kar, and Prof. Sugata Pratik Khastgir, motivated me to pursue research as a career, and that worked as a catalyst ever since. Fruitful discussions with them in classrooms and beyond are of immense value, fostering deeper understanding and inspiring intellectual growth. I must also mention the encouragement I received from Dr. Nirupam Roy (Nirupam *da*), who was my M.Sc thesis supervisor along with Prof. Bharadwaj, which inspired me to choose Radio Astronomy as my field of research. I am also very thankful to Prof. Shiv K. Sethi from the Raman Research Institute, Bangalore, and present and past faculty members of the Physics department of Burdwan Raj College, including Dr. Mamata Bhattacharya, Dr. Sanat Kumar Manik, Dr. Abani Mohan Rudra, Dr. Surajit Mandal, Dr. Arup Dhara, Dr. Sachindranath Das as well as Prof. Debasis Bhattacharyya from the Kalna College, West Bengal, for their constant guidance and support.

Throughout, my mother, Supriti Rakshit Dey, was there for me with her love, patience, and constant encouragement. You have always believed in me, even when I doubted myself. Your strong presence, in the absence of my father, Joyanta Kumar Dey–whom I miss dearly and wish would have been present to witness–has and will always drive me to pursue my goals. To my sibling, Subhramoy Dey, and other family members, including my grandparents, uncles, aunts, brothers, sisters, nephew (Bittu), niece (Nandini), parents- and other relatives-in-law, I don't want to thank you for the values you put in my life. And I feel very fortunate to have you as my family. To Shinjini, Samya, Mithi, Kuttus, and Megh, the newest members of our family, though you are too young to understand right now, it gave me immense pleasure to see you guys over a video call after a long, tiring day. One day, when you are older, I hope you will understand just how much joy you brought me

during this time, even with the smallest gestures. To my better half, Priya, I cannot thank you enough for being there with me when I needed it the most from my college days. Your captivating approach toward life has helped me deal with difficult situations with ease. But, first of all, thank you very much for being my best friend.

I also wish to thank my friends from my school and college days, whom I feel very fortunate to have as friends. To Dipu, Subhadeep, Dibakar, Kiran, Parashar, and Barul, my school friends, thank you very much for staying in constant touch throughout this long period. To Habib, Sudip, Sugandha, Taniya, and Anupam, my college friends, thank you very much for keeping in touch and for your encouragement throughout this journey.

To my friends and seniors from IIT Kharagpur, I have learned a lot from you guys, both personally and academically. To Anirban, Upamannu, Saikat, Udvas, Agniva, Abantika, Poulomi, Kapil, Sawata, Suvadip, Joyjit, Kunal, and Satish, I always cherish the time we spent together during our stay at the IIT Kharagpur. Seniors, especially, Siddhartha *da*, Suman *da*, Debanjan *da*, Rajesh *da*, Samir *da*, Pritha *di*, and Abinash *da*, thank you very much for sharing your skills and experiences as being doctoral students, which I found very relevant throughout this pursuit.

To my friends and fellow researchers at IIST, thank you very much for your help and discussions and for making my time here enjoyable. To Sweta *di*, Sagnik, and Anindya, thank you very much for the endless *adda*s that worked as stress busters. To Akshay, Jogender *bhaiyya*, Govind, Pramod, Elango, Avinash, Gaurab, Debabrata, Manoj, Shiv, Narendra *bhaiyya*, Guru Krishna, Chavva Subbreddy, Vibin, Ajin, and Renjith, thank you very much for the time we had on campus. To my lab mates, Aneesha, Geethu, Namitha, Sreelekshmi, Arun, Amal, Hafiz, and Basavraj, thank you very much for making the workplace lively and vibrant. To my lab juniors, Ritwika, Sarwar, Ravi, Swapnil, Prachi, Bhagyashree, Kiran J., Manish, Deepak, Pratyush, Bhavana, Ajay, Divyansh, Shivanshi, Shashank, Saurabh, Amulya, Vishal, Samrat, Akaash, Dhiraj, Abraham, Sameer, Rohit, Satyapriya, Aniket, Amrit, and Suvajit it was wonderful sharing the lab with you guys. Thank you for the discussions we had together from time to time, which also enriched my perspectives. To Arnab, Raju, Pratyush, Dibya, Suvrojit, Akash, Kalishreyo, Rouhin, Sagnik, Bijay, Saptaswa, Manojit, Arunava, Tejas, Shubham, and Mukul, I adore you guys for the laughter and fun you brought at our every meet-up, and I wish you well in your future endeavors.

I know there are a few people I haven't thanked enough for the roles they played during this journey. To everyone who helped me along the way, your support made this work possible, and I am deeply grateful.

Jyotirmoy Dey

Abstract

Massive stars ($M \geq 8$ $M_{\odot}$) play a pivotal role in shaping the interstellar medium and influencing the evolution of galaxies through their intense radiation, stellar winds, and supernova explosions. These stars are the primary sources of ionizing radiation, producing large quantities of ultraviolet photons that ionize the surrounding gas and create H II regions. Studies of H II regions are critical for understanding how massive stars impact their environments and how the interstellar medium is chemically enriched and dynamically shaped over time.

Despite the importance of H II regions in tracing high-mass star formation, there remain some gaps in our understanding of their structure and evolution. A long-standing problem is the discrepancy between the ionizing photon rates inferred from radio and infrared observations. While infrared observations suggest higher ionizing photon rates, radio observations often detect significantly lower values, raising questions about the processes that govern the evolution of H II regions and how ionizing radiation interacts with the surrounding gas and dust. In particular, compact and ultracompact H II regions are known to exhibit this discrepancy, which has been a source of debate for several decades.

In this work, we explore the hypothesis that extended, arcminute-scale radio emission surrounding compact H II regions may account for this discrepancy. Using high-sensitivity radio observations from the *upgraded Giant Metrewave Radio Telescope* and complementary data from the GLOSTAR survey, we conducted a detailed multi-wavelength analysis of eight Galactic H II regions. Additionally, mid-infrared and far-infrared data from the Hi-GAL, MIPSGAL, and GLIMPSE surveys were utilized to assess the ionizing photon rates through spectral energy distribution fitting and other radiative transfer models.

Our findings reveal the presence of significant extended emission surrounding all eight target H II regions, which dramatically increases the radio-estimated ionizing photon rates, bringing them into closer alignment with the infrared estimates. The velocity field of the ionized gas, traced through radio recombination lines, is seen to be continuous across the compact and extended regions, suggesting a common source of origin for both regions. This extended emission, often undetected in earlier high-resolution studies due to sensitivity limitations, provides crucial missing flux that significantly reduces discrepancies in ionizing photon rates.

Our observations show the presence of hierarchical structure in compact and ultracompact H II regions, which may help resolve the "age problem" of ultracompact H II regions. In the context of hierarchical structure, the extended emission is likely to arise from the leakage of ionizing photons into regions of lower density, as opposed to the classical picture of expansion of a bubble of uniform density. Thus, ultracompact H II regions with associated extended emission may not be as young as that inferred from the size of the compact emission alone.

We find the presence of multiple ionizing sources in all eight sources of our sample. We find good agreement between the rate of Lyman continuum photons as inferred from the radio emission and the overall rate from the different ionizing stars. The luminosity of the nebular emission from the H II region is also found to be in good agreement with the total luminosity of the ionizing stars. These confirm the clustered nature of massive star formation and provide further support for a common origin for the compact and extended emission components.

In addition, we have found signatures of a cloud-cloud collision in a multi-wavelength study of an ultracompact H II region, G18.148−0.283. The velocity distribution map of the ionized gas reveals the presence of a velocity gradient of approximately 10 km s^{-1} across the radio continuum peaks. The ^{12}CO (J=3−2) molecular line data also shows the presence of two velocity components (corresponding to two molecular clouds) that overlap with the ionized gas velocities. Besides, the spectrum and position-velocity diagram generated from the CO emission reveal intermediate-velocity molecular gas bridging those velocity components, a very important signature of a cloud-cloud collision. These bridging features are also visible in the position-velocity diagram created from the radio recombination line emission from the ionized gas, which could be a first-of-its-kind discovery. Furthermore, the mid-infrared absorption and far-infrared emission maps establish the presence of a filamentary infrared dark cloud, which may have formed due to a collision.

In sum, the broader implications of this research highlight the importance of accounting for large-scale diffuse emission in radio observations of H II regions. Our findings emphasize the need for high-sensitivity surveys, such as the forthcoming *Square Kilometre Array*, which will further enhance our understanding of how ionizing feedback from young massive stars influences the interstellar medium and drives galactic evolution. By shedding light on the dynamics of ionized regions and their surrounding environments, this work provides a critical step forward in unraveling the complex processes that govern massive star formation and feedback in the Galaxy.

Contents

[1]This chapter is based on the published paper: Dey et al. (2022) [Jyotirmoy Dey, Jagadheep D. Pandian, and Dharam Vir Lal, “Gas Dynamics in the star-forming Region G18.148–0.283: Is It a Manifestation of Two Colliding Molecular Clouds?", 2022, The Astrophysical Journal, 925, 60]. The paper is reproduced here with minor changes.

[2]This chapter is based on the published paper: Dey et al. (2024) [Jyotirmoy Dey, Jagadheep D. Pandian, and 10 co-authors, “A multi-wavelength study of Galactic H II regions with extended emission", 2024, Astronomy & Astrophysics, 689, A254]. The paper is reproduced here with minor changes.

List of Figures

List of Tables

Abbreviations

2MASS	2 Micron All Sky Survey
AIPS	Astronomical Image Processing System
ATLASGAL	The APEX telescope large area survey of the galaxy at 870 μm
CASA	Common Astronomy Software Applications
CBCD	Corrected Basic Calibrated Data
CCC	Cloud-Cloud Collision
CCD	Color-Color Diagram
CHR	Compact H II Region
CMD	Color-Magnitude Diagram
COHRS	CO High-Resolution Survey
CORNISH	Co-Ordinated Radio 'N' Infrared Survey for High-mass star formation
EGO	Extended Green Object
EM	Emission Measure
FIR	Far Infrared
FWHM	Full Width at Half Maximum
GHz	Giga Hertz
GLIMPSE	Galactic Legacy Infrared Mid-Plane Survey Extraordinaire
GLOSTAR	A Global View on Star Formation survey
GMC	Giant Molecular Cloud
HARP	Heterodyne Array Receiver Programme
HCHR	Hypercompact H II Region
Hi-GAL	The Herschel infrared Galactic Plane Survey
HIPE	Herschel Interactive Processing Environmen
HMC	Hot Molecular Cores
HMPO	High-Mass Protostellar Objects
IMF	Initial Mass Function
IRAC	Infrared Array Camera

IRDC	Infrared Dark Cloud
ISM	Interstellar Medium
LSR	Local standard of rest
MAGPIS	Multi-Array Galactic Plane Imaging Survey
MHz	Mega Hertz
MIPS	Multiband Imaging Photometer for Spitzer
MIPSGAL	MIPS Galactic Plane Survey
MIR	Mid Infrared
NIR	Near Infrared
NRAO	National Radio Astronomy Observatory
PACS	Photometric Imaging Receiver
PAH	Polycyclic Aromatic Hydrocarbon
PBCD	Post-Basic Calibrated Data
PDR	Photo-Dissociation Region
PRF	Point Response Function
PV	Position-velocity
RFI	Radio Frequency Interference
RMS	Red MSX Survey
RRL	Radio Recombination Line
SED	Spectral Energy Distribution
SNR	Supernova Remnant
SPIRE	Spectral and Photometric Imaging Receiver
THOR	The HI/OH/Recombination line survey of the inner Milky Way
UCHR	Ultracompact H II Region
uGMRT	upgraded Giant Metrewave Radio Telescope
UKIDSS	The UKIRT Infrared Deep Sky Survey
UV	Ultra Violet
VLA	Karl G. Jansky Very Large Array
YSO	Young Stellar Object

Chapter 1

Introduction

Stars, as the luminous units of the Universe, play a pivotal role in galaxy evolution and enrich the cosmos with heavy elements. Understanding the intricate process of star formation requires various astronomical observations. While the mechanisms of low-mass star formation are well-known, many aspects of the mechanisms that form high-mass stars ($M \geq 8$ $M_{\odot}$) still remain elusive. Massive stars significantly influence the evolution of galaxies as principal sources of heavy elements, contributing to the chemical enrichment of the Universe. Their outflows, stellar winds, and supernova explosions also significantly affect the interstellar medium (ISM). To comprehend the physical, chemical, and morphological structure of galaxies, it is essential to study the processes underlying the formation of high-mass stars and their subsequent influence on the local environment.

The early stages of massive star formation are particularly challenging to observe, as these stars are deeply embedded within dense molecular clouds. The obscuration of visible and near-infrared (NIR) light necessitates utilizing longer wavelengths, such as millimeter/submillimeter and radio, for penetrating the surrounding dust and gas. Additionally, the high-mass stars forming in clusters make it difficult to disentangle individual sources in crowded regions, further complicating direct observations. Moreover, massive stars are relatively rare compared to their low-mass counterparts, following a power-law with a slope of approximately -2.35 in the stellar initial mass function (IMF; Kroupa 2001). Consequently, they are scarcer, making their study more challenging. Furthermore, their short lifespan leads to fleeting evolutionary stages, especially during the early phases of formation, further contributing to the scarcity of high-mass star-forming regions in their initial stages of evolution.

Many intensive investigations have focused on the early phases of high-mass star formation for numerous years. The emergence of massive stars is accompanied by significant emission of ultraviolet (UV) photons. The emission of Lyman-continuum photons ($\lambda <$

911 Å) leads to the ionization of the ISM, creating H II regions, thereby exposing the locations of ongoing high-mass star formation, which can be observed through free-free emission at radio wavelengths. This evolutionary sequence begins with deeply embedded, hypercompact H II regions, which gradually expand and evolve into ultracompact H II regions (UCHRs), followed by compact H II regions (CHRs). In addition to their radio brightness, the H II regions exhibit high luminosity in the mid and far-infrared (MIR & FIR) wavelengths. This brightness in the MIR and FIR results from the absorption of ultraviolet and optical photons by dust, which then re-emits their energy in these wavelengths. Since radio, millimeter/submillimeter, FIR, and MIR wavelengths are less affected by extinction, researchers can conduct studies in these wavelength ranges to gain deeper insights into the processes linked to the formation of massive stars and the dust present within star-forming clouds.

A critical problem in the field of massive star formation is to understand their formation mechanism. Several formation theories have emerged to explain how these stars come into existence, with core accretion (McKee & Tan, 2002, 2003) and competitive accretion (Bonnell et al., 2001; Bonnell & Bate, 2006) being the most prominent. Apart from these two significant models, massive stars can also form while being triggered by some other external factors, like cloud-cloud collisions (Torii et al., 2015) and external shocks due to supernova explosions (Nagakura et al., 2009). In a cloud-cloud collision, two molecular clouds collide, and the resulting shock waves compress the gas, leading to increased density and temperature in certain regions. This compression can initiate the gravitational collapse necessary for star formation. Whereas for the second triggering method, when a star explodes in a supernova, it sends shock waves in all directions, triggering the collapse of nearby clouds and leading to the formation of new stars.

The late stages of massive star formation, specifically UCHRs and CHRs, are associated with some long-standing problems. One such problem is the observed discrepancy in the rates of ionizing or Lyman-continuum photons inferred from the radio continuum and infrared emissions, with the rate estimated from radio being up to 90% lower than the same inferred from the infrared emission (Wood & Churchwell, 1989). A later study by Kurtz et al. (1994) also found this inconsistency, attributing it to the absorption of Lyman-continuum photons by dust present within the H II region. However, further studies by Kurtz et al. (1999), Kim & Koo (2001), Ellingsen et al. (2005), and de la Fuente et al. (2020) suggested that diffuse radio continuum emission linked to the ultracompact H II regions could also be related to the inconsistency in the rates of ionizing photons. This extended emission mostly remains undetected because of the interferometric observations'

limited sensitivity to scales larger than that characterized by the shortest baseline. Considering this diffuse emission will result in higher radio continuum flux and ionizing photon rates nearer to those estimated from infrared data, reducing the need for high dust absorption, as previously advocated. A similar scenario can also happen for the CHRs, where the absorption by the dust may be overestimated because of the non-detection of diffuse emission surrounding the compact core (Habing & Israel, 1979).

In this thesis, we attempt to make a comprehensive assessment of the extended emission's role in the evolution of UCHRs and CHRs and the resolution of long-standing problems associated with the same.

Outline of the thesis

The thesis is structured as follows:

- Chapter 2 contains a brief overview of star formation with special attention on the formation of massive stars.
- A discussion on H II regions, including their properties, classifications, and a couple of associated long-standing problems, is presented in Chapter 3.
- Chapter 4 includes observation and data analysis techniques, including our observations using uGMRT.
- In Chapter 5, we study the dynamics of ionized gas in the H II region G18.148−0.283 to understand its formation mechanism.
- Chapter 6 presents a study of Galactic H II regions with diffuse emission using multi-wavelength data.
- In Chapter 7, we summarize our results and provide prospects for future work.

Chapter 2

An overview of star formation

2.1 Introduction

The formation of stars due to the gravitational collapse of molecular clouds involves a multifaceted field of study that combines extensive theoretical work with advanced computational efforts and multi-wavelength observations. Despite substantial progress in comprehending the underlying physical processes, numerous questions remain unresolved or subject to debate within this active research area. This section provides a concise overview of this intricate subject.

The ISM serves as the cradle for star formation, housing the essential raw materials required for this cosmic process. Containing mostly hydrogen and helium, the ISM constitutes approximately 10–15% of the total mass of the Galaxy (Ferrière, 2001). It manifests in various phases, each characterized by distinct properties, as outlined in Table 2.1. The hot inter-cloud medium, with temperatures around 10^6 K and densities near 0.003 cm^{-3}, is generated by supernova-driven shocks and occupies a large volume of the Galaxy. The warm neutral medium, at temperatures of $\sim$ 8000 K and densities of $\sim$ 0.3–0.5 cm^{-3}, is composed primarily of diffuse neutral hydrogen (H I). The warm ionized medium, at $\sim$ 8000 K and $\sim$ 0.1 cm^{-3}, is partially ionized, maintained by the leakage of ionizing photons from massive stars and is often associated with the extended emission around H II regions. These H II regions, with temperatures of 7000–10000 K and densities of 100–10^5 cm^{-3}, are ionized regions surrounding young, massive stars, where UV radiation ionizes the surrounding hydrogen. The cold neutral medium, with temperatures of 50–100 K and densities of $\sim$ 20–50 cm^{-3}, is the cooler phase of neutral hydrogen, commonly found in more confined structures such as filaments. The denser regions are molecular clouds, with temperatures of 10–20 K and densities ranging from 100–1000 cm^{-3}, where gas exists primarily in molecular form (H_2). Also, being predominantly situated in the spiral

arms of our Galaxy, these interstellar clouds can be broadly categorized as dark clouds, diffuse clouds, and translucent clouds (Ferrière, 2001), exhibiting variations in temperature, extinction, and composition. These components together form a dynamic system that regulates star formation and material recycling in galaxies (McKee & Ostriker, 1977; Ferrière, 2001).

Star formation predominantly occurs within the molecular component of the Galaxy, primarily in giant molecular clouds (GMCs; see Fig. 2.1) within the cold neutral medium. GMCs, the birthplace of countless stars, stand out as the most massive entities in our Galaxy. The mass of GMCs ranges from about 10^4 to 10^6 $M_\odot$, making them some of the most massive entities in galaxies. The largest GMCs can span up to hundreds of parsecs and are crucial for forming clusters of stars, including massive stellar populations (Magnani et al., 1985; Brand & Wouterloot, 1995; Heyer et al., 2001; Oka et al., 2001; Beuther et al., 2007b). These enormous structures are predominantly composed of molecular hydrogen (H_2), comprising roughly 70% of their total mass (Fukui & Kawamura, 2010) and constituting $\gtrsim 1000$ cm^{-3} by density (Williams et al., 2000), with helium (He) comprising around 26% of their mass and traces of atomic hydrogen (H I) gas (Fukui & Kawamura, 2010).

Figure 2.1: Images showing the 'pillars of creation,' a giant molecular cloud. The left panel shows NASA's Hubble Space Telescope view of the 'pillars of creation' in visible light, while a new, near-infrared light view from NASA's James Webb Space Telescope is shown on the right panel. The near-infrared light helps us peer through more of the dust in this giant molecular cloud. Thus, the thick, dusty brown pillars (left panel) are no longer as opaque, and many more red stars that are still forming come into our view (right panel). Image credit: NASA, ESA, CSA, STScI.

Various mechanisms have been proposed to account for the formation of molecular

Table 2.1: Physical properties of various phases of the ISM. The values are taken from Tielens (2005)

Phase	Fractional volume (%)	Temperature (K)	Scale height (pc)	Number density (cm^{-3})
Hot inter-cloud	50	10^6	3000	0.003
Warm Neutral Medium	30	8000	200	0.5
Warm Ionized Medium	25	8000	900	0.1
Cold Neutral Medium	1	80	94	50
Molecular clouds	0.05	10	75	$>$200
H II region	–	10^4	70	10^5

clouds, including converging flows driven by stellar feedback or turbulence, agglomeration of smaller cloud fragments, gravitational and magneto-gravitational instability, and instability linked to differential buoyancy (Dobbs et al., 2014). Although a combination of these mechanisms may operate in different galactic environments, the prevailing consensus is that GMCs take shape within the Milky Way's disk as molecular gas gets trapped in the spiral wave pattern of the galactic gravitational potential energy (Elmegreen, 1994), with gravitational collapse occurring more swiftly within the spiral arms due to the reduced impact of tidal shear forces (Luna et al., 2006). This is substantiated by observational evidence, as GMCs are predominantly found within the spiral arms of the Milky Way (Stark & Lee, 2006).

Molecular line observations have unveiled the clumpy and inhomogeneous nature of GMCs (Myers & Benson, 1983; Bronfman et al., 1989), leading to a classification scheme of the hierarchical substructures present within clouds. This categorization broadly includes clumps ($n(H_2) \sim 10^3$ cm^{-3}; Larson 2003), and cores ($n(H_2) \sim 10^5$ cm^{-3}; Churchwell 2002), which further fragment into smaller structures at higher-resolution (Williams et al., 2000). These hierarchical substructures form through gravitational collapse and fragmentation of regions with elevated densities, marking the initial phases of star formation.

In these preliminary phases, gravity plays a pivotal role, with various opposing forces coming into play at different scales. As opposed to the largest scales of diffuse interstellar matter, where galactic tidal forces become significant, and condensation commences when gravity prevails over these forces, turbulence and magnetic fields are dominant counteracting forces to gravity, and their dissipation triggers collapse at the scale of GMCs. Whereas, at the scale of individual cores, thermal pressure and magnetic fields act as the opposing force to gravity, defining the minimum mass threshold for core collapse and the initiation of star formation. As cores undergo gravitational collapse, angular momentum-induced cen-

trifugal forces may temporarily halt contraction, potentially forming binary or multiple-star systems. When the central region of a core reaches stellar densities, thermal pressure prevents further collapse, giving rise to a 'stellar embryo' or 'protostar' that grows through mass accretion from its envelope. This phase is accompanied by the emergence of bipolar jets, signaling ongoing accretion (Williams et al., 2000).

2.2 Low-mass star formation

Low-mass stars vastly outnumber their high-mass counterparts (Salpeter, 1955; Kroupa, 2001), and the proximity of numerous low-mass star-forming regions has made their study highly favorable. A solid comprehension of the mechanisms behind low-mass star formation is a foundational step before delving into the realm of high-mass stars. The classical model for low-mass star formation, as elucidated in pioneering works by Shu (1977), Shu et al. (1987), and later by Lada & Shu (1990) and Kennicutt & Evans (2012), outlines various stages in this process (see Fig. 2.2 for a brief overview).

Initially, the self-gravity of GMCs contends with turbulent and magnetic pressures, resisting collapse. Over time, ambipolar diffusion causes the separation of neutral atoms from ions due to the fact that ionized particles will not have the same mean velocity as the neutral species (Shu, 1992). This leads to a dissipation of magnetic support, as the charged particles are directly affected by the electromagnetic forces, whereas the neutrals only experience them through collisions with the ionized species. As ambipolar diffusion continues, magnetic pressure decreases, resulting in a dominance of gravity. This gradual process allows neutral gas to form a dense, slowly rotating protostellar core, a stage that persists longer than the free-fall time scale

$$t_{ff} = \left(\frac{3\,\pi}{32\,G\,\rho} \right)^{\frac{1}{2}}, \tag{2.1}$$

where ρ is the density of the gas and G is the gravitational constant. However, turbulence can influence the collapse time scale (Fatuzzo & Adams, 2002; Zweibel, 2002; McKee & Ostriker, 2007).

The conditions for equilibrium are dictated by the virial theorem, which states that for a gravitationally bound system in equilibrium, the total kinetic energy is half the gravitational potential energy. Perturbations to this balance trigger collapse, which can be induced by various factors such as shockwaves from nearby supernova explosions, intense UV radiation from massive stars, or GMC collisions. The Jeans' mass, expressing the minimum

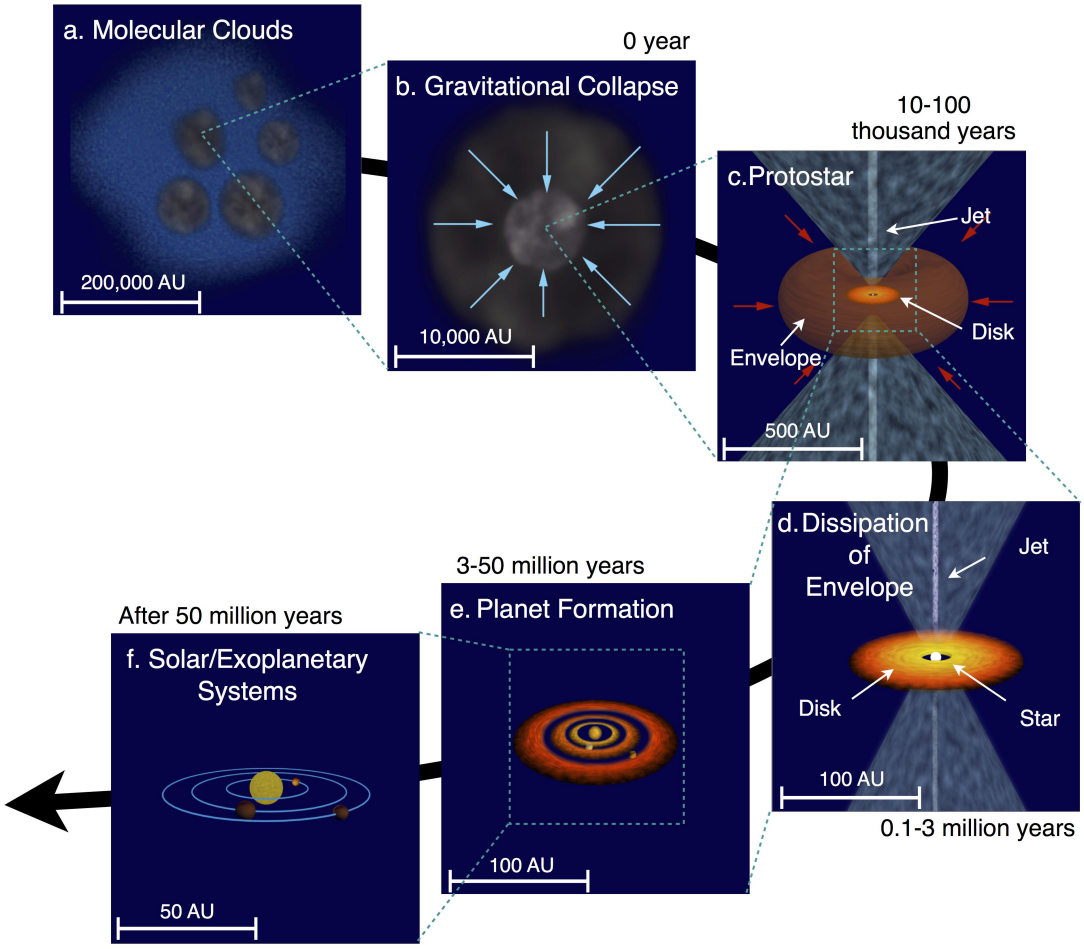

Figure 2.2: A schematic diagram of low-mass star formation. Image credit: ASIAA.

mass required for gravitational collapse, plays a pivotal role in this process, and it is dependent on cloud density and temperature. Isothermal clouds remain stable if their mass remains below the Jeans' mass. However, once the cloud surpasses this critical mass, it undergoes runaway contraction, continuing until some opposing force intervenes. This critical mass or the Jeans mass' (Shu et al., 1987) is given by

$$M_J = \left(\frac{5\,k_b\,T}{\mu\,m_H\,G}\right)^{\frac{3}{2}} \left(\frac{3}{4\,\pi\,\rho}\right)^{\frac{1}{2}}, \tag{2.2}$$

where ρ and T are the density and temperature of the cloud, m_H is the mass of the hydrogen atom, μ is the mean molecular weight, and G is the gravitational constant.

During the initial phase, the cloud is optically thin, and the collapse remains isothermal, efficiently radiating away gravitational energy without heating the cloud. The temperature remains constant while density increases due to collapse, leading to the satisfaction of the

Jeans' criteria in substructures within the cloud that results in fragmentation and formation of clumps and cores. Moreover, internal turbulent motions within GMCs, often supersonic on scales other than the smallest, also contribute to fragmentation and clumpy structures. The gravitational fragmentation cascades until the cloud becomes opaque to its radiation, causing the collapse to transition from isothermal to adiabatic. In this phase, the Jeans' mass increases with density, setting a limit on the mass of the smallest cores. Alternatively, observed turbulent motions within molecular clouds become subsonic on the minor scales, suggesting a lower limit to the sizes of compressed structures formed by turbulence.

As the density steadily increases toward the core's center, a transformation occurs as the core undergoes an inside-out collapse. During this process, a phase of accretion commences, in which surrounding envelope material progressively descends upon the protostar, taking shape at the core's very center. In this accretion phase, centrifugal forces increase due to the conservation of angular momentum that is being dumped by the infalling material, forming a disk structure surrounding the central protostar (Zinnecker & Yorke, 2007). The accretion rate is believed to be more rapid in the initial stages of protostar formation (Larson, 2003). The matter being accreted into the circumstellar disk also generates a highly collimated bipolar jet, with magnetic forces in the accretion disk generating the initial outflow (McKee & Ostriker, 2007). Outflows are a common feature of low-mass star formation (Arce & Sargent, 2006), and also help remove excess angular momentum from the collapsing protostellar core. Without this mechanism, the conservation of angular momentum would cause the core to spin too rapidly, potentially inhibiting further collapse and affecting the star formation process. In the case of low-mass stars, accretion ceases when the star enters the hydrogen-burning phase, as the strong stellar winds inhibit further matter accretion.

2.3 High-mass star formation

Moving from the well-understood low-mass star formation processes, we encounter a significant divergence when it comes to the formation of high-mass stars. One of the primary challenges in comprehending the birth of massive stars is the unresolved issue of how high-mass stars overcome the 'radiation pressure problem,' in which intense radiation from the protostars should halt accretion. Furthermore, high-mass star formation is a rarer and more fleeting process compared to low-mass star formation, which occurs more commonly in relative isolation and has a longer lifespan.

However, the crucial difference lies in the time frames involved. The gravitational

collapse is governed by the free-fall time (eq. 2.1), which is also linked to how long the collapsed core continues to accrete material (Shu et al., 1987). This duration is known as the accretion timescale (t_{acc}), which is given by

$$t_{acc} = \frac{M}{\dot{M}}, \tag{2.3}$$

where M and $\dot{M}$ are the mass of the core and mass accretion rate, respectively. As the cloud contracts, the gravitational potential energy is gradually converted into thermal energy, marking the Kelvin-Helmholtz (K-H) timescale

$$t_{KH} = \frac{G\,M^2}{R\,L}, \tag{2.4}$$

where R, L, and M are stellar radius, luminosity, and mass, respectively. The K-H timescale represents the time required for the star to radiate away its current gravitational binding energy at its present luminosity. It's the timescale in which the star would contract if its nuclear energy sources were turned off.

For low-mass stars, the K-H timescale surpasses the accretion timescale ($t_{KH} > t_{acc}$), meaning that accretion concludes before hydrogen burning initiates. However, for high-mass stars, the K-H timescale is considerably shorter than the accretion timescale ($t_{KH} < t_{acc}$). This occurs because t_{KH} depends on luminosity, with $L \propto M^{\alpha}$ (where $\alpha > 2$). A shorter Kelvin-Helmholtz timescale implies that fusion begins before the star stops accreting. The resulting high luminosity generates a powerful outward radiation pressure, which hinders the continued accretion of matter (Beuther et al., 2007b).

We have demonstrated this in Fig. 2.3, where the K-H timescale and accretion timescale are depicted for a range of stellar masses. From this figure, depending on the accretion rate, it becomes evident that for stars with masses greater than 10 $M_{\odot}$, $t_{KH} < t_{acc}$. This indicates the high-mass regime, where stars initiate nuclear fusion while still accreting gas (Palla & Stahler, 1993; Keto & Wood, 2006).

The radiation pressure from the photons emitted by stars undergoing nuclear fusion could potentially impede further accretion, dissipate the infalling envelope, and, consequently, impose a limit on the ultimate mass of the star (around 30 $M_{\odot}$ that can form through accretion; Palla & Stahler 1993). However, observations have identified stars with masses exceeding 150 $M_{\odot}$ (Figer, 2005; Crowther et al., 2010), and the mechanism behind their formation remains a topic of intense debate.

Several theoretical models have been proposed to illuminate the formation of massive stars. The three primary theories include the monolithic collapse of a massive quasi-

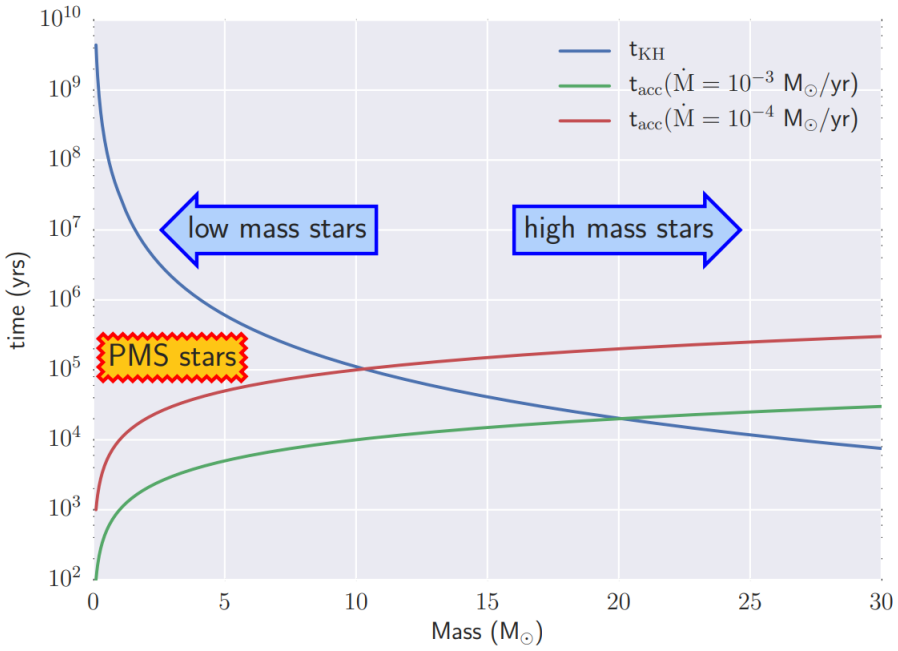

Figure 2.3: Image showing the Kelvin-Helmholtz (K-H) timescale and accretion timescale ($t_{acc} = M/\dot{M}$) for stars with masses between 0 – 30 $M_\odot$. For lower-mass stars, the K-H timescale is longer than the accretion timescale, while, depending on the accretion rate, for stars with masses ≥ 10 $M_\odot$, this relationship reverses. Image credit: Schilke (2015).

hydrostatic core (Myers & Fuller, 1992; McKee & Tan, 2003), competitive accretion (Bonnell et al., 2001; Bonnell & Bate, 2006), and stellar collisions (Bonnell et al., 1998).

2.3.1 Monolithic collapse and core accretion

In the context of high-mass star formation, we can consider monolithic collapse as an 'amplified' version of the low-mass star formation. It commences with the presence of self-gravitating cores that are densely concentrated. These cores, from which high-mass stars are born, are supported by internal turbulence over thermal motion (Myers & Fuller, 1992). This concept was further developed in the 'core accretion' model introduced by McKee & Tan (2003). In this model, the initial core is approximated as a single polytropic sphere, as it is in a state of internal virial equilibrium. The stability of these prestellar cores is assessed through their virial parameter, denoted as α_{vir}, defined as

$$\alpha_{vir} = \frac{5\,\sigma_{1D}^2\,R_c}{G\,M_c}, \tag{2.5}$$

where σ_{1D}^2 represents the core's one-dimensional velocity dispersion, M_c and R_c are the core's mass and radius, respectively (Bertoldi & McKee, 1992). Cores with $\alpha_{vir} > 2$ are considered stable against gravitational collapse, while those with $\alpha_{vir} < 2$ are prone to collapse. The 'core accretion' model postulates that the cores with surface densities $\sim$ 1 gm cm^{-2} give rise to high-mass stars and exhibit highly supersonic turbulence, implying $\alpha_{vir} \sim 1$ (Tan et al., 2014). Consequently, the formation timescale becomes several times longer than the core's free-fall timescale ($t_{ff} \sim 10^5$ years), and the substantial turbulence leads to clumping, resulting in high accretion rates ($\dot{M}_{acc} \sim 10^{-4}$ to 10^{-3} M$_\odot$ yr^{-1}). These high accretion rates can effectively counteract the radiation pressure linked to the star's significant luminosity (McKee & Tan, 2003; Rosen et al., 2019). Observational support for this concept is found in the existence of massive cores residing in high-pressure environments, marked by non-thermal turbulent motions outweighing thermal motions (Tan et al., 2013; Zhang & Tan, 2015; Liu et al., 2018). However, there are other observational studies that contradict the dominance of turbulent motion within cores (e.g., Peters et al. 2010; Pandian et al. 2024).

Additionally, simulations conducted by Krumholz et al. (2009) suggest that radiation does not hinder accretion; instead, accretion continues through a disk onto the massive protostar. Moreover, the formation process involves the creation of cavities through jets and outflows, which serve as pathways for radiation to escape without obstructing the accretion process. The observation of highly focused jets and outflows (Marti et al., 1993; Beuther et al., 2005) and rotating structures (Beuther et al., 2017; Motogi et al., 2019) lends empirical support to this model. While the monolithic collapse model effectively explains the formation of isolated massive stars by assuming the existence of stable, massive starless cores, possibly on the order of 10^2 Jeans masses (Tan et al., 2014), with more massive stars emerging from more substantial cores, conclusive detections of starless massive cores remain elusive (Motte et al., 2018; Massi et al., 2019).

2.3.2 Competitive accretion

This model presents an alternative perspective on how high-mass stars form, emphasizing the fragmentation of the cloud leading to the emergence of multiple low-mass protostars. This theory is grounded in the observation that massive stars are primarily found in clusters (Bonnell et al., 1998; Stahler et al., 2000). As its name suggests, this model involves a gravitational competition for gas within densely populated stellar clusters (Bonnell et al., 2001). In the context of the typical formation of a single star, gas accretion mainly occurs from

the parent clump. However, the dynamics change when cluster formation is considered.

According to this model, the cluster originates from the existence of a substantial reservoir of gas, and within this cluster, protostars essentially 'compete' for the available gas to support their growth. Key factors in this hypothesis include the size of the accretion region, the mass of the developing protostellar embryo, and the spatial distribution of neighboring protostars. The growth of these protostellar fragments occurs in a highly uneven manner, depending on their specific positions within the cluster (Bonnell et al., 1998).

Additionally, the region where stars are forming has its most significant gravitational potential energy at the center, leading to an increased rate of gas accretion toward this central area. Consequently, stars located near the cluster's center tend to become more massive primarily due to the increased accretion rates.

The 'competitive accretion' model relies on the presence of a distributed gas reservoir initially characterized by low-velocity dispersion, which is typical in a turbulent medium. This model provides insights into how the overall stellar mass of a cluster is connected to the most massive star within it. Moreover, it helps explain the distribution of stellar masses, the occurrence of mass segregation in young stellar clusters, and the high frequency of binary systems, along with the characteristics of massive stars. However, one of the primary challenges faced by this process is the influence of radiation pressure, which imposes significant limitations on accretion, particularly for stars with masses exceeding 10 $M_{\odot}$ (Edgar & Clarke, 2004).

2.3.3 Stellar merger

In this hypothesis, the initial formation of cores and protostars follows the low-mass theory but within a densely populated and clustered environment, as originally suggested by Bonnell et al. (1998) and later by Bonnell (2002). The main purpose of this theory was to address the challenge of gas accumulation in the face of strong radiation pressure.

In this model, the formation of high-mass stars through mergers is considered more viable in the most massive star clusters characterized by extreme density. If the cluster exhibits a high stellar density, around 10^6 to 10^8 pc^{-3} (Tan, 2006), it can lead to the merger of multiple protostars, resulting in the creation of massive stars. However, such densely populated clusters are not commonly observed. N-body simulations conducted by Baumgardt & Klessen (2011) lend very little support to the merger as one of the primary mechanisms for massive star formation. Nonetheless, Takahira et al. (2014) showed that stellar mergers still play a role in forming certain observed massive cores.

Hence, it is plausible that some stellar mergers may take place near the centers of certain star clusters, but the idea that stellar mergers account for a significant portion of high-mass stars encounters several substantial challenges, including the lack of explanation of observed disks and collimated outflows by this model and the proposed ultradense state, which would be highly luminous due to the presence of massive stars, has never been observed Beuther et al. (2007a).

2.3.4 Cloud-cloud collision

Recent years have witnessed a surge in observational evidence (Torii et al., 2015, 2017; Fukui et al., 2016) bolstering the role of cloud-cloud collisions as a mechanism triggering high-mass star formation. These studies illuminate the formation scenario of O-type stars, strengthening the pivotal role of supersonic compression resulting from cloud-cloud collisions.

Cloud-cloud collisions arise when two molecular clouds interact in the ISM. The collision of two clouds, which are primarily comprised of cold, dense gas and dust, induces shock waves, which compress the cloud material, setting off localized collapses within the clouds. Such compression serves as a trigger for the formation of stars, including massive stars. It is worth noting that the intricate dynamics of cloud-cloud collisions are influenced by an array of factors, including relative velocities, masses, densities, magnetic fields, and turbulence within the clouds.

The foundation for our understanding of cloud-cloud collisions was laid by Habe & Ohta (1992), whose pioneering numerical calculations provided critical insights into the dynamics of these collisions. Subsequent studies, such as those conducted by Anathpindika (2010), Inoue & Fukui (2013), and Takahira et al. (2014), have further advanced our knowledge in this realm, offering valuable numerical perspectives on the intricate processes at play during cloud-cloud collisions. Cloud-cloud collisions offer a compelling mechanism for the formation of high-mass stars by promoting the compression of the material, which collapses further under the influence of self-gravity, ultimately overcoming the challenges posed by radiation pressure.

2.4 Evolution of high-mass stars

The observed early developmental phases for low-mass stars such as our Sun can be categorized into four primary classes: Class 0, I, II, and III. This classification is based on

the characteristics of their spectral energy distributions (SEDs) across near-infrared to submillimeter wavelengths, as outlined by André (2015). Class 0 sources, with temperatures below 70 K, represent low-mass protostars. Their SEDs peak beyond 100 μm in the submillimeter range, exhibiting minimal emission, often going undetected, in the NIR and MIR. These sources are surrounded by substantial envelopes and discs, and their ages typically amount to a few times 10^4 years.

Moving to Class I, these sources are in the late accretion phase, gradually accumulating the remaining stellar mass. Similar to Class 0, Class I objects are shrouded by a residual envelope and a sizable circumstellar disk. Their peak emissions occur in the MIR and FIR wavelengths, lasting for a few times 10^5 years. Class II stars lack an envelope but possess an optically thick accretion disc, leading to observable excess infrared emission. Many classical T Tauri stars fall into this category. Class III stars are post-accretion but still in the pre-main-sequence stage (see Fig. 2.4 for details).

In contrast to low-mass stars, the formation of high-mass stars does not follow a well-defined observational evolutionary sequence. This is primarily due to the complex nature of massive stars deeply embedded in their parent clouds. Despite this lack of a clear sequence, certain objects (see Fig. 2.5 for a brief overview) provide insights into the evolutionary stages of high-mass star formation, which will be briefly discussed in the following subsections.

2.4.1 Infrared dark clouds

Infrared dark clouds (IRDCs) represent the cold and dense regions within giant molecular clouds. They harbor collections of cold (T $<$ 20 K), dense (n $>$ 10^5 cm^{-3}), and massive (M $\approx$ 100 M$_\odot$) clumps, displaying either compact or filamentary structures (Lada & Lada, 2003; Pillai et al., 2006). Initially identified by the Infrared Space Observatory (Kessler et al., 1996) and the Midcourse Space Experiment (Price et al., 2001), these clouds manifest as dark extinction features against the intense MIR galactic background emission (Hennebelle et al., 2001). Found throughout the Galaxy (Rathborne et al., 2006), IRDCs are considered to be the precursors of massive protostellar and cluster formation. The IRDCs contain jet-like outflows (Wang et al., 2011) and extended green objects (EGOs; Yu & Wang 2013), both serving as indicators of massive YSOs. The internal structure of IRDCs is most effectively examined at FIR and millimeter/submillimeter wavelengths, as their thermal emission peaks in this range due to their low temperatures. Moreover, this facilitates an accurate tracer of mass and column density since dust emission is optically

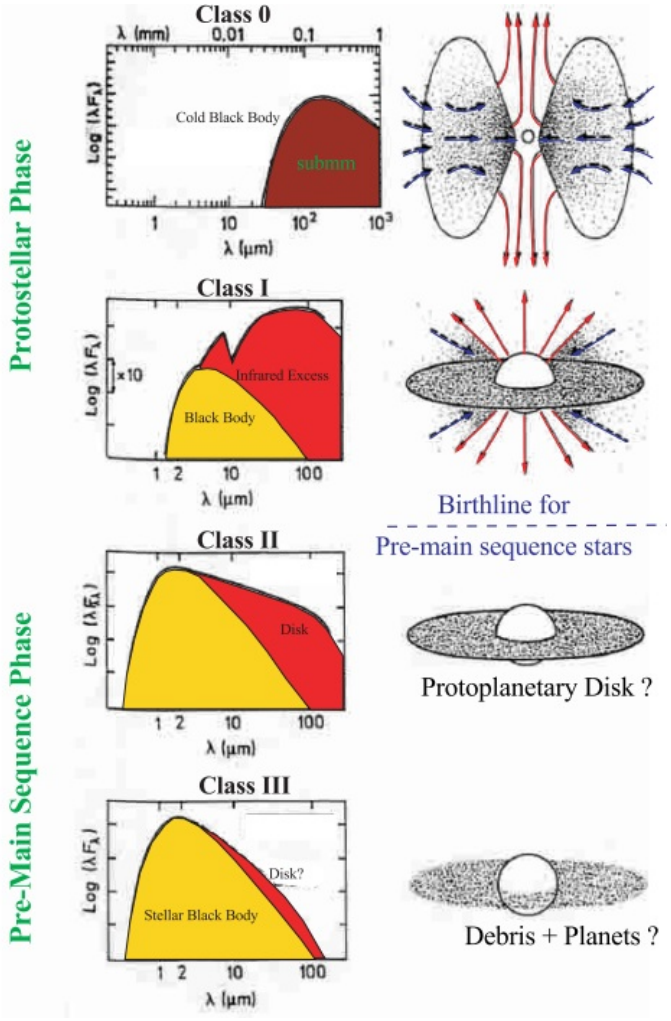

Figure 2.4: Image showing the empirical evolutionary sequence during the formation of a low-mass star from Class 0 to Class III young stellar object (YSO), based on the shape of the SED. Image credit: André (2002).

thin at these wavelengths.

2.4.2 High-mass protostellar objects and Hot molecular cores

High-mass protostellar objects (HMPOs) are distinguished in observations by their elevated luminosities ($L > 10^3$ $L_\odot$; Ao et al. 2018), prominent dust emission, and a notable absence or very weak detectable free-free emission from the ionized gas at centimeter wavelengths (Sridharan et al., 2002). This characterization positions them as one of the initial phases in the formation of high-mass stars. The HMPOs exhibit masses and sizes spanning from a few hundred to a few thousand solar masses and 0.25–0.5 parsecs, respectively, resembling

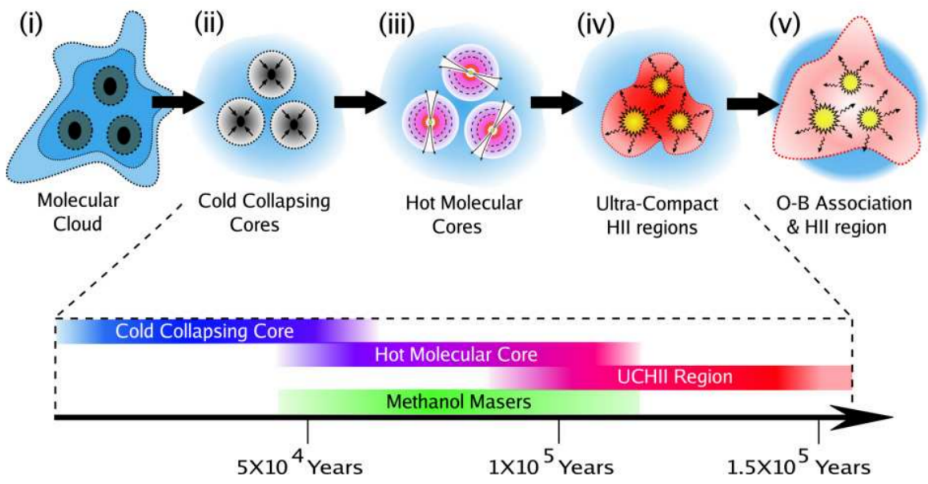

Figure 2.5: Image showing a schematic of evolutionary stages of high-mass star formation. This image is adapted from Dr. Cormac Purcell's thesis.

the characteristics of IRDCs. However, HMPOs distinguish themselves by higher temperatures (approximately 22 K) and greater densities ($n > 10^6$ cm^{-3}) compared to what is typically observed in IRDCs. Despite their high luminosities, the HMPOs could not form detectable H II regions, typically due to the lack of ionizing photons and being deeply enveloped in gas clouds. It is believed that they harbor centrally located, unresolved cores that are internally heated.

Hot molecular cores (HMCs), as discussed by Kurtz et al. (2000) and Cesaroni (2005), are considered the precursors of high-mass stars. These cores are notable for their rich chemistry, resulting from the evaporation of dust grain mantles due to the intense radiation from deeply embedded early-type stars Beltrán & Rivilla (2018). The HMCs exhibit small sizes (diameters $\leq$ 0.1 pc), high densities ($n \geq 10^7$ cm^{-3}), elevated temperatures ($T \geq$ 100 K), and significant extinction ($A_V \geq 100$ mag) within molecular cloud cores (Nomura & Millar, 2004). The observed high molecular densities in HMCs are regarded as indicators of ongoing high-mass star formation, generating a substantial mass of high-temperature gas. The HMCs are characterized by actively accreting protostars, marking a phase before the development of H II regions, as exemplified by the work of Kurtz et al. (2000) and Beuther et al. (2006).

2.4.3 H II regions

H II regions form through the ionization of hydrogen within gas clouds. The transition from neutral to ionized hydrogen takes place when exposed to intense UV radiation beyond the

Lyman limit (13.6 eV, assuming that hydrogen is in its ground state). Given that only high-mass stars produce a significant number of Lyman-continuum photons, H II regions serve as indicators of massive star formation (Hoare et al., 2007). Optimal observations of H II regions occur in radio and infrared wavelengths, as they are characterized by thermal emission from free-free radiation and dust surrounding the ionized region.

Based on their size and electron density, H II regions are categorized into Hypercompact (HCHR), Ultracompact (UCHR) (Kurtz, 2005; Hoare et al., 2007), compact (CHR), and classical/extended regions (Mezger et al., 1967; Yorke, 1986). Both HCHR and UCHRs represent small, developing zones of ionized gas around newly formed massive stars. The HCHRs are notably smaller than UCHRs, suggesting that the former encapsulates ionized gas around a single star, while the latter corresponds to a stellar cluster (Kurtz, 2005). On the other hand, compact and classical H II regions are the results of the hydrodynamical expansion of the ionized gas, leading to the disruption of the parent molecular cloud. This event exposes embedded high-mass and low-mass stars, making them observable in optical and near-infrared wavebands (Carpenter et al., 1990; Zinnecker et al., 1993).

2.5 Studying high-mass star-forming regions

The massive star-forming regions within our Galaxy are recognized as hubs for intricate physical and chemical processes, particularly involving dust grains. In the initial phases of massive star formation, prior to the establishment of an embedded heating source, these regions exhibit robust emissions of cold dust and gas at FIR/sub-millimeter wavelengths. The dust plays a critical role in radiating at these wavelengths, making it an essential tracer of the early stages of star formation. In contrast, the MIR emission is very weak or not detected since the dust cocoon has not yet been heated (Beuther et al., 2007b). As the cold, dense cores collapse and begin to heat up, the dust temperatures rise, marking the commencement of the hot core phase, where MIR radiation from the dust becomes more prominent.

The MIR spectrum is particularly valuable because it provides exclusive access to rovibrational transitions, especially for molecules that lack a permanent dipole moment and are invisible in traditional radio and millimeter observations. These transitions allow us to probe deeper into the chemistry and kinematics of the warm gas and dust in the immediate vicinity of embedded protostars. By studying the rovibrational transitions, we can trace the detailed physical conditions such as the temperature, density, and even the velocity structure of the gas in the hot core phase and understand how protostars influence their

surroundings as they heat and ionize the surrounding dust and gas.

Thus, surveys at various wavelengths, including FIR and MIR, are essential for exploring high-mass star-forming regions. FIR and sub-millimeter surveys detect the cold, massive molecular cloud cores, while MIR observations are key to revealing the hot dust and the associated chemical processes through rovibrational transitions. Specifically, MIR surveys allow the identification of hot molecular cores–regions where dust temperatures have increased due to the presence of a forming protostar—and the study of their chemical makeup. In addition to providing insights into the warm dust, these MIR transitions are crucial for identifying high-mass protostellar objects (HMPOs) at a stage when ionized hydrogen has not yet formed around the protostar.

As these protostars evolve into UCHRs, the dust cocoon continues to radiate strongly in the MIR and FIR, while radio wavelengths become important for detecting ionized gas. Surveys targeting UCHRs rely on both continuum and RRL features to map out the star-forming regions. Radio continuum surveys, in particular, are highly effective at locating these UCHRs, which emit strongly at radio wavelengths.

In addition to these broad surveys, an effective approach to trace high-mass star formation involves observing astronomical masers, the microwave counterparts of lasers occurring naturally in interstellar space. Different masers indicate distinct evolutionary stages of massive star formation, including the elusive early stages (Ellingsen, 2004). Bright and compact, masers are ideal for investigating the kinematics and physical conditions within massive star-forming regions at milli-arcsecond resolution.

2.6 Challenges in probing high-mass star-forming regions

Observational exploration of processes involved in high-mass star formation faces significant challenges, particularly in the prestellar (before the onset of stellar activity) and protostellar (during the assembly process of the star) stages. Several factors contribute to these limitations:

1. Short timescales: The rapid evolution of high-mass stars makes it challenging to detect and study various stages comprehensively.

2. Stellar IMF: The rarity of massive stars, dictated by the IMF, implies that they are statistically found at greater distances from the Sun (beyond $\sim$1 kpc), necessitating high-angular resolution observations.

3. Embedding in parent clouds: Massive protostars are deeply embedded in their parent clouds, preventing direct observations at optical or near-infrared wavelengths due to high

extinction.

4. Clustered environments: High-mass stars are predominantly situated in clustered environments, and their influence on the local/primordial environment adds complexity to observational studies.

Despite these challenges, significant progress has been made in recent years. Advances in sensitivity and angular resolution across the electromagnetic spectrum enable deeper observations into massive star-forming regions. Comprehensive reviews by Motte et al. (2018) and Tan et al. (2014) provide valuable insights into the recent observational and theoretical landscape of massive star formation.

Chapter 3

H II regions

High-mass stars exert significant influence on the surrounding ISM due to their radiative, mechanical, and chemical impacts. The observable outcomes of the dynamic interaction between high-mass stars and the neighboring ISM serve as crucial indicators for investigating the diverse evolutionary stages associated with their birth. While the early stages are associated with the presence of jets and outflows, the late stages are more prominent due to the ionization of the adjacent neutral medium by UV photons from the massive star, leading to the formation of H II regions (Wood & Churchwell, 1989; Churchwell, 2002). The H II region surrounding a recently formed massive star expands into the ambient ISM, propelled by various feedback mechanisms such as thermal overpressure, potent stellar winds, radiation pressure, or a combination of these factors (Churchwell et al., 2006; Deharveng et al., 2010).

For the creation of a H II region within a molecular cloud, the dissociation of molecular hydrogen (H_2) followed by the ionization of neutral atomic hydrogen (H I) is necessary. The first process requires photons with energies greater than 4.48 eV, while ionization demands energies exceeding 13.6 eV. In the initial stage of massive star formation, an H II region does not yet exist surrounding the massive star. This is followed by a brief formation period and then a gradual expansion. As the H II region expands, ionization occurs alongside recombination.

When the radius of the ionization front, R, is still small, the massive star's ionizing photon flux surpasses the recombination rate, allowing additional photons to reach the ionization front and continue ionizing the surrounding neutral medium. During this phase, the ionization front expands very quickly, with its speed surpassing the isothermal sound speed within the region. Also, in this phase, the expansion of the ionization front is more due to the photo-ionization rate being greater than the recombination rate compared to the pressure-driven expansion phase (later) of the bubble. Consequently, the ionization front

spreads isotropically into the surrounding space, forming what is known as a Strömgren sphere. The radius of this sphere (R_s) can be calculated as

$$R_s = \left(\frac{3\, N_{Ly}}{4\, \pi\, n_H^2\, \alpha_{rec}} \right), \tag{3.1}$$

where N_{Ly} is the Lyman-continuum photon rate from the central star, n_H is the neutral hydrogen number density, and α_{rec}[1] is the recombination coefficient.

Photons with energies below 13.6 eV escape without ionizing the gas. However, a significant portion of these photons have sufficient energy to dissociate the surrounding molecular region, leading to the formation of a photo-dissociation region (PDR). Both the H II region and the PDR are constrained by the photon flux that meets the necessary energy requirements (Whittet, 1992; Stahler & Palla, 2004). For example, considering a massive star of spectral type O6V, emitting N_{Ly} = 10^{49} photons per second, situated within a neutral medium with a density of 10^4 cm^{-3}, the initial expansion phase lasts approximately 50 years, and by the end of this phase, the radius of the Strömgren sphere is around 0.15 pc (Deharveng et al., 2010). Thus, initially, the H II regions expand rapidly outwards as the ionization front moves through the ISM. However, the flux of ionizing photons reduces with increasing distance, and the initial fast expansion phase halts when the rate of ionization equals the recombination rate.

After the initial phase, a prolonged expansion phase occurs, driven by the pressure difference between the regions. The pressure in the warm ionized gas ($T_e \sim 10^4$ K) is significantly higher than in the cold neutral medium ($T_e \sim 10$ – 100 K). As the radius (R) approaches the Strömgren radius (R_s), the speed of the ionization front slows down, allowing the pressure difference to initiate the second phase of expansion. Fig. 3.1 from Deharveng et al. (2010) illustrates this second expansion phase. During this phase, the velocity of expansion (because of the difference in pressure between the H II region and surrounding neutral medium) exceeds the speed of sound in the neutral medium, creating an expanding shock in the neutral medium. This process compresses the surrounding neutral material into a thin shell that bounds the H II region. As UV photons continue to flow in, the mass of the ionized gas keeps increasing while the density decreases due to the ongoing expansion. This second phase of expansion continues until pressure equilibrium is reached.

The evolutionary sequence (see Table 3.1 for details) of H II regions begins with deeply embedded hypercompact structures, which then undergo expansion to form ultracompact,

[1]It is calculated by excluding the n=1 state because if an electron recombines directly to the ground level, the released photon will be capable of ionizing another hydrogen atom.

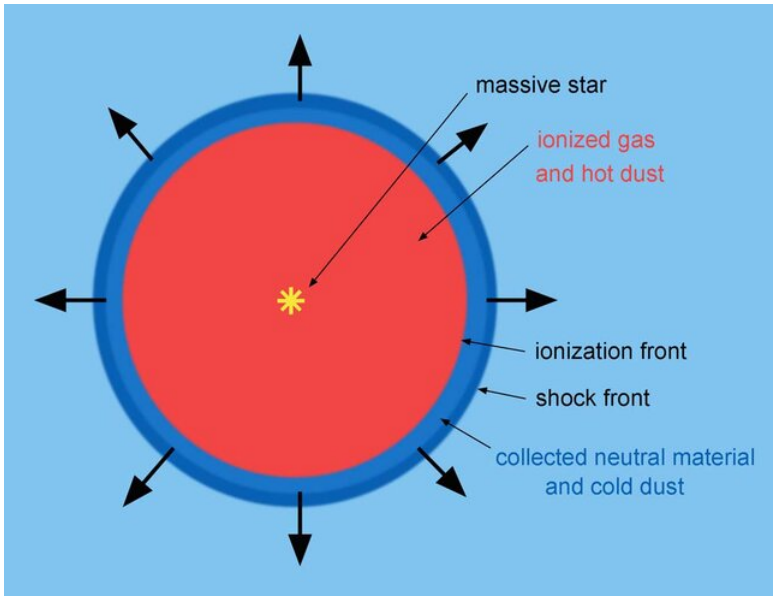

Figure 3.1: Image showing the second phase of expansion of a spherical H II region. Image credit: Deharveng et al. (2010)

Table 3.1: Physical properties of various evolutionary stages of H II regions. The inputs are taken from Kurtz (2005)

Type	Diameter (pc)	Ionized mass ($M_\odot$)	Density (cm^{-3})	Emission measure (pc cm^{-6})
Hypercompact	~ 0.03	$\sim 10^{-3}$	$\gtrsim 10^6$	$\gtrsim 10^{10}$
Ultracompact	$\lesssim 0.05$	$\sim 10^{-2}$	$\gtrsim 10^4$	$\gtrsim 10^7$
Compact	$\lesssim 0.5$	~ 1	$\gtrsim 5 \times 10^3$	$\gtrsim 10^7$
Classical	~ 10	$\sim 10^5$	$\sim 10^2$	$\sim 10^2$
Giant	~ 100	10^3 – 10^6	~ 30	$\sim 10^6$
Supergiant	> 100	10^6 – 10^8	~ 10	$\sim 10^5$

compact, and classical H II regions. The commencing phase of this sequence is intimately tied to the formation process, occurring when the recently formed massive star is still accreting material. In contrast, the classical H II regions are predominantly associated with more evolved objects. Moreover, when an H II region is situated on the outer periphery of a large molecular cloud, it has the potential to trigger star formation. A notable example is found behind the luminous Orion Nebula, where within the deeper recesses of the cold Orion molecular cloud, the ongoing formation of new stars is taking place. Although the current stars in this region are not yet massive and hot enough to generate their own H II regions, it is anticipated that some of them will eventually reach this stage.

H II regions are most effectively detected through infrared or radio wavelength observa-

tions. The central source's radiation heats the dust that then re-emits in the infrared, peaking around ~ 100 μm. By analyzing the shape and peak of the dust SED, one can infer the dust temperature, which reveals the heating effects of nearby massive stars and the presence of cooler, more extended structures such as PDRs. Furthermore, the SED allows for the estimation of dust mass, which, when combined with a gas-to-dust ratio, provides a measure of the molecular gas mass, thereby giving insight into the material reservoir available for ongoing star formation. Variations in the SED also indicate differences in dust composition and grain size, such as the presence of polycyclic aromatic hydrocarbons (PAHs) identified by specific mid-infrared features. The dust SED can also trace star formation activity by revealing warm dust heated by embedded YSOs and protostars, helping to characterize the embedded stellar population and its interaction with the surrounding medium.

At wavelengths greater than 3 mm, the emission from dust rapidly declines, and the 'free-free' radio emission from the ionized gas becomes the dominant emission. At radio wavelengths, under the Rayleigh-Jeans limit, the flux S_ν at a frequency ν is given by

$$S_\nu \approx \frac{2\,k}{c^2}\,\nu^2\,T_e\,\tau_\nu\,\Omega_s, \qquad \text{when} \;\; \tau_\nu \ll 1, \tag{3.2}$$

$$S_\nu \approx \frac{2\,k}{c^2}\,\nu^2\,T_e\,\Omega_s, \qquad \text{when} \;\; \tau_\nu \gg 1, \tag{3.3}$$

where T_e is the electron temperature, τ_ν is the optical depth, and Ω_s is the solid angle of the H II region in steradians. The optical depth, τ_ν, determines (for the most part) the shape of the free-free part of the spectrum, and it is expressed as

$$\tau_{\rm C}(\nu) \approx 3.014 \times 10^{-2} \left(\frac{T_e}{\rm K}\right)^{-1.5} \left(\frac{\nu}{\rm GHz}\right)^{-2} \left(\frac{EM}{\rm pc\,cm^{-6}}\right) \langle g_{ff}\rangle, \tag{3.4}$$

where EM (= $\int n_e^2 ds$, where n_e is the electron density.) is the emission measure, and $\langle g_{ff}\rangle$ is the free–free Gaunt factor (Brussaard & van de Hulst, 1962) given as

$$\langle g_{ff}\rangle \approx \ln\left[4.955 \times 10^{-2} \left(\frac{\nu}{\rm GHz}\right)^{-1}\right] + 1.5\,\ln\left(\frac{T_e}{\rm K}\right). \tag{3.5}$$

Altenhoff (1961) found a good numerical approximation of eq. 3.4 and it is expressed as

$$\tau_{\rm C}(\nu) \approx 8.235 \times 10^{-2} \left(\frac{T_e}{\rm K}\right)^{-1.35} \left(\frac{\nu}{\rm GHz}\right)^{-2.1} \left(\frac{EM}{\rm pc\,cm^{-6}}\right), \tag{3.6}$$

In the optically thin regime (eq. 3.2), $S_\nu \propto \nu^{-0.1}$, while in the optically thick regime

(eq. 3.3) $S_\nu \propto \nu^2$.

In addition to the radio continuum emission, H II regions also emit RRLs. The RRL emission from H II regions arises from the electronic transitions between high-n levels (typically n $>$ 100) of hydrogen atoms. These lines occur at radio wavelengths and are hence not affected by dust extinction, making them excellent probes for studying the kinematics, density, and temperature of H II regions. The line emission is generally optically thin, and the intensity is directly proportional to the emission measure. RRLs are valuable for determining the electron temperature (T_e) of H II regions, which can be estimated from the ratio of RRL to continuum emission, as both arise from the same ionized gas. The full width at half maximum (FWHM) of the RRLs provides information about the velocity dispersion within the ionized gas. For those H II regions that are in their early stages of evolution, such as HCHR, the FWHM is typically broad (40 km s^{-1} or greater) due to high turbulence, thermal motion, pressure broadening and other systematic motions (Sewilo et al., 2004; Hoare et al., 2007; Keto et al., 2008). As the H II regions expand and evolve into a more diffuse state, the FWHM decreases (down to ~ 20 km s^{-1}) due to the dissipation of the systematic and turbulent motions, and, consequently, the H II regions gradually attain a more stable configuration, where turbulent motions are less dominant (Kim & Koo, 2001).

Observations at the radio and infrared wavelengths are less impacted by extinction effects, such as scattering and absorption by interstellar dust, compared to those at the optical and ultraviolet wavelengths. Hence, studies at the radio and infrared wavelength regimes enable a deep exploration into star-forming clouds, unveiling processes related to the formation of massive stars. Complementary studies at the near-infrared (NIR) wavelengths contribute to a comprehensive census of the associated young stellar population. For in-depth insights into the physical properties and nature of H II regions, excellent reviews can be found in works such as Wood & Churchwell (1989), Garay & Lizano (1999), Churchwell (2002), and Hoare et al. (2007).

Interestingly, the observed H II regions seldom display the perfect spherical shape that the above scenarios would suggest. Wood & Churchwell (1989) conducted a survey of the Galactic Plane for UCHRs and categorized them based on their morphology. Their findings revealed that 20% had spherical shapes, 16% exhibited core-halo morphologies, 4% had shell structures, 17% were irregular, and 46% were unresolved. It is believed that a significant amount of mechanical energy is contributed to the local environment by the stellar winds even before a UCHR forms. These winds are often considered to explain the spherical shell morphologies that are rare by nature. When combined with the gradients in pressure in the surrounding gas, they may also account for cometary and

irregular morphologies (Castor et al., 1975; Shull, 1980). Additionally, the central star or star cluster's motion through the ambient medium could also be responsible for creating cometary morphologies (Mac Low et al., 1991).

Both UCHRs and their evolved phase CHRs are critical for understanding massive star formation and feedback as they mark the early stages of interaction between the massive stars and their environment. The radio continuum flux (S_ν at frequency ν) observed towards the H II regions, in general, allows us to estimate the rate (N_{Ly}) of Lyman-continuum or ionizing photons (energy $\geq$ 13.6 eV) emanating from their central star or star cluster. Following Schmiedeke et al. (2016), in the optically thin limit, the $N_{\rm Ly}$ can be estimated as

$$N_{Ly} \geq 4.76 \times 10^{42}\ \nu^{0.1}\ d^2\ S_\nu\ {T_{\rm e}}^{-0.45}, \tag{3.7}$$

where S_ν is the flux density in Jy at the frequency ν in GHz, d is the distance to the H II region in pc, and $T_{\rm e}$ is the electron temperature of the ionized gas in K.

However, not all Lyman-continuum photons will contribute to the ionization of hydrogen. A significant fraction of these photons can be absorbed by the dust grains inside the H II region. Dust absorption reduces the quantity of ionizing photons available for interaction with hydrogen atoms, affecting the region's overall ionization structure. This process also leads to the heating of dust, contributing to the infrared radiation observed from the H II regions. Thus, the rate of ionizing photons can also be estimated by observing the dust emission of H II regions at the infrared wavelengths, as the radiation from the central star or star cluster is reprocessed into infrared emission by the dust particles surrounding the H II regions. In order to calculate the ionizing photon rate (N_{Ly}^{IR}) using the infrared data, first, we need to estimate the total infrared luminosity (L_{IR}^{dust}) using the MIR and FIR flux densities. The quantity, L_{IR}^{dust}, is again derived by fitting a SED function to the observed MIR and FIR flux densities. Next, by utilizing the following expression from Inoue et al. (2001), we can calculate the fraction (f) of Lyman-continuum photons contributing to the ionization of hydrogen

$$\left(\frac{L_{IR}^{dust}}{L_\odot}\right)\left(\frac{5.63 \times 10^{43}\,{\rm s}^{-1}}{N_{Ly}}\right) = \frac{1-0.28f}{f}. \tag{3.8}$$

This fraction, f, is directly related to the N_{Ly}^{IR} by the equation

$$f = \frac{N_{Ly}}{N_{Ly}^{IR}}. \tag{3.9}$$

Hence, by using the values of f and N_{Ly}, one can estimate the ionizing photon rate at the infrared wavelengths.

The first extensive survey for UCHRs was undertaken by Wood & Churchwell (1989), who used radio observations (using VLA) at a high angular resolution to detect 75 UCHRs. However, surprisingly, Wood & Churchwell (1989) found that the rate of ionizing photons derived from the radio was much lower ($\sim$ 90%; see their Table 18 for details) than that from the infrared (estimated utilizing data from the *Infrared Astronomical Satellite*). A similar discrepancy was also found in the later work of Kurtz et al. (1994) (see their Table 7 for details), and both works attributed the discrepancy to the dust particles inside the UCHRs absorbing the ionizing photons.

Alternatively, Kurtz et al. (1994) proposed another explanation involving a stellar cluster to account for the aforementioned discrepancy. If the stars in a cluster follow a typical IMF law (e.g., Kroupa 2001), the several low-mass stars would accompany the high-mass stars. These stars would increase the infrared luminosity, but the production of ionizing photons will not be increased significantly. Nevertheless, using the IMF law from Kroupa (2001) along with the mass-luminosity relation for main sequence stars (Salaris & Cassisi, 2005), it is found that the massive stars contribute more than 90% of the total luminosity. As a result, a stellar cluster does not substantially change the statistical relationship between ionizing photon rates derived assuming only massive stars from radio and infrared observations.

Subsequent studies by Kurtz et al. (1999), Kim & Koo (2001), Ellingsen et al. (2005), and de la Fuente et al. (2020) demonstrated that diffuse radio continuum emission associated with UCHRs might help resolve the discrepancy in Lyman-continuum photon rates. This extended emission often goes undetected because interferometric observations are typically insensitive to emission on scales larger than the shortest baseline of the instrument (see Fig. 3.2). Including this extended emission leads to significantly higher radio continuum fluxes, which, in turn, yield larger Lyman-continuum photon rates, bringing them nearer to those estimated from the infrared data. This minimizes the requirement for the high dust absorption proposed by Wood & Churchwell (1989) and Kurtz et al. (1994). A similar scenario could apply to CHRs, where the non-detection of extended emission around compact cores remains may potentially cause overestimation of dust absorption (Habing & Israel, 1979).

Including the diffuse emission may also help address the "age problem," which arises from the fact that UCHRs would need to remain in their ultracompact phase much longer than their sound crossing time in a homogeneous medium. Based on their sizes, mod-

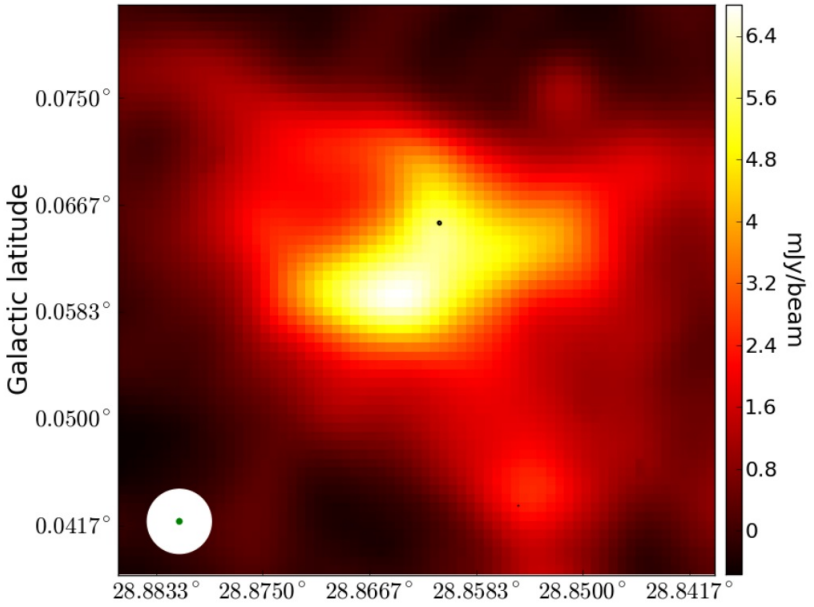

Figure 3.2: Image showing a source example of the differences between the two sets of VLA images, D-configuration (background), and B-configuration (5σ-level contours). As the D-configuration is more compact and hence contains more short baselines than the B-configuration, the latter configuration has picked very little radio emission (black point). Image credit: Dzib et al. (2023)

els suggest that UCHRs should expand and dissipate quickly due to the pressure-driven expansion of ionized gas into the surrounding medium (e.g., Franco et al. 1990; Tenorio-Tagle 1979). However, these regions persist for much longer, with lifetimes extending up to several hundred thousand years (Wood & Churchwell, 1989; Kurtz et al., 2000). This discrepancy points to the potential influence of additional physical mechanisms, such as confinement by stellar winds, magnetic fields, or external pressure (Keto, 2002; Peters et al., 2010). Detecting extended emission around UCHRs could provide a crucial piece of the puzzle, implying that these regions are not as young as they seem when only the UCHR is observed. The presence of extended emission would suggest that ionized gas has expanded beyond the ultracompact core, indicating a more evolved stage of development and offering insights into the prolonged lifetimes of H II regions (Kim & Koo, 2001).

In conclusion, H II regions are clear indicators of massive star formation, as they are one of the phenomena that have a physical association only with the birth of massive stars. Also, due to the short timescales involved in the formation of massive stars and their tendency to form in clusters, molecular clouds hosting H II regions probably also host massive young stellar objects at their preliminary stages of evolution (Kurtz et al., 2000). However,

a few long-standing problems associated with them still require further investigation. Advancing our understanding of these obstacles through multi-wavelength studies is crucial for enhancing our knowledge about the H II regions.

Chapter 4

Observation and data analysis techniques

The primary objective of this thesis is to conduct comprehensive multi-wavelength studies of several Galactic UCHRs and CHRs. This has been achieved through the utilization of data across radio, sub-mm, FIR, MIR, and NIR wavelengths. In this chapter, we focus on the multi-wavelength data analysis techniques employed. First, we will go through the details of radio observations and data reduction procedures. Then, various data products from multiple archives, which have been utilized to investigate the different phases and components associated with the high-mass star-forming complexes, will be discussed. Next, we discuss the methodologies adopted for generating the maps of column density and dust temperature utilizing the far-infrared cold dust emission data. We also discuss the procedures adopted for subtracting the point sources at the MIR wavelengths, which are required to construct the SED of dust emission. Then, the techniques for fitting a dust SED using MIR and FIR data are briefly described. Finally, we explain the methodologies used to identify the candidate ionizing stars.

4.1 Radio observation and data analysis

4.1.1 uGMRT observation

To investigate the ionized gas associated with the star-forming regions of interest, a low-frequency radio continuum mapping was performed using the *upgraded Giant Metrewave Radio Telescope* (uGMRT), located in Pune, India. The uGMRT features a hybrid configuration consisting of 30 antennas arranged in a 'Y' shaped array. Each antenna is a 45-meter diameter parabolic dish. The central square contains 12 antennas randomly distributed within an area of 1×1 km^2, with the shortest baselines of approximately 100 meters, making it sensitive to large-scale emission. The other 18 antennas are distributed

in three arms, with six antennas in each arm. The maximum baseline achievable with the uGMRT is about 25 km, providing high angular resolution ($\sim 2''$ at 1.28 GHz). Further details about the uGMRT configuration can be found in Swarup (1990). Fig. 4.1 illustrates the location and 'Y' shaped array configuration of the uGMRT, along with a close-up view of one of its antennas. Compared to other multi-element aperture synthesis interferometers operating at meter wavelengths, the uGMRT offers the largest collecting area. The central square baselines of the uGMRT are comparable in length to the *Karl G. Jansky Very Large Array* (VLA) D-configuration, while the baselines from the arm antennas are similar to the VLA A and B configurations. Consequently, a single observation with the uGMRT samples the (u, v) plane adequately with reasonable sensitivity.

When the sky brightness distribution of the source, $I(l, m)$, is limited to a small region, i.e., the direction cosine, $n \approx 1$, the complex visibility, $V(u, v)$, is the Fourier transform of $I(l, m)$. This is known as the Van Cittert-Zernike theorem, which can be expressed mathematically as

$$V(u, v) = \int I(l, m)\, e^{-i2\pi[lu+mv]}\, dl\, dm, \tag{4.1}$$

where (u, v) are the baseline coordinates, and (l, m) are the direction cosines. Thus, to reconstruct the sky brightness distribution of the source, one needs to perform an inverse Fourier transform on the measured and calibrated visibilities of the source, which is the time-averaged spatial correlation of the signal at the observer's plane. However, practically, this process is not so straightforward, as the measurements may get corrupted due to multiple external factors, including both instrumental effects (such as the antenna-to-antenna variations in receiver sensitivity, deformations in the shape of the antennas, etc.) as well as propagation effects in the Earth's atmosphere. In addition to that, the radio frequency interference (RFI) originating from man-made objects, such as telecommunication systems, satellites, and aircraft transponders, also corrupts the radio data, especially at the operating frequencies of the uGMRT. Hence, we need to edit and calibrate the measured visibilities before proceeding with the inverse Fourier transform on them.

Before calibrating the $V(u, v)$ of the target source, we use the measured visibility of another source with a known and stable flux density, referred to as a flux density calibrator. Accurate flux density calibration is a fundamental requirement in radio astronomy, as it ensures that the observed intensity of radio sources is quantitatively reliable. Radio telescopes do not inherently provide flux measurements; instead, they record signals that are influenced by a range of instrumental and environmental factors, as mentioned before. These factors can fluctuate over time and across different observing conditions. Calibra-

tion corrects for such effects by comparing observed signals to those from known reference sources, allowing for the precise determination of absolute flux densities. This process is critical for producing data that can be meaningfully compared across different frequencies, observational epochs, and instruments. Without rigorous flux density calibration, scientific interpretations, such as the characterization of emission mechanisms or the derivation of physical parameters from radio data, would lack the necessary accuracy for robust conclusions.

Additionally, the complex antenna-based gains can vary over time, primarily due to changes in the Earth's atmosphere. To correct for these variations, periodic observations of another source, typically unresolved, are required; this source is called the gain calibrator. The gain calibrator needs to be as close to the target as possible so that the same region of atmosphere as over the target source is probed by observing the gain calibrator. Similar to the flux density calibration, gain calibration is also a crucial procedure in radio astronomy. Without proper gain calibration, these previously mentioned fluctuations can introduce significant errors in the recorded data, leading to incorrect measurements of source intensities. During the gain calibration process, we generate the calibration solutions utilizing the data from the gain calibrator, which are then used to correct the instrument's gain. The flux density of the gain calibrator is also calibrated against the flux density of the flux calibrator by transferring the flux density calibration solutions. Thus, each observation requires at least one measurement of the flux calibrator and periodic observations of the gain calibrator.

Furthermore, the gain of an antenna also varies with frequency due to several factors related to the antenna's physical size and design. Besides, variations in atmospheric conditions and instrumental factors, such as the bandpass filter, feed design, and system noise, can also influence the antenna's gain performance across different frequencies. Thus, we also need to correct for the fluctuations in the frequency-dependent part of the antenna-based gain. For this purpose, we perform a bandpass calibration. An effective bandpass calibration is crucial for detecting and accurately measuring spectral features, particularly those that are weak and broad. Also, bandpass calibration can be a limiting factor in the dynamic range of continuum observations. The best targets for this calibration are bright, flat-spectrum sources with featureless spectra. The generated bandpass calibration solutions are utilized to make the shape of the passband flat or, in other words, to keep the gain of the antenna constant across the observing band.

In our observations, we used the VLA calibrators 3C286 and 3C48 as the flux and bandpass calibrators and J1911–201 and J1822–096 as the gain calibrators. The flux calibrator was observed for approximately 10–15 minutes at the beginning and end of each observa-

tion sequence. The gain calibrator was observed periodically in conjunction with the target source. During each period, the target was observed for about 25–35 minutes, followed by a 5-minute observation of the gain calibrator.

4.1.2 Data Analysis

We have used the NRAO Common Astronomy Software Applications (CASA; McMullin et al. 2007) tool to analyze the radio data. Fig. 4.2 shows the overall flowchart consisting of the steps for data editing, calibration, and imaging. A brief description of our data analysis procedure is given below.

1. The uGMRT data are recorded in "lta" format. In order to work in CASA, we need to convert these into the CASA readable format, which is called the "measurement set" (MS) format. For this purpose, the "lta" format data is first converted to the FITS format using pre-compiled binary files "listscan" and "gvfits" from the observatory. Next, We use the CASA task `importuvfits` to convert data from the FITS to MS format.

2. The task `listobs` provides us with a summary of the contents of the dataset in the logger window. The summary includes a description of the targets, including the calibrators, details on the scans, and details on the spectral window used, including the central frequency and number of channels.

3. Any interferometric array requires a small amount of time, in the beginning, to stabilize its components. Consequently, the standard practice is to remove the initial data points from each scan. We call it "quack" flagging. Similarly, the last few recordings of each scan are also "quack" flagged to avoid any discontinuity arising from switching the array from the source to the calibrator or vice versa. The task `flagdata` is used (with mode = "quack") to achieve this.

4. Now, having done some basic editing based on known information, it is time to look at the data using the `plotms` tool to determine if there are any other bad data such as dead antennas, bad baselines, bad time range, spikes, RFI, etc. The details of such bad data are recorded in a "flagfile".

5. Task `flagdata` is used to manually flag these bad data based on the input "flag file." At this stage, the usual data viewing and flagging techniques focus on the calibrators

to determine various corrections from them and then apply these corrections to the science data.

6. The next step is to provide a flux density value for the flux calibrators, 3C48 and 3C286, for our case. Later, during the final steps of the data calibration process, we will use this information to transfer the scaling of flux density to the gain calibrators. The task `setjy` is used to set the flux density for the flux calibrators used in our observation.

7. Next, we start our data calibration procedure by performing an antenna-based delay calibration using the task `gaincal` (gaintype="K"). In all calibration procedures, we provide a reference antenna, which worked for the entire duration of the observation. Nevertheless, this delay calibration procedure solves the relative delays between each antenna and the reference antenna and generates a "delaycal" table containing the solved delays.

8. We perform an initial phase-only gain calibration before doing any bandpass calibration. The reason for performing this step before the bandpass is to average over the (typically not large) variations of phase with time in the bandpass. This is achieved using the task `gaincal` (gaintype="G"). This creates a "gantable" that contains initial phase solutions.

9. After solving for the initial gain, we iteratively check and flag the bad data from the flux calibrator using the tasks `applycal`, `plotms`, `clearcal`, and `flagdata` in sequence.

10. The antenna-based gain solutions also vary across the passband. Hence, we require a bandpass solution to negate the gain variations over frequency channels. For this purpose, we use the `bandpass` task to generate the "bandpass" table containing the bandpass solutions. Next, we check for the quality of bandpass solutions using the task `plotms`. For acceptable solutions, the amplitude of the bandpass should be nearly constant with frequency. However, some variation in amplitude is admissible as long as the change is smooth.

11. Now that we have a bandpass solution to apply, the forward step is to derive the final complex antenna gain solutions for the calibrators using the "bandpass" table generated in the previous step. The task `gaincal` is used to calculate the gain

solutions for both the flux and gain calibrators. The final amplitude and phase-based solutions for both the calibrators are stored in a separate "gaintable" for later use.

12. Next, we take the flux calibrator (whose flux density was set using `setjy` before) as a reference to estimate the flux of the gain calibrator using the task `fluxscale`. The flux density obtained from this step should be close to the flux listed in the VLA manual.

13. Now, we apply the calibration to each target (including calibrators) using the `applycal` task. We use the generated solution tables in previous steps and the appropriate target source for that particular calibration. For the flux and gain calibrators, all bandpass solutions are the same as for the flux calibrator, and the phase and amplitude-based solutions as derived from their respective visibility data. For the target, we apply the bandpass solution from the flux calibrator and the phase and amplitude-based solution from the gain calibrator.

14. After calibrating the targets, we carefully examine the calibrated visibility data using the `plotms` tool. If any bad data points are present, we flag those using the `flagdata` task. Then, we recalibrate the visibility data by repeating the steps from point 11.

15. Once we are satisfied with the quality of the calibration, we split the sources into individual files using the task `split`. This step is not strictly necessary, as we can always access the calibrated visibility data for each source by mentioning their field ids during the later steps. However, splitting the calibrated data into smaller files reduces the chance of losing the entire data. Also, it is easy to handle individual small files compared to large files, particularly during self-calibration.

16. Next, the data are split into two sets, one for the continuum and another for the spectral line. The latter requires subtraction of the continuum before imaging, which is typically done using the task `uvcontsub`. This task performs continuum fitting and subtraction on a per integration, per baseline, and per correlation basis. Next, it takes a global average to estimate the shape of the subtracted baseline. While this process works well for instruments like the VLA, one encounters problems with the uGMRT, especially when the lines are weak, such as RRLs. This is due to the presence of a residual ripple across the passband even after bandpass calibration, the strength of which is comparable to that of the RRLs. We hence use the task `UVLSF`

from the Astronomical Image Processing System (AIPS), which works well for our purpose since it carries out continuum subtraction locally around each spectral line (as opposed to taking a global average in the end to remove the continuum emission). First, a set of line-free channels (about either side of the spectral line) is provided for the task. Then, `UVLSF` fits a straight line or a polynomial of a certain order using those line-free channels and estimates the shape of the spectral baseline. Finally, `UVLSF` returns two files containing the subtracted visibility data and fitted baseline data as visibilities.

17. Now that we have separated the RRL emission from the total emission, we shift our focus to image the continuum emission (original data with line-free channels). The continuum data are averaged in frequency to decrease the size of the data. However, the data are averaged only such that they are not affected by "bandwidth smearing". The CASA task `mstransform` helps us to achieve this. We again look for bad data after this step, and they are flagged subsequently if found present.

18. The task `tclean` is used for imaging the continuum emission. The first step is to construct the point spread function of the interferometer, called the "dirty beam," which is the inverse Fourier transform of the uv coverage. Given this "dirty beam," we construct a model of the true sky brightness distribution in a process called deconvolution. To accomplish this, we do an inverse Fourier transform of the measured visibility function and generate what is called a "dirty map," which is a convolution of the "dirty beam" and the true sky brightness distribution. Finally, the "true map" is generated from the "dirty map" using the model of the true sky brightness and a "restoring beam." Now, the inverse Fourier transform relation between the visibility function and brightness distribution is applicable only for a narrow field where the sky could be approximated as flat. Thus, if we apply standard 2D inverse Fourier transform to wide-field data such as ours, it will produce artifacts around sources away from the phase center. Hence, we need to segment the sky plane into multiple w-planes, each of which has a field of view that is small enough for the Van Cittert-Zernike theorem to be valid and stitch everything back together after performing the inverse Fourier transform. In general, we set the parameter wprojplanes = –1 to automatically calculate the number of required w-planes within `tclean`. Moreover, during imaging, appropriate weighting of the measured visibilities can improve the dynamic range of the produced image. Given the non-uniform uv coverage, the weighting of the different visibilities is a free parameter. Typically, one may use

"natural", "uniform", and "briggs" weighting schemes, where the first two are at two extremes, with the last one falling in between. In "natural" weighting, the weight is the inverse of the variance and thus gives the best signal-to-noise ratio, whereas in "uniform" weighting, all the uv data points, including those at high values of u and v (which have the poorest signal-to-noise) have the same weight, giving rise to better resolution at the expense of the signal-to-noise. During our imaging, the "briggs" weighting scheme (Briggs, 1995) was used, which can produce images with an intermediate strategy between "natural" and "uniform". Furthermore, we deconvolve and collect the clean components of the true sky brightness model interactively by creating clean masks. We stop this process once the residual image resembles noise. Finally, the collected clean components are restored into a "true map" using a "restoring beam." Also, as we want to self-calibrate the image, we save the generated model.

19. The generated image may contain residual errors even after calibrating the data due to the different sky positions of the target and calibrator, variations in the Earth's atmosphere in between two calibrator scans, etc. Hence, we self-calibrate the data to correct these fluctuations by using the Phase closure and Amplitude closure methods. Self-calibration is an iterative process wherein the cleaned image itself is used as a model to generate calibration solutions that will bring the data closer to the model. Next, the calibrated data are imaged to make a better model, and the process is iterated. The iterations include the tasks `tclean`, `gaincal`, `applycal`, and `tclean` in sequence. We have done 3–5 phase-only and 1–2 amplitude and phase-based self-calibrations. We begin this process from a long solution interval and gradually decrease it during the phase-only iterations. Next, we repeat this process for self-calibration based on both amplitude and phase.

20. We image the continuum-subtracted RRL data using the task `clean`. As the RRL emission from our target is arising from extended components, the task `clean` is run interactively. As with the case of continuum imaging, we stopped the deconvolution process once the residual image resembled the noise. We also set the rest frame, rest frequency, and LSR velocity information to correct for the Doppler shift. We also apply the solutions generated during self-calibration of the radio continuum in order to obtain self-calibrated RRL images.

21. Once the final image is obtained, we use the task `wbpbgmrt` to do a primary beam correction.

4.2 Archival data

4.2.1 Radio data

Data from *The HI/OH/Recombination line survey of the inner Milky Way* (THOR; Beuther et al. 2016) survey are utilized to supplement the uGMRT observations. The THOR survey was conducted with the *Karl G. Jansky Very Large Array* (VLA) in its C-configuration and utilized the WIDAR correlator to cover the 21-cm H I line, 4 OH lines, 19 RRLs, and continuum emission within 1–2 GHz in full polarization. Six different spectral windows were employed to observe the continuum emission within 1–2 GHz. Given the variations in angular resolution with frequency, all continuum images were smoothed to a uniform resolution of $25''$. To enhance the signal-to-noise ratio, the detected RRLs were stacked, resulting in final RRL maps with an angular resolution of $40''$ and a velocity resolution of 10 kms^{-1}.

We have also utilized radio data from the GLOSTAR survey (Medina et al., 2019; Brunthaler et al., 2021). Both D and B-configurations of VLA are used to conduct this survey, employing a correlator setup that captures continuum emission in full polarization within the 4–8 GHz range (using two 1 GHz sub-bands centered at 4.7 and 6.9 GHz). The 6.7 GHz methanol maser line, the 4.8 GHz formaldehyde line, and 7 RRLs are also covered in this survey. The information about zero-spacing was obtained using the 100-m Effelsberg radio telescope. The procedures used in calibration and imaging of the GLOSTAR survey data are described in Brunthaler et al. (2021). The survey's data products include images from the D-configuration alone (hereafter GLOSTAR-D; Medina et al. 2019), B-configuration alone (hereafter GLOSTAR-B; Dzib et al. 2023; Yang et al. 2023), combined B and D-configurations, and D-configuration combined with the Effelsberg telescope (hereafter GLOSTAR-D+Eff; Dokara et al. 2023).

The radio continuum data from GLOSTAR-D and GLOSTAR-B consist of a single continuum image at an effective frequency of 5.79 GHz, along with eight sub-band images suitable for spectral index measurements. Due to the frequency dependence and location on the sky, all continuum images are restored with circular beams of $18''$ for the D-configuration and $1''$ for the B-configuration. The GLOSTAR-D data can detect structures up to $\sim 2'$ in size, while GLOSTAR-B is limited to $4''$ due to imaging constraints that consider data only with uv-ranges greater than 50 kλ. The GLOSTAR-D+Eff continuum image has an effective frequency of 5.85 GHz and an angular resolution of $18''$. Given their weak signal strength, the RRLs are imaged only in the D-configuration (Khan et al., 2024).

All detected RRLs are stacked to enhance the signal-to-noise ratio, resulting in a final RRL map with an angular resolution of 25″ and a velocity resolution of 5km s^{-1}.

Along with the radio data from THOR and GLOSTAR surveys, we have used radio data from the *Co-Ordinated Radio 'N' Infrared Survey for High-mass star formation* (CORNISH; Hoare et al. 2012; Purcell et al. 2013) and *Multi-Array Galactic Plane Imaging Survey* (MAGPIS; Helfand et al. 2006) surveys. The CORNISH survey is a high-resolution (1.5″) radio continuum survey of the inner Galactic plane at 5 GHz, conducted using the VLA. This blind survey is targeted towards the northern *Spitzer*-GLIMPSE I[1] region, covering a range of $10^\circ < l < 65^\circ$ and $|b| < 1^\circ$ with comparable resolution. The MAGPIS survey is a high-resolution ($\sim$ 6″ at 20 cm) radio continuum survey of the Galactic plane conducted with the VLA and the Effelsberg 100-m radio telescope. MAGPIS covers the region $5^\circ < l < 48^\circ$ and $|b| < 0.8^\circ$ at wavelengths of 6 cm (4.85 GHz), 20 cm (1.4 GHz), and 90 cm (330 MHz). Both of these surveys provide a detailed view of the Galactic plane's ionized structures.

4.2.2 Molecular line data

We have utilized ^{12}CO (J=3−2) data from the *CO High-Resolution Survey* (COHRS; Dempsey et al. 2013; Park et al. 2023) to investigate the molecular environment. The COHRS observations were conducted using the *Heterodyne Array Receiver Programme* (HARP; 325–375GHz) receiver mounted on the *James Clerk Maxwell Telescope* in Hawaii. The survey offers data products with a velocity resolution of 1 km s^{-1} and an angular resolution of 16″, along with a typical rms noise level in antenna temperature of approximately 1 K. In addition, we have used NH_3 (1,1) line emission data from the *Red MSX survey* (RMS; Urquhart et al. 2011). This survey utilized the 100-m *Green Bank Telescope* to detect 22–24 GHz H_2O maser and NH_3 (1,1), (2,2) and (3,3) line emission towards $\sim$ 600 RMS sources situated within the northern Galactic plane.

4.2.3 Polarized dust emission data from the *Planck* telescope

The *Planck* 353-GHz (850 μm) dust continuum polarization data (Planck Collaboration et al., 2015) are used to determine the orientation of the magnetic field lines on the plane of the sky. This dataset includes Stokes I, Q, and U maps obtained from the *Planck* Public

[1]This program is a part of the original *Galactic Legacy Infrared Midplane Survey Extraordinaire* (GLIMPSE; Churchwell et al. 2006) survey.

Data Release 3 full mission maps, along with the PCCS2 Catalog[2].

We begin by following the IAU convention, i.e., the position angle, $\theta_{GAL} = 0^{\circ}$, points Galactic North but increases towards Galactic East, and the values of subsequent θ_{GAL} are estimated using the expression

$$\theta_{GAL} = 0.5 \times \tan^{-1}(-U/Q). \tag{4.2}$$

Following the position angle transformation relation (Corradi et al., 1998), the magnetic field orientation in Equatorial coordinates can be derived as

$$\theta_B = \theta_{GAL} + \frac{\pi}{2} - \psi, \tag{4.3}$$

where ψ represents the position angle transformation relation between the Equatorial and Galactic coordinate systems at the position of each pixel. It is given as

$$\psi = \tan^{-1}\left[\frac{\cos(l - 32.9^{\circ})}{\cos(b)\cot(62.9^{\circ}) - \sin(b)\sin(l - 32.9^{\circ})}\right]. \tag{4.4}$$

4.2.4 Far-infrared emission data from the cold dust

Data from the *Herschel infrared Galactic Plane Survey* (Hi-GAL; Molinari et al. 2010) are used to construct the spectral energy distribution (SED) of dust emission across mid- to far-infrared wavelengths. The Hi-GAL survey provides far-infrared continuum images at 500, 350, 250, 160, and 70 μm using the *Spectral and Photometric Imaging Receiver* (SPIRE; Griffin et al. 2010) and *Photodetector Array Camera and Spectrometer* (PACS; Poglitsch et al. 2010) cameras on the *Herschel Space Observatory*. For our analysis, we utilized level-2.5 data products from the *Herschel* Science Archive[3]. The Hi-GAL data have varying pixel sizes and resolutions at the five wavelengths of 70, 160, 250, 350, and 500 μm. The pixel sizes are 3.2″, 3.2″, 6″, 10″, and 14″, and the corresponding resolutions are 5″, 13″, 18.1″, 24.9″, and 36.4″ in these wavelength bands, respectively. Additionally, the data are presented in units of Jy pixel^{-1} at 70 and 160 μm, and MJy sr^{-1} at the other wavelengths.

Along with the Hi-GAL data, the 870 μm images from the *APEX Telescope Large Area Survey of the Galaxy* (ATLASGAL; Schuller et al. 2009) are used to identify an IRDC.

[2] `https://irsa.ipac.caltech.edu/applications/planck/`

[3] HPPUNIMAP[B/R]: maps from the combined scan and cross-scan observations, using the `Unimap` task, suitable for extended source analysis; extdPxW: provides monochromatic intensities at 250, 350, and 500 μm, where PxW denotes any of the three arrays, PSW = 250 μm, PMW = 350 μm, or PLW = 500 μm

These observations were conducted using the Large Apex Bolometer Camera (LABOCA), a 295-element bolometer array. The data provide a pixel size of 6″ and an angular resolution of 18.2″.

4.2.5 Mid-infrared emission data from the warm dust

Mid-infrared maps from the *Spitzer Space Telescope* were employed to examine warm dust emission and YSOs in our target H II regions. The *Infrared Array Camera* (IRAC; Fazio et al. 2004) onboard *Spitzer* is one of three focal plane instruments that capture simultaneous broadband images at 3.6, 4.5, 5.8, and 8.0 μm. The pixel sizes across all four bands are 1.2″, with angular resolutions of 1.7″, 1.7″, 1.9″, and 2.0″ at 3.6, 4.5, 5.8, and 8.0 μm, respectively. We used the IRAC mid-infrared maps from the GLIMPSE survey. Additionally, the 24 μm images were obtained from the *Multiband Imaging Photometer* (MIPS; Rieke et al. 2004) instrument as a part of the *MIPS Galactic Plane Survey* (MIPSGAL; Carey et al. 2009) survey, which has a pixel size of 2.5″ and a resolution of 6″.

4.2.6 Near-infrared data from the 2MASS and UKIDSS surveys

The *Two Micron All Sky Survey* (2MASS; Skrutskie et al. 2006) is a comprehensive all-sky survey in three near-infrared (NIR) bands: J (1.25 μm), H (1.65 μm), and K_s (2.16 μm). The survey was conducted using two highly automated 1.3-m telescopes located at Mt. Hopkins, AZ, and CTIO, Chile. Each telescope is equipped with a three-channel camera, with each channel featuring a 256×256 array of HgCdTe detectors, allowing for simultaneous observations in all three bands. For photometric data, the *2MASS Point Source Catalog* (2MASSPSC) is used, retaining only high-quality photometric sources indicated by a "read-flag" of 2, which denotes acceptable photometric uncertainties. These selected magnitudes are utilized to analyze the characteristics of the stellar population and to identify potential ionizing stars associated with the regions of interest.

The *UKIRT Infrared Deep Sky Survey* (UKIDSS; Lawrence et al. 2007) is a deep infrared survey of the northern sky, conducted using the 3.8-m *United Kingdom Infrared Telescope* (UKIRT) located on Mauna Kea, Hawaii. The survey uses the *Wide Field Camera* (WFCAM) to image the sky in five NIR bands: Z (0.87 μm), Y (1.03 μm), J (1.25 μm), H (1.63 μm), and K (2.20 μm). UKIDSS consists of several sub-surveys, each tailored to specific scientific goals, covering different areas of the sky to varying depths. The UKIDSS *Galactic plane survey* provides data with higher sensitivity and resolution compared to its predecessor, 2MASS. The survey data are used extensively to study the stellar populations,

star formation, and structure of the Milky Way, as well as for extragalactic studies.

4.3 Methodologies to estimate the column density and dust temperature from cold dust emission

We analyze the characteristics of cold dust emission in star-forming regions utilizing *Herschel* data spanning 70–500 μm. The emission from dust reaches its peak in the far-infrared range, with the full SED of the cold dust emission being well covered within the *Herschel* wavelengths. To derive the line-of-sight averaged molecular hydrogen column density and dust temperature, we perform pixel-by-pixel fits using a modified blackbody model. However, the resolutions, pixel sizes, and units of the *Herschel* data are different at different wavelengths, and this needs to be made uniform in order to do the SED modeling. Hence, before performing the SED modeling, the data are processed in the *Herschel* Interactive Processing Environment (HIPE)[4] and standardized to the same resolution, pixel size, and unit. The specific steps involved are:

1. The task `Convert Image Unit` in HIPE is used to change the surface brightness units of the SPIRE images from MJy Sr^{-1} to a common unit of Jy pixel^{-1}, matching that of the PACS images.

2. The plug-in `Photometric Convolution` is employed to reproject all the images onto a uniform grid, ensuring a consistent pixel size and resolution of 14$''$ and 36.4$''$, respectively, corresponding to the parameters of the 500 μm image (the lowest resolution among the four bands). Convolution kernels from Aniano et al. (2011) are utilized in this process.

Next, to determine the column density and dust temperature from far-infrared images, we perform a pixel-by-pixel fitting by modeling the specific intensity, I_ν, of the modified blackbody function, which is given by

$$I_\nu - I_{bg,\nu} = B_\nu(T_d)\left(1 - e^{-\tau_\nu}\right), \tag{4.5}$$

where $I_{bg,\nu}$ is the specific background intensity at the frequency ν (estimated following a method called 'sigma clipping,' see Sect. 4.5 for details), $B_\nu(T_d)$ is the Planck's function at the dust temperature T_d, and τ_ν is the optical depth at the frequency ν, which is given as

[4]HIPE is a collaborative creation of the *Herschel* Science Ground Segment Consortium, which includes ESA, the NASA *Herschel* Science Center, and the HIFI, PACS, and SPIRE consortia.

$$\tau_\nu = \frac{\mu\, m_{\rm H}\, \kappa_\nu\, N({\rm H_2})}{\eta}. \tag{4.6}$$

Here, the gas-to-dust ratio in the ISM, denoted by η, is approximately 100. The mean molecular weight μ is set to 2.86, assuming that the cold molecular gas comprises 70% molecular hydrogen by mass (Ward-Thompson et al., 2010). The dust opacity κ_ν is related to the frequency ν as

$$\kappa_\nu = \kappa_0 \left(\frac{\nu}{\nu_0}\right)^\beta, \tag{4.7}$$

In this equation, β is the dust emissivity index, assumed to be 2, following Russeil et al. (2013), and $\kappa_0 = 5.04$ cm^2 g^{-1} at 500 μm for an MRN distribution of grain sizes in a diffuse ISM with a gas density of 10^6 cm^{-3} and thin ice mantles (Ossenkopf & Henning, 1994). The dust temperature T_d and column density $N({\rm H_2})$ are treated as free parameters and are estimated by fitting the far-infrared data points using the non-linear least squares Marquardt-Levenberg algorithm.

The resulting column density and dust temperature maps provide important insights into the star formation activities occurring in the regions being studied. The column density maps allow us to trace the distribution of the cold dust, helping to identify dense molecular clumps that could be sites of star formation, while variations in dust temperature can reveal heating sources, thus offering a comprehensive view of the evolutionary stages and processes within these star-forming regions.

4.4 Procedure for eliminating the point sources from the GLIMPSE and MIPSGAL images

As explained in chapter 3, H II regions give rise to significant emission at mid-infrared wavelengths due to the reprocessing of UV photons emitted by the massive stars by dust. The spectral energy distribution of dust from MIR to FIR wavelengths can be computed by estimating the flux density of extended emission in GLIMPSE, MIPSGAL, and Hi-GAL surveys. However, the analysis of warm dust emission using the GLIMPSE and MIPSGAL images is severely affected by the presence of numerous point sources. Thus, one needs to remove the point source contaminants first in order to estimate the flux density from extended emission. To carry out this task, we have used the MOsaicker and Point source EXtractor (MOPEX; Makovoz & Marleau 2005) software. The steps that we have taken

are described in brief below.

4.4.1 Analysis of the GLIMPSE/IRAC data

1. The IRAC data contains artifacts of various types, including "Stray light", "Muxstripe", "Muxbleed", "Column Pulldown", and "Jailbars". However, artifact-mitigated images (*cbcd.fits) have been made available in the archive[5]. These images have been processed to correct for artifacts such as "Column Pulldown" and "Banding," which are effects induced by the presence of bright sources in the observations. These corrections improve the quality of the data, making it more reliable for scientific analysis.

2. We then make a list of the corrected basic calibrated data (CBCD; *cbcd.fits), uncertainty (*bunc.fits), and bad pixel mask (*bimsk.fits) images into three separate .txt files. The following steps will be computing the overlap correction, mosaicing the data, and finally, performing point source extraction.

3. Initially, it is necessary to match the backgrounds of overlapping IRAC frames. The "Overlap" pipeline in MOPEX handles this by computing an additive correction for each CBCD image, ensuring they are adjusted to a consistent background level. Also, we must load a "Pmask" (permanent bad pixel mask) file in the "Overlap" pipeline. These "Pmask" files are date-specific and are supplied along with the MOPEX installation. We have to set a specific "Pmask" file, which is closest in time to the observation date.

4. With the CBCDs now corrected for mismatched backgrounds, the subsequent step is to utilize these corrected CBCDs to generate a new mosaic using the "Mosaic" pipeline. Most of the parameters for this pipeline are kept at their default values, whereas the "Array Location Dependent Photometric Correction Mosaic" parameter is set to "Spitzer Cryo Default" to apply photometric corrections to the generated mosaic. This correction is required as the IRAC flatfield is determined by observing the high surface brightness zodiacal background, which has a spectral peak redward of the IRAC filters. However, the spectral energy distributions of many sources, especially stars, have color temperatures peaking blueward of the IRAC filters.

5. Next, we use the "Apex" pipeline to perform the point source photometry. This

[5] `https://sha.ipac.caltech.edu/applications/Spitzer/SHA/`

requires the point response function (PRF) to be supplied to the pipeline. Following the recommendations given in the *Spitzer* data analysis cookbook[6], we have used a list of PRFs, as this significantly enhances the quality of PRF fitting for sources that are located outside the central regions of the arrays.

6. Finally, the "APEX QA" pipeline is used to assess the quality of PRF fitting. This pipeline can also subtract the fitted point sources from the original mosaic and generate a residual mosaic. The residual mosaic now has all the point sources removed and is used for subsequent analysis.

4.4.2 Analysis of the MIPSGAL/MIPS data

1. We start our analysis by examining the level-2 post-basic calibrated data (PBCD) images/mosaics for artifacts. As the CBCD files for MIPS are not available from the archive, we must self-calibrate the level-1 BCD images to remove the artifacts.

2. In this self-calibration process, we first generate a frame that contains only the artifacts. This frame can then be used to correct each BCD image by dividing out the artifacts. These steps can be accomplished using the "flatfield.pl" Perl script that is provided with the MOPEX software package. In the end, "flatfield.pl" returns a "flat" image, which contains only artifacts and self-calibrated BCDs, which can be used further to make a new mosaic.

3. Next, we create a new mosaic using the "mopex.pl" script that comes packaged with MOPEX. Once this script is executed, a directory with the new PBCD mosaic is created.

4. Now that we have generated a new mosaic, we extract the point sources by using the "Apex" pipeline and providing a PRF map. "Apex" fits the PRF and writes the point source information in an extraction table. Finally, we create the point source subtracted residual map by using the "Apex QA" pipeline and extraction table.

4.5 Modelling the dust SED using the MIR and FIR data

Infrared emission from Galactic H II regions arises primarily from heated dust grains, which re-radiate ultraviolet light from massive stars in the mid to far-infrared, and from

[6] `https://irsa.ipac.caltech.edu/data/SPITZER/docs/dataanalysistools/cookbook/1/`

PAH molecules that emit broad spectral lines in the mid-infrared upon excitation by UV photons. The study of infrared emission by fitting a SED function to the infrared flux densities provides insights into the heating, ionization, dust composition, grain size distribution, and total infrared luminosity, which are crucial for understanding the physical conditions and evolution of H II regions.

In this section, we aim to model a global SED for the full H II region as opposed to Sect. 4.3, where we fit (per-pixel) a modified blackbody function only using the far-infrared data. As indicated in Sect. 4.2.4 and 4.2.5, we have used far-infrared data from the Hi-GAL survey and mid-infrared data from the GLIMPSE and MIPSGAL surveys for determining the global dust SED. To estimate the far-infrared flux densities from the Hi-GAL survey, we employed the `Photutils` package (Bradley et al., 2023), which is an affiliated package of the `Astropy` library. The process begins by estimating and subtracting the background emission from each far-infrared map using a method called 'sigma clipping.' In this technique, pixels that fall above or below a specified σ level from the median are removed, and the statistics are recalculated to refine the background estimate. Following this, source detection and extraction are carried out on the background-subtracted maps through image segmentation, where sources are identified based on having a minimum number of connected pixels, each exceeding a 3σ threshold above the background noise. Elliptical apertures are then fitted to these detected sources, allowing for the calculation of total far-infrared flux densities within these apertures for each far-infrared band of the Hi-GAL survey.

To estimate the mid-infrared flux densities, we used the point source subtracted maps from the GLIMPSE and MIPSGAL surveys. We estimated the fluxes (including extended emission) using two approaches. The first approach involved removing point sources from the images using the method described previously and measuring the total flux density of the remaining emission. Alternatively, we performed photometry on the entire region encompassing the H II regions, including both point sources and extended emission. We then calculated the total flux density of the point sources within the aperture using data from the GLIMPSE point source catalog (Benjamin et al., 2003) and subtracted this from the total flux density to estimate the contribution from extended emission alone. Both methods yielded results that were consistent within 3–8%, supporting the validity of our approach. We then combined the mid-infrared flux densities from the GLIMPSE and MIPSGAL surveys with those from the Hi-GAL survey to construct the infrared SED of the H II regions.

Finally, we fit the SED through radiative transfer modeling using the `DustEM` package

(Compiègne et al., 2011)[7]. The `DustEM` tool utilizes the formalism of Desert et al. (1986) to determine the grain temperature distribution, which is then used to compute the dust SED based on the specified dust type and size distributions. Key input parameters include the type of grains, their size distribution, optical properties, thermal capacities, and other related characteristics. In this study, we employed a dust model from Compiègne et al. (2011) that incorporates PAHs, amorphous carbons, and amorphous silicates. We adhered to the same grain size distribution and physical properties as detailed in the appendix of Compiègne et al. 2011.

4.6 Identifying the candidate ionizing stars using the NIR data

High-mass stars form in clusters that also include a large population of low-mass stars and YSOs. These clusters are young and deeply embedded in their parent GMCs, with massive stars typically forming at the center. Their deep embedding within the GMCs also makes these clusters highly obscured by the interstellar dust. Hence, studies that are aimed to identify the candidate massive (or ionizing) stars within H II regions are highly affected by interstellar extinction. It plays a major role in determining the observed colors and magnitudes of stars. The interstellar extinction is typically described by the following empirical relationship

$$A_\lambda = A_V \left(\frac{\lambda}{\lambda_V}\right)^{-\alpha}, \tag{4.8}$$

where A_λ is the extinction at a given wavelength λ, A_V is the extinction in the visual band, λ_V is the wavelength corresponding to the visual band, and α is the power-law index that depends on the properties of dust, and it may vary in different regions due to the grain size distribution and the local environment.

However, at the NIR wavelengths, the extinction is usually less severe than that in the optical wavelengths, but it is still significant, particularly in dense star-forming regions. Following Rieke & Lebofsky (1985), the extinction law in the NIR regime can often be approximated by A_J/A_V = 0.282; A_H/A_V = 0.175; and A_K/A_V = 0.112. These relations can be used to correct for interstellar reddening in NIR photometric data. By applying these extinction corrections, the intrinsic properties, such as colors and magnitudes, of

[7] `https://www.ias.u-psud.fr/DUSTEM/`

stars can be recovered, facilitating the identification of the candidate massive stars that are responsible for ionizing the surrounding gas.

Hence, we have used NIR data from space and ground-based surveys such as 2MASS and UKIDSS for identifying the candidate massive stars that have ionized their surroundings, creating our target H II regions. For this purpose, we have searched for the NIR point sources in the *2MASS All-Sky Point Source Catalog* and *UKIDSS GPS sixth archival data release* catalogs using circles of radius $2' - 4'$ centered at the respective coordinates reported in the THOR radio catalog.

Next, the color-magnitude diagrams (CMD; K vs. H−K) were created using the Bessell & Brett homogenized system (Carpenter, 2001) equivalent colors of point sources that fall within the corresponding circular regions. In these diagrams, massive OB-type stars, which are the primary ionizing sources, tend to lie in the upper-left part of the CMD. Reddening shifts their observed magnitudes and colors diagonally toward the lower-right, meaning the slope of this shift provides an estimate of the interstellar reddening in the observed region. Thus, we shortlisted only those sources that lie above the reddening vector (as defined following the interstellar extinction laws provided by Rieke & Lebofsky 1985) of B3-type stars as the candidate ionizing stars. We have chosen B3-type stars as the lower limit of massive stars because ionizing photons produced by stars with spectral types later than B3 are not significant enough compared to the other early-type stars.

However, the primary assumption in this technique (only using CMD for the identification) is that all NIR point sources are located at the same distances as their corresponding H II regions. Hence, this approach may introduce false positives, as any foreground late-type stars that are not intrinsically bright may get misclassified as candidate ionizing stars due to being located at nearer distances than our targets. These false detections can be filtered out by constructing color-color diagrams (CCD) and selecting only those sources whose colors align with those of OB-type stars in the CCDs.

Thus, we then plotted the shortlisted (from the CMD) candidate ionizing stars on the respective color-color diagrams (H−K vs. J−H). The ionizing stars are expected to appear in specific regions of the CCD depending on their intrinsic colors and the amount of reddening they experience. Hence, to pinpoint potential ionizing stars linked to the H II regions, we included only those sources situated between the reddening vectors of OB-type stars (O9 and B3 star reddening vectors in the CCD). Sources with error bars that cross into this region of interest were also included. As mentioned earlier, to plot these reddening vectors, we used the interstellar reddening law from Rieke & Lebofsky (1985), and crosses at intervals of A_V = 5 are also placed on them to get an estimate of interstellar extinction at

the visible wavelengths. The intrinsic color loci of main sequence and giant stars ($[J-H]_0$ and $[H-K]_0$) were determined based on the criteria provided by Cox (2000) and Bessell & Brett (1988).

To further check the consistency in our analysis, we estimated the hydrogen column densities ($N(H_2)$) at the coordinates of the candidate ionizing stars from the visual extinction (A_V) measured in the CMD/CCDs by utilizing the following equation (Bohlin et al., 1978):

$$N(H_2) = \frac{A_V}{5.3 \times 10^{-22}}\ \mathrm{cm}^{-2}. \tag{4.9}$$

If we find that there is a broad consistency between the column densities measured from the far-infrared maps (see Sect. 4.3) and that estimated using the visual extinction (eq. 4.9) from the CMD/CCD, then we accept the source as a candidate ionizing star. However, one caveat in this method is that the dust opacity and $N(H_2)$ to A_V ratio vary from region to region (Predehl & Schmitt, 1995; Güver & Özel, 2009).

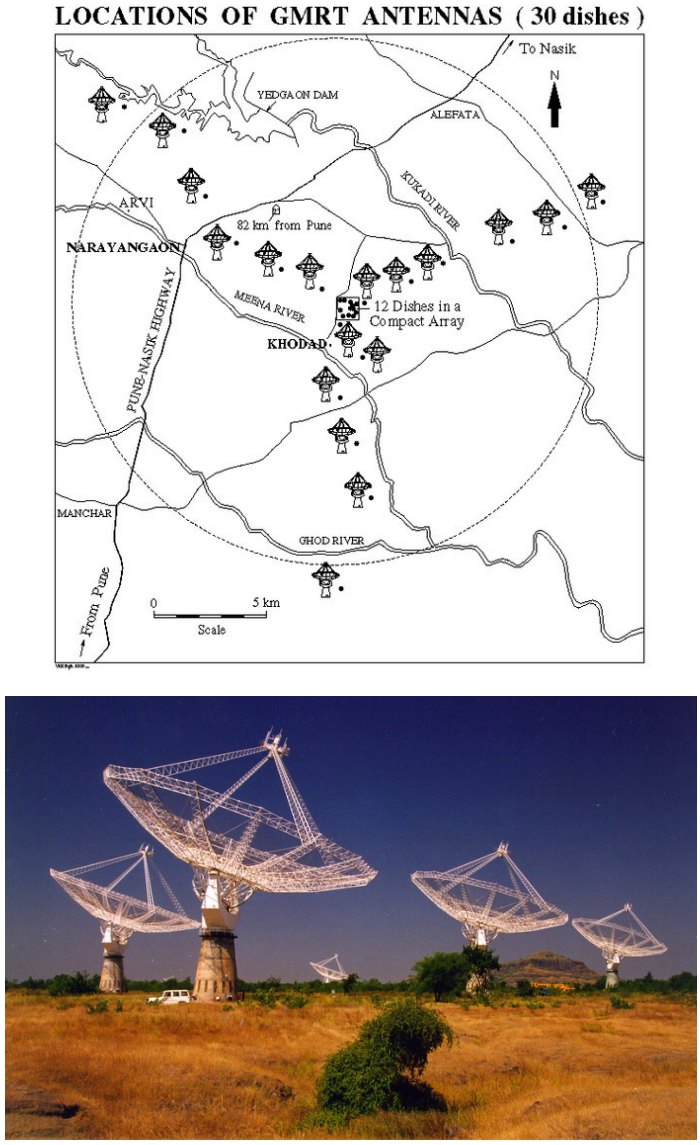

Figure 4.1: Images showing the (top) array configuration of uGMRT and (bottom) a close-up view of a few parabolic dish antennas. Images are taken from `https://www.gmrt.ncra.tifr.res.in/`

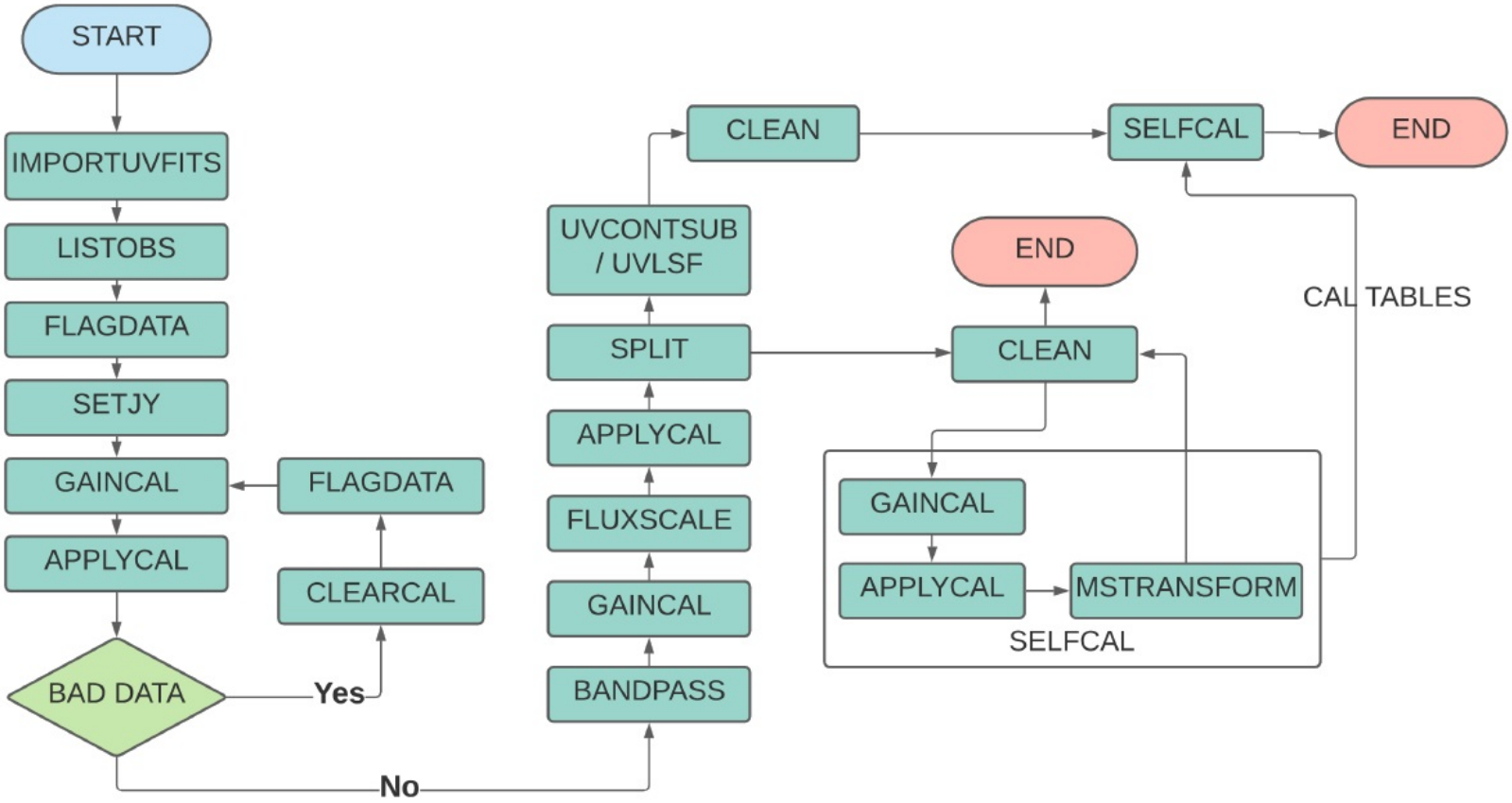

Figure 4.2: Images showing the flowchart describing the data editing, calibration, and imaging procedures.

Chapter 5

Gas dynamics in the star-forming region G18.148–0.283: Is it a manifestation of two colliding molecular clouds?

5.1 Introduction[1]

Understanding the formation processes of massive stars ($M \geq 8$ $M_{\odot}$) or star clusters is still far from complete. Observational studies targeting massive star formation are more challenging compared to their low-mass counterparts due to massive stars forming on short time scales and in clustered environments (Kratter & Matzner, 2006). Since the massive star-forming regions are, on average, more distant compared to the areas forming low-mass stars, there are additional limitations of angular resolution and sensitivity of observing facilities (Kurtz et al., 1994; Churchwell, 2002). Despite these difficulties, studies of massive star formation are crucial, as they continuously influence the evolution of galaxies by emitting protostellar jets, ejecting stellar materials, accreting gas, and various other mechanisms.

Although the formation of low or intermediate-mass stars by accretion of matter is reasonably well understood, one cannot simply scale up this process to form massive stars. The significant number of companions around high-mass stars influence the subsequent accretion onto the massive protostellar cores (Krumholz et al., 2009). The outward radiation pressure can also halt the accretion process before the core reaches its final mass. Thus,

[1]This chapter is based on the published paper: Dey et al. (2022) [Jyotirmoy Dey, Jagadheep D. Pandian, and Dharam Vir Lal, "Gas Dynamics in the star-forming Region G18.148–0.283: Is It a Manifestation of Two Colliding Molecular Clouds?", 2022, The Astrophysical Journal, 925, 60]. The paper is reproduced here with minor changes.

the massive core needs to accrete mass with a high accretion rate (10^{-4}–10^{-3} $M_{\odot}$ yr^{-1}; Wolfire & Cassinelli 1987; McKee & Tan 2003) to overcome the radiation pressure.

McKee & Tan (2003) explained that such an accretion rate is possible if the surface density of the clumps (Σ) is sufficiently high with a value $\gtrsim$ 1 g cm^{-2}. One of the ways to create a region with such high values of Σ is a cloud-cloud collision (CCC). In this process, two supersonic clouds collide with one another to create a shocked and compressed region suitable for fragmentation and further collapse. CCCs are not very rare in the Milky Way. Early observations of CCCs include studies of NGC 133, where the CO spectra revealed two velocity components (Loren, 1976, 1977). The first cluster to be identified as a possible collision object was Westerland 2, which harbors two associated clouds with a velocity difference of 20 km s^{-1} (Furukawa et al., 2009; Ohama et al., 2010) approximately. Other recent observations by Fukui et al. (2014), Torii et al. (2015), Baug et al. (2016), Dewangan & Ojha (2017), Dewangan et al. (2019), Issac et al. (2020) have also detected CCCs in the high-mass star-forming regions.

In most cases, the relative velocity between the two colliding clouds leads to two different velocity peaks or components in the resulting molecular spectrum (Loren, 1976, 1977; Dickel et al., 1978). Since the mixing of the colliding clouds continues for a long time after the instance of the collision, a collision front of shocked materials having intermediate velocities also forms in between the colliding clouds. As a result of this event, a "broad-bridge" feature appears in a position-velocity (PV) diagram of the colliding region (Haworth et al., 2015) that connects the velocity peaks detected in the molecular spectrum. Thus, surveys of molecular line emission (especially ^{12}CO) are great tools to identify and verify CCC events. One such survey is the *CO High-Resolution Survey* (COHRS; Dempsey et al. 2013), which maps the ^{12}CO (J=3−2) transition in the Galactic plane between -0.5° $\leq b \leq 0.5^{\circ}$ and $10^{\circ} \leq l \leq 65^{\circ}$ with a velocity resolution of 1 km s^{-1}.

Based on their magnetohydrodynamic simulations, Inoue & Fukui (2013) also concluded that a collision between two supersonic clouds gives rise to the dense filamentary structures enhancing the surface density and self-gravity inside the colliding clouds. Such a filament may achieve the required high surface density, leading to the formation of massive stars. Simulations also show that the collision amplifies the magnetic field in a direction perpendicular to that of the filament. Although the perpendicular alignment of magnetic fields is found to be a general outcome of turbulent magnetohydrodynamic simulations (e.g. Li & Klein 2019 and references therein), detection of such a field geometry using the dust polarization data from the *Planck* telescope[2] can also act as a subsidiary signature of

[2]https://www.cosmos.esa.int/web/planck

a CCC along with other pieces of evidence.

Massive stars also ionize their surrounding environment by producing H II regions. Observations of the H II regions using RRLs can help us determine the ionized gas's kinematics and properties, such as electron temperature. Moreover, in the event of a CCC, one may observe two velocity components in the RRL emission if massive stars form from both clouds around the collision interface.

In this chapter, we perform a multi-wavelength study of a H II region, G18.148−0.283 (G18.15 henceforth), to understand its gas dynamics and formation. Located at a heliocentric distance of 4.1 kpc (Quireza et al., 2006), G18.15 has a physical diameter of 4.9 pc, which corresponds to an angular diameter of $4.1'$ for the given distance. G18.15 is located in the first Galactic quadrant ($l = 18.148°$, $b = -0.283°$; $\alpha = 18^{\rm h}25^{\rm m}01.01^{\rm s}$, $\delta = -13°15'33.5''$). The *Co-Ordinated Radio 'N' Infrared Survey for High-mass star formation* (CORNISH; Hoare et al. 2012; Purcell et al. 2013) reported a flux density of 856.18 ± 82.85 mJy at 5 GHz, and classified G18.15 as an UCHR. Quireza et al. (2006) used the National Radio Astronomy Observatory (NRAO) 140-ft (43 m) telescope in Green Bank at 8.6 GHz (HPBW = $3.20'$) to estimate an electron temperature ($T_{\rm e}$) of 7180 ± 70 K for the entire region assuming G18.15 to be a homogeneous, isothermal sphere. Lockman (1989) measured the local standard of rest (LSR) velocity of G18.15 using the same 140-ft telescope, and reported $V_{\rm LSR} = 53.9 \pm 0.4$ km s^{-1}. Kurtz et al. (1994) estimated the lower limit of the Lyman-continuum photon rate in the region based on which they assigned a spectral type of B0.5 to the central ionizing star.

In their multi-wavelength-based observation, Zhang et al. (2017) concluded that there are three clump candidates associated with G18.15, and high-mass star formation processes may still be happening within these clumps. According to them, the formation process was triggered by the forward-propagating shock wave, which originated from the expansion of G18.15 itself. In this chapter, we present evidence that the star formation activity may be the outcome of a CCC.

The structure of this chapter is as follows. In Sect. 5.2, we describe our radio observations with the uGMRT and the ancillary data used for our study. In Sect. 5.3, we describe the results from our study, including radio continuum, RRL emission, distribution of molecular hydrogen, ionizing stars, and young stellar objects (YSO) in this ionized region. Lastly, in Sect. 5.4, we discuss the possibility of a CCC event behind the formation of G18.15.

5.2 Observations and archival data

Our observation of G18.15 is carried out using the *upgraded Giant Metrewave Radio Telescope* (uGMRT; Swarup 1990) situated at Pune, India. The observations are carried out with the GWB correlator configured to have a bandwidth of 100 MHz centered at 1350 MHz with 8192 channels. uGMRT has a native resolution of $2''$ and the largest detectable angular scale of $7'$ in this band. The details of the observational run are furnished in Table 5.1. A total of five hydrogen RRLs, H167α to H171α (see Table 5.2), are present in this frequency range. The radio source 3C48 is used as the flux density calibrator and bandpass calibrator, whereas $1911-201$ is used as the gain calibrator.

Table 5.1: Details of our observation using uGMRT.

Parameter	Value
Target name	G18.148-0.283
Observation date	March 11, 2019
System Temperature	73 K
On-source time	210 minutes
No. of channels	8192
Central frequency	1350 MHz
Bandwidth	100 MHz
Primary Beam	$25'$
Synthesised Beam	$\approx 2''$
Peak continuum flux density	373.3 mJy beam^{-1}
Theoretical rms (σ)[a]	0.4 mJy beam^{-1}

Note – a = in a single channel at 10 km s^{-1} resolution before stacking.

The radio data are reduced using the NRAO *Common Astronomy Software Applications* (CASA; McMullin et al. 2007) package. For the details on the radio data reduction, please refer to Sect. 4.1.2.

After carefully flagging and calibrating the target, the net bandwidth available for imaging G18.15 is around 50 MHz, considering only the line-free channels. The target is then imaged using the `tclean` task, and the continuum image is self-calibrated to improve the dynamic range. The final 1σ noise in the continuum image is 0.06 mJy beam^{-1}.

As shown in Table 5.1, the observations are carried out with 8192 channels, providing a native velocity resolution ~ 2.6 km s^{-1}. The gain-calibrated line data are first Hanning-smoothed to a velocity resolution $\sim$ 5 km s^{-1} in order to get rid of the Gibbs ringing phenomenon caused by the strong RFI sources. However, only the H169α and H170α

Table 5.2: Name and rest frequencies of the RRLs that were targeted in our observation.

RRL name	Rest frequency (ν_0) (MHz)
H167α	1399.368
H168α	1374.601
H169α	1350.414
H170α	1326.792
H171α	1303.718

line data could be imaged using the task `clean`. The H167α and H171α could not be imaged due to the lines being affected by the edges of the bandpass. The H168α line was discarded due to it having a poor signal-to-noise ratio. To enhance the signal-to-noise ratio, the images of both RRLs were stacked to the observed frequency of H169α using the package `Line-Stacker` (Jolly et al., 2020)[3]. This results in an improvement in the signal-to-noise ratio of the line image by roughly a factor of $\sqrt{2}$. The final rms noise (= σ) after stacking is equal to 0.25 mJy beam^{-1}.

The uGMRT observations are complemented by different multi-wavelength archival datasets (see Sect. 4.2 for details), including data from the 2MASS, UKIDSS, GLIMPSE, Hi-GAL, COHRS, and THOR surveys to a name a few.

5.3 Results

5.3.1 Radio emission from the ionized gas

5.3.1.1 Continuum emission

Fig. 5.1 shows the 1350 MHz radio continuum emission from G18.15 at 10″ resolution using the uGMRT, with the THOR map at 25″ resolution being overlaid in contours. Although the native resolution of uGMRT is 2″, we have restricted the resolution to 10″ to recover the extended emission. The morphology of radio continuum emission is elongated along the NW-SE direction with an extended envelope of emission along the perpendicular direction of the central elongated structure. At 25″ resolution, there are two peaks in the radio continuum, which are resolved into multiple peaks at the higher resolution of uGMRT. The spectral index for the region is obtained from the THOR survey and is seen to be ≈ 0.1. This suggests that the emission is thermal and has an optical depth around unity since one

[3] `https://github.com/jbjolly/LineStacker/releases`

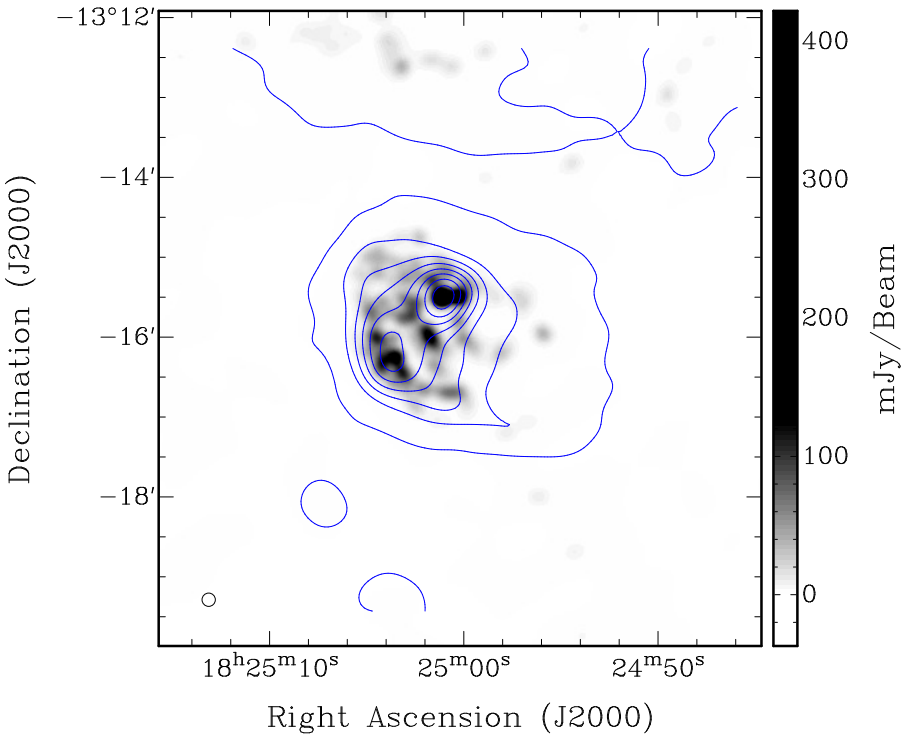

Figure 5.1: The radio continuum image of G18.15 at 1350 MHz is shown overlaid with the contour levels (in blue) from THOR at 1310 MHz. The color scale depicts the specific intensity or brightness in mJy beam^{-1}. The levels are starting from 3σ and increasing in steps of 75 mJy beam^{-1}, while the rms noise is equal to $\sim$ 1.4 mJy beam^{-1}. The 1350-MHz beam size is shown at the bottom-left corner of the figure using a black empty circle.

expects the spectral index to be close to 0 as the emission transitions from being optically thick to optically thin.

Although the assumption of the radio continuum emission being optically thin is not strictly valid, we can derive a lower limit for the Lyman-continuum photon rate (N_{Ly}) using the following equation (Schmiedeke et al., 2016):

$$N_{Ly} \geq 4.76 \times 10^{42}\, \nu^{0.1}\, d^2\, S_\nu\, {T_e}^{-0.45}, \tag{5.1}$$

where S_ν is the flux density in Jansky (Jy), ν is the frequency in GHz, d is the distance to the source in parsec (pc), and T_e is the electron temperature of the ionized gas. Adopting an electron temperature of 7180 K (Quireza et al., 2006) and a distance of 4.1 kpc, one obtains the Lyman-continuum photon rate to be larger than 5.8×10^{48} s^{-1} (log $N_{Ly} = 48.76$). If all the ionizing radiation were to arise from a single star, this would require a main sequence star of spectral type O6.5-O7 or earlier (Martins et al., 2005).

Our estimate of the Lyman-continuum photon rate is in good agreement with that of Zhang et al. (2017), who found log $N_{Ly} = 48.68$ using the radio continuum data from the 1.4 GHz *NRAO VLA Sky Survey* (NVSS; Condon et al. 1998), but is significantly higher than that of Kurtz et al. (1994), who found log $N_{Ly} = 46.82$ using observations of the region at 8.4 GHz with the VLA in the B-configuration. Our higher Lyman-continuum photon rate than that of Kurtz et al. (1994) is probably due to the extended emission being resolved out in their high-resolution study. Similarly, the Lyman-continuum photon rate estimated from the high-resolution ($\sim 2''$) CORNISH survey is log $N_{Ly} = 48.0$, which suggests that some extended emission is resolved out in the CORNISH maps as well.

5.3.1.2 RRL emission

Fig. 5.2 and 5.3 show the channel map and integrated intensity map of the RRL emission at an angular resolution of $25''$. It can be seen from the figures that three different emission peaks are aligned with the central elongation of continuum emission. The SE peak is the brightest among the three peaks, followed by the middle and NW peaks. The SE peak is located within $2''$ of the continuum SE peak, while the middle and NW peaks are located at opposite sides of the continuum NW peak. As mentioned in Sect. 5.3.1.1, the radio continuum spectral index for this region is positive and close to 0, suggesting the emission transition from being optically thick to optically thin, whereas the RRL emission is optically thin. This could be one of the plausible reasons behind the observed misalignment between the radio continuum and recombination line peaks. However, additional studies are required to address this problem.

5.3.1.3 Electron temperature map

Fig. 5.4 shows the electron temperature (T_e) distribution across G18.15 using the RRL and continuum data (the methodology and relevant equations are given in Appendix A). This was done by smoothing the radio continuum map to the same resolution as that of the RRL map – $25''$ for the uGMRT data. The electron temperature at the peaks of continuum emission ranges from 5200–9500 K. The electron temperature agrees well with the average electron temperature of 7180 K (Quireza et al., 2006) towards the region, considering that this was measured at a much coarser resolution of $3.2'$. It is, however, surprising to see that the electron temperature is much lower at the locations of diffuse emission.

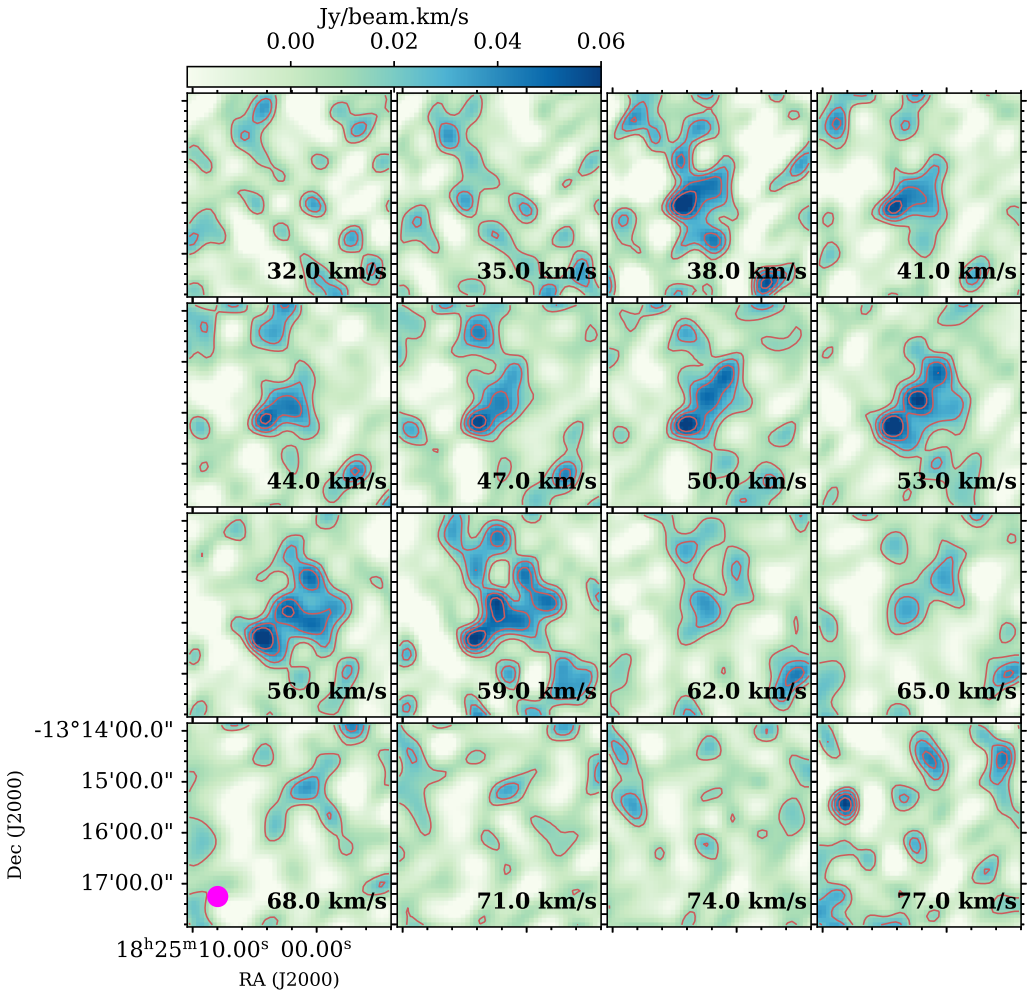

Figure 5.2: The stacked RRL channel map towards G18.15 is shown here. Each panel shows the velocity integrated intensity within a velocity range of 3 km s^{-1}. The 25″ beam is shown using a filled magenta circle.

5.3.2 Kinematics of the region

Fig. 5.5 shows the velocity field of the ionized gas in the region. The NW continuum peak is observed to have a higher velocity compared to the SE peak. The velocity field (52–65 km s^{-1}) between the NW and SE peaks appears to be smooth with a linear gradient at 40″ resolution of THOR, while at 25″ resolution, it appears somewhat discontinuous. The presence of two velocity components to the RRL emission separated by 13 km s^{-1} with a discontinuity in the middle of the H II region is suggestive of G18.15 being a case of a CCC.

The possibility of G18.15 being a case of a CCC can be tested by examining the kine-

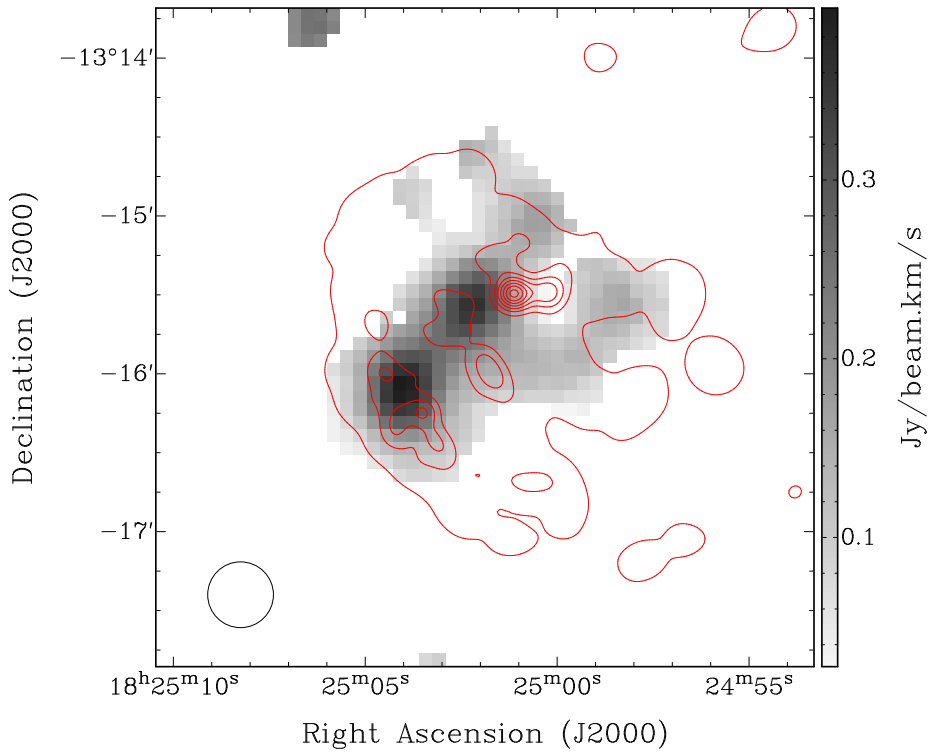

Figure 5.3: The moment-0 map from the uGMRT RRL data is shown overlaid with the respective radio contours in red from the continuum emission. The contours are increasing in steps of 50 $\mathrm{mJy\,beam^{-1}}$ starting from the 3σ level. The restoring beam is shown in a black empty circle at the bottom-left corner of the figure.

matics of the molecular gas in the region. We used the COHRS data for this purpose since the J=3−2 transition of CO is an excellent tracer of the warm gas (10−50 K) at densities around 10^4 cm^{-3}. The CO spectrum towards G18.15 (Fig. 5.6) shows the presence of two velocity components (or peaks) at 53.4 km s^{-1} and 66.7 km s^{-1} respectively. It can be seen that the velocity components in CO are close to those observed in the ionized gas. This suggests that the massive stars in the region have formed from the two molecular clouds traced by the CO emission. The spectrum also shows that the velocity components representing two different molecular clouds are connected by a narrow plateau of intermediate velocity and moderate intensity, which may arise from the interaction between the two clouds.

Fig. 5.7 shows the CO integrated intensity map using the velocity range of 39−55 km s^{-1} covering the low-velocity molecular cloud overlaid with the black contours from the integrated intensity map using the 59−74 km s^{-1} velocity range of the high-velocity molecular clouds. The radio continuum emission at 1350 MHz is also overlaid with the blue contours. Fig. 5.7 shows that both clouds are obliquely shaped with a NE-SW elongation.

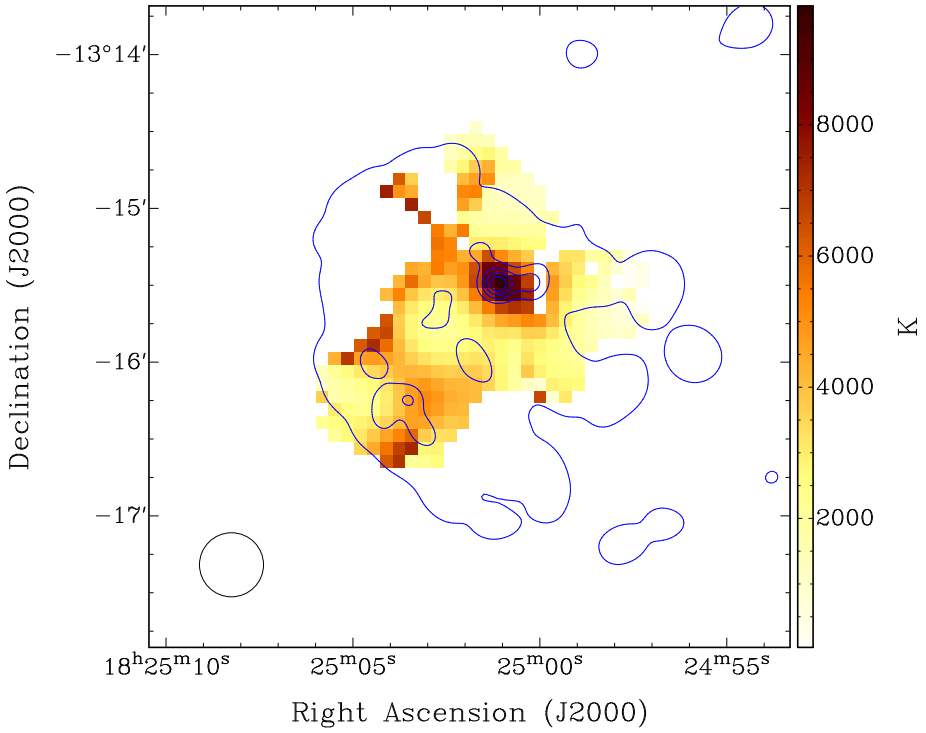

Figure 5.4: The pixel-wise electron temperature (T_e) map from uGMRT is shown overlaid with the 3σ contours (in blue) from the radio continuum emission. The contour levels are increasing in steps of 75 mJy beam^{-1} starting from the 3σ level. The beam is shown in a black empty circle at the bottom-left corner of the figure.

The figure also shows the presence of a cavity (diameter $\sim$ 0.5 pc) towards the west of the radio continuum peaks, with most of the CO line emission occurring from a C-shaped region that is offset to the east of G18.15 from the center.

The presence of two velocity components connected with an intermediate-velocity emission profile in the CO spectrum, a large cavity, a linear gradient, and a C-shaped emission region suggest that G18.15 is the site of a CCC event between two molecular clouds with a relative velocity of 10 km s^{-1}. The features observed are in agreement with the simulations of Habe & Ohta (1992) and Takahira et al. (2018).

In particular, it is interesting to note the presence of a dark filamentary structure connecting the radio continuum peaks in 8.0 μm (Fig. 5.8). Although the filament is not classified as an IRDC in the catalogs of Simon et al. (2006) and Peretto & Fuller (2009), the extinction at 8.0 μm that has close correspondence with 870-μm emission suggests the filament to be an IRDC. This is consistent with the simulations of Inoue & Fukui (2013) wherein dense filaments are formed in CCC events due to enhancement of the gas surface density.

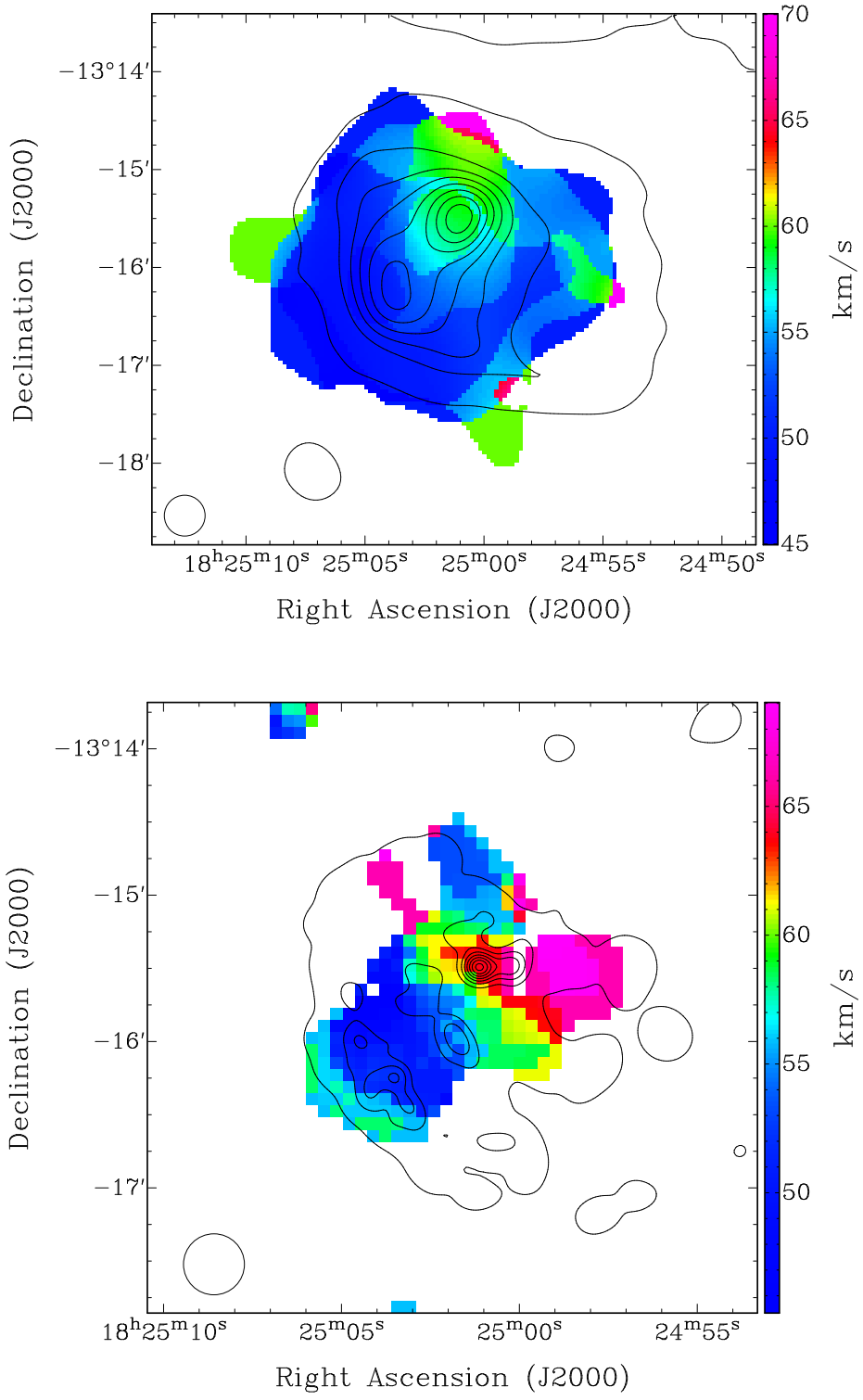

Figure 5.5: The top and bottom panels show the moment-1 maps from the THOR and uGMRT, respectively. A velocity gradient is seen between the NW and SE peaks. The contours in the left and right panels are identical to those in Fig. 5.1 and Fig. 5.3, respectively.

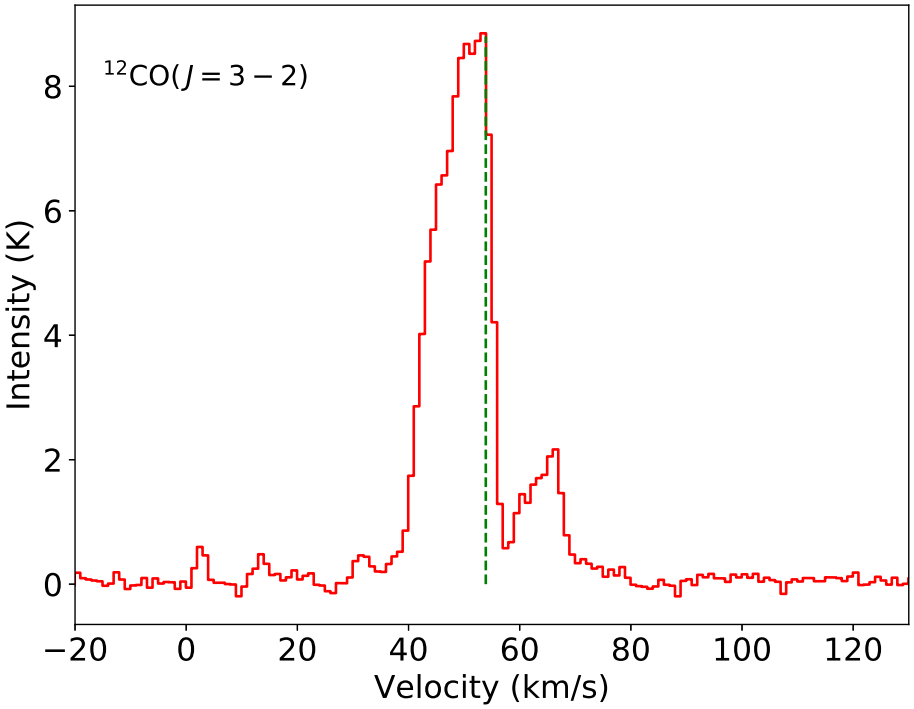

Figure 5.6: The ^{12}CO spectrum towards G18.15 shows two velocity peaks at the LSR velocities of 53.4 and 66.7 km s^{-1} respectively. The intermediate velocities form a narrow plateau connecting those peaks. The LSR velocity measured by Lockman (1989) is shown by the green dashed line.

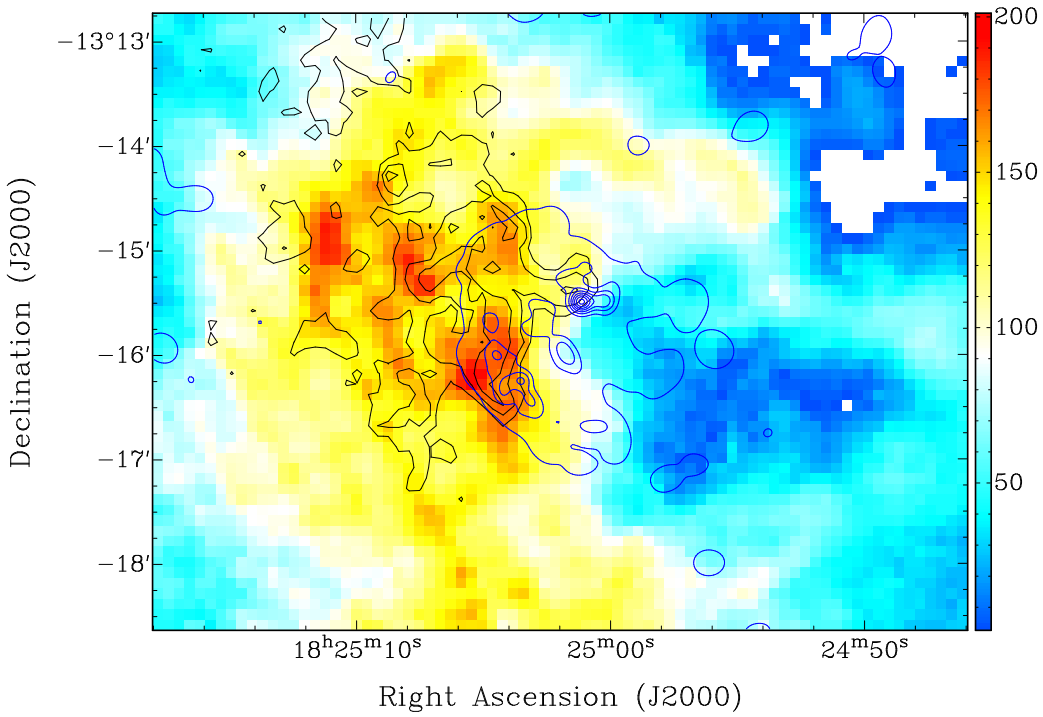

Figure 5.7: The color scale shows the ^{12}CO (J=3−2) integrated intensity $[\mathrm{K\,.\,km\,s^{-1}}]$ within the velocity range 39 to 55 km s^{-1}. The contours in black (from 18 to 40 K.km s^{-1} in steps of 8 K.km s^{-1}) show the CO integrated emission within the velocity 59 to 74 km s^{-1}. The contours in blue show the radio continuum emission from uGMRT at 1350 MHz with the contour levels identical to those in Fig. 5.3.

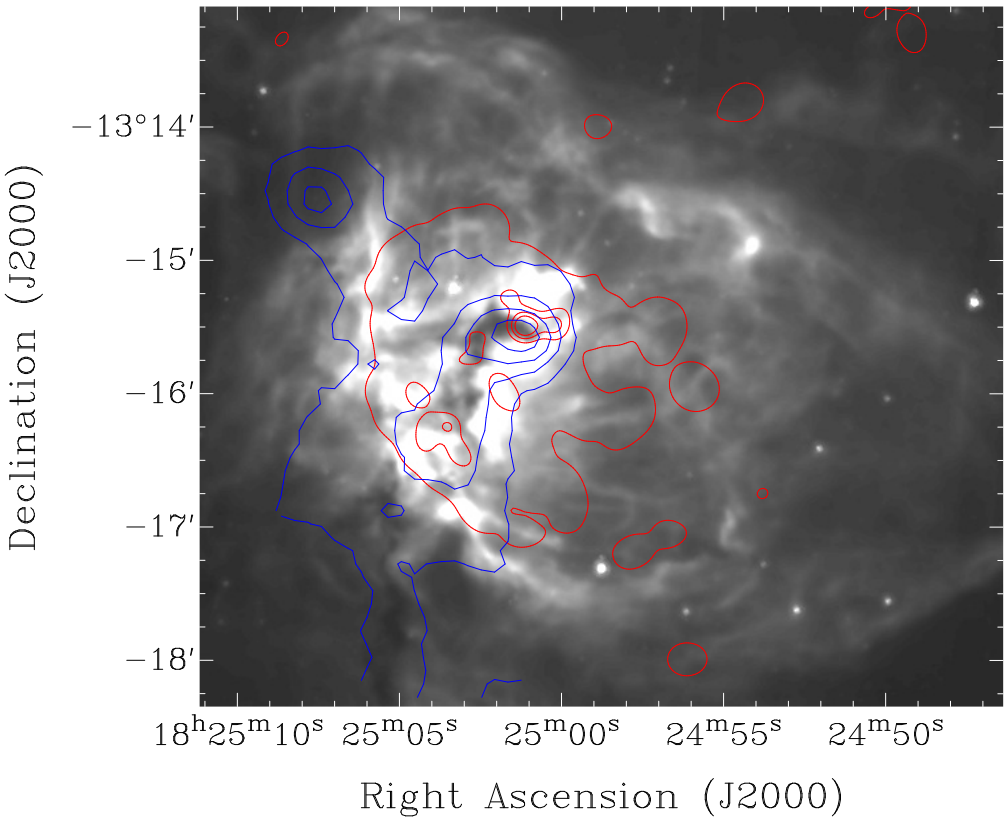

Figure 5.8: The figure shows the 8.0-μm mid-infrared image of G18.15 obtained from the *Spitzer*-GLIMPSE survey. The blue and red contours show the dust emission at 870 μm and radio continuum emission at 1350 MHz, respectively.

5.3.3 FIR emission from the cold dust

The cold dust emission was analyzed using data from the Hi-GAL survey. We used level-2.5 data from the Herschel Science Archive for this purpose. The data have a plate scale of 3.2″ per pixel at the PACS wavelengths of 70 and 160 μm, and 6″, 10″, and 14″ per pixel at the SPIRE wavelengths of 250, 350, and 500 μm, respectively. Moreover, the data have different units, with the PACS data having units of Jy pixel^{-1}, while the SPIRE data has units of MJy sr^{-1}. The data were pre-processed in the HIPE software to have the same units and were regridded to a common plate scale using a premade kernel (Aniano et al., 2011).

We generated the column density and dust temperature maps (top and bottom panels of Fig. 5.9) by following the methods described in Sect. 4.3. High column densities can be observed across the radio continuum peaks tracing the central filament with a peak value of 3.1×10^{22} cm^{-2} located close to the NW continuum peak. The dust temperature also peaks towards the center and remains almost constant overall ($\sim$ 33 K) within the H II region. The relatively high value of dust temperature suggests significant heating from the massive stars inside the H II region.

5.3.4 Orientation of the magnetic field lines

We have utilized the 353-GHz *Planck* dust polarization data to determine the mean orientation of the magnetic field lines in the vicinity of G18.15. Following the IAU convention (i.e., the position angle, $\theta_{GAL} = 0^{\circ}$ points Galactic North but increases towards Galactic East), the θ_{GAL} values are derived using the relation

$$\theta_{GAL} = 0.5 \times \tan^{-1}(-U/Q). \tag{5.2}$$

Adopting the transformation relation of position angles (Corradi et al., 1998), the magnetic field orientation in Equatorial coordinates can be calculated as

$$\theta_B = \theta_{GAL} + \frac{\pi}{2} - \psi, \tag{5.3}$$

where ψ is the transformation relation of the position angles in the Equatorial and Galactic systems at the position of each pixel. It is expressed as

$$\psi = \tan^{-1}\left[\frac{\cos(l - 32.9^{\circ})}{\cos(b)\cot(62.9^{\circ}) - \sin(b)\sin(l - 32.9^{\circ})}\right]. \tag{5.4}$$

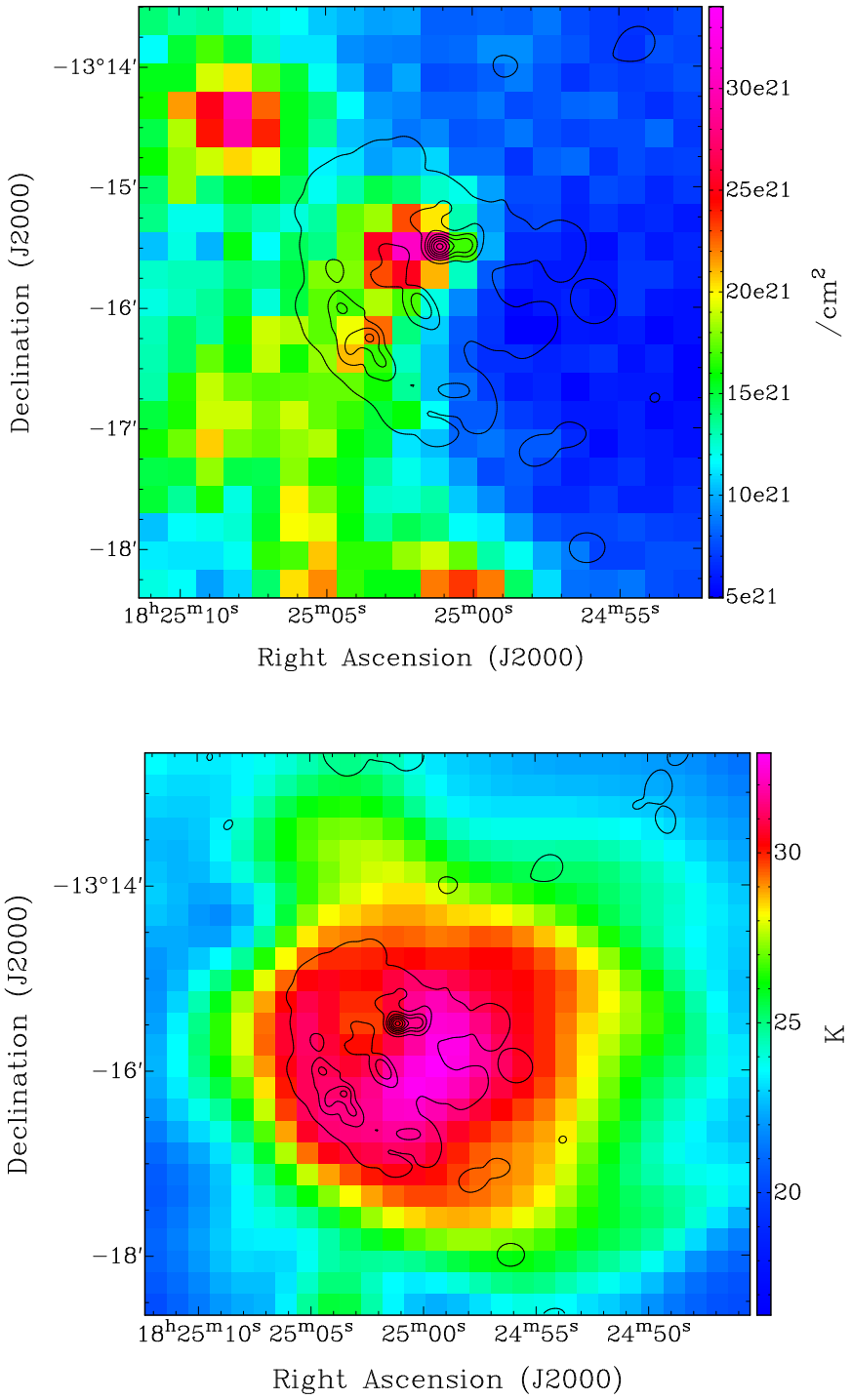

Figure 5.9: The figures show the H_2 column density (top) and dust temperature (bottom) maps towards G18.15. The maps are obtained after fitting pixel-wise SEDs to the PACS and SPIRE far-infrared images. The black contours show the radio continuum emission at 1350 MHz starting at the 3σ level.

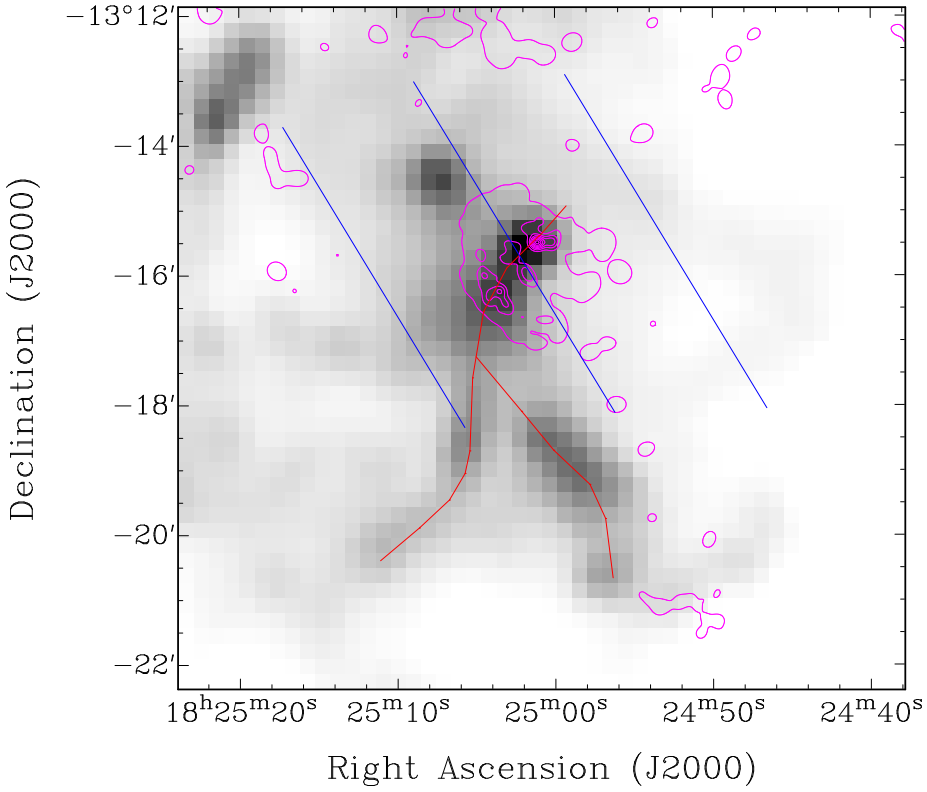

Figure 5.10: The figure shows the 500-μm SPIRE image of the cold dust emission overlaid with the 3σ radio contours at 1350 MHz in magenta. The red solid lines show a visually identified skeleton of the filament, which hosts G18.15. The blue lines are the mean orientation of the magnetic field lines measured around G18.15.

The mean orientation of the magnetic field is estimated to be at a position angle of $30.8^\circ \pm 2.6^\circ$ as shown in Fig. 5.10. It can be seen that the mean magnetic field is nearly perpendicular to the underlying central filament within G18.15.

5.3.5 Identification of the candidate ionizing stars

In order to identify the candidate ionizing stars towards G18.15, we have performed a photometric study of the near-infrared point sources using data from the 2MASS[4] and UKIDSS GPS[5] surveys. We have searched for the near-infrared point sources in the *2MASS All-Sky Catalog of Point Sources* and *UKIDSS GPS sixth archival data release* (UKIDSSDR6plus) catalogs using a circle of 2′ radius centered at $\alpha = 18^{\rm h}25^{\rm m}01^{\rm s}\,, \delta = -13^\circ16'02''$.

Following the methods described in Sect. 4.6, we have identified 2 and 5 candidate ionizing stars from the UKIDSS and 2MASS surveys, respectively (Fig. 5.11 and 5.12). Table 5.3 lists all 7 candidates identified using the near-infrared photometry, and their locations are shown in Fig. 5.13. As an added consistency check, we determined the hydrogen column density ($N(\mathrm{H_2})$) expected at the coordinates of the candidate stars from the visual extinction (A_V) measured in the color-color diagram using Bohlin et al. (1978):

$$N(\mathrm{H_2}) = \frac{A_V}{5.3 \times 10^{-22}}\,\mathrm{cm}^{-2}, \tag{5.5}$$

The respective $N(\mathrm{H_2})$ values from eq. 5.5 and locations of the candidate stars are listed and shown in Table 5.3 and Fig. 5.13, respectively. We find that there is broad consistency between the column density measured from the far-infrared map and that estimated by the visual extinction, with discrepancies attributed to the uncertainty in the dust opacity and other variations in the $N(\mathrm{H_2})$ to A_V ratio (Predehl & Schmitt, 1995; Güver & Özel, 2009).

This gives confidence that the sources listed in Table 5.3 are indeed OB-type stars that are associated with the G18.15 region. However, it is to be noted that only two stars are of spectral type earlier than B0. Fig. 5.13 shows that 2 (2MASS-1 and 2) out of the 7 candidate ionizing sources are located near the continuum peaks of G18.15, whereas 4 out of the remaining 5 sources are located at the periphery of the central dust filament with the last source (UKIDSS-2) at a location slightly away from the region showing radio continuum emission. Thus, while 2MASS-2 is the likely source for the southern continuum peak, the ionizing stars for the northern peak are not detected. However, our analysis does not preclude the existence of a population of ionizing stars in the IRDC that are not detected

[4] http://vizier.u-strasbg.fr/viz-bin/VizieR-3?-source=II/246/out
[5] http://wsa.roe.ac.uk:8080/wsa/region_form.jsp

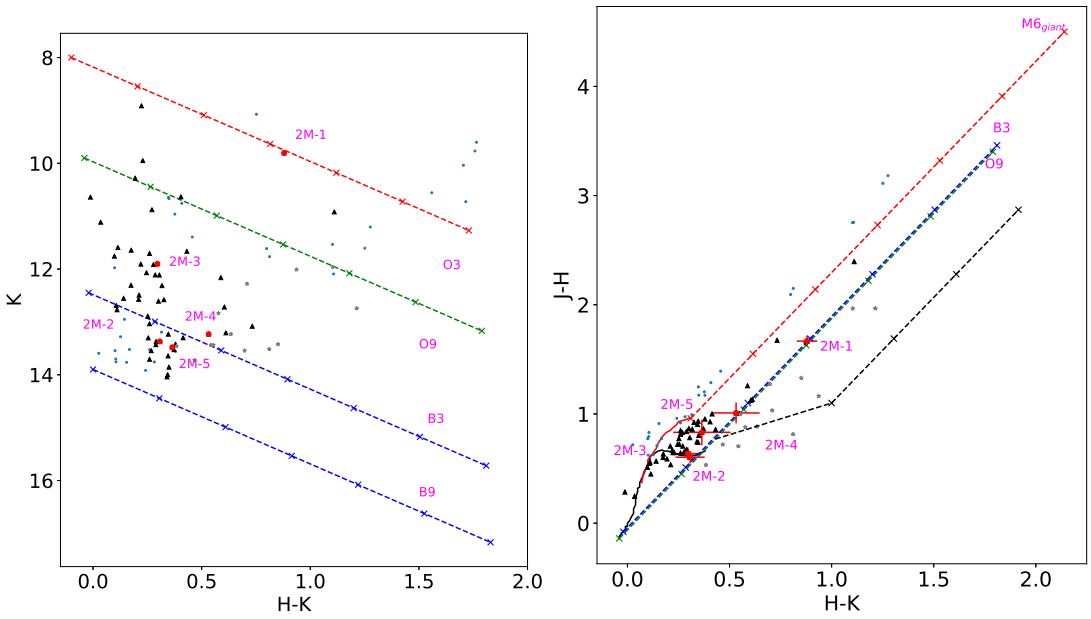

Figure 5.11: The left panel shows the K vs. (H–K) color-magnitude diagram of the 2MASS near-infrared sources within a circle of radius 2′ centered at G18.15. The reddening vectors of the massive stars (O3–B9) are plotted on the color-magnitude diagram. The (J–H) vs. (H–K) color-color diagram of the 2MASS point sources being of spectral type earlier than B9 in the color-magnitude diagram is shown in the right panel. The solid black and red lines represent the loci of Class V (main sequence stars) and Class III (giant stars) objects, respectively (Bessell & Brett, 1988; Cox, 2000). The black long-dashed line represents the locus of the T-Tauri stars (Meyer et al., 1997). Reddening vectors corresponding to the different classes are also shown using dotted lines. The crosses on the reddening vectors are placed at an increasing interval of $A_V = 5$. Sources (main sequence and giants stars) that are located within the reddening vectors of $M6_{giant}$ and O9 spectral classes are represented by black triangles, whereas pre-main sequence sources are denoted by gray stars. Any other objects are denoted by the cyan dots. The candidate ionizing stars are denoted by the red dots with respective error bars.

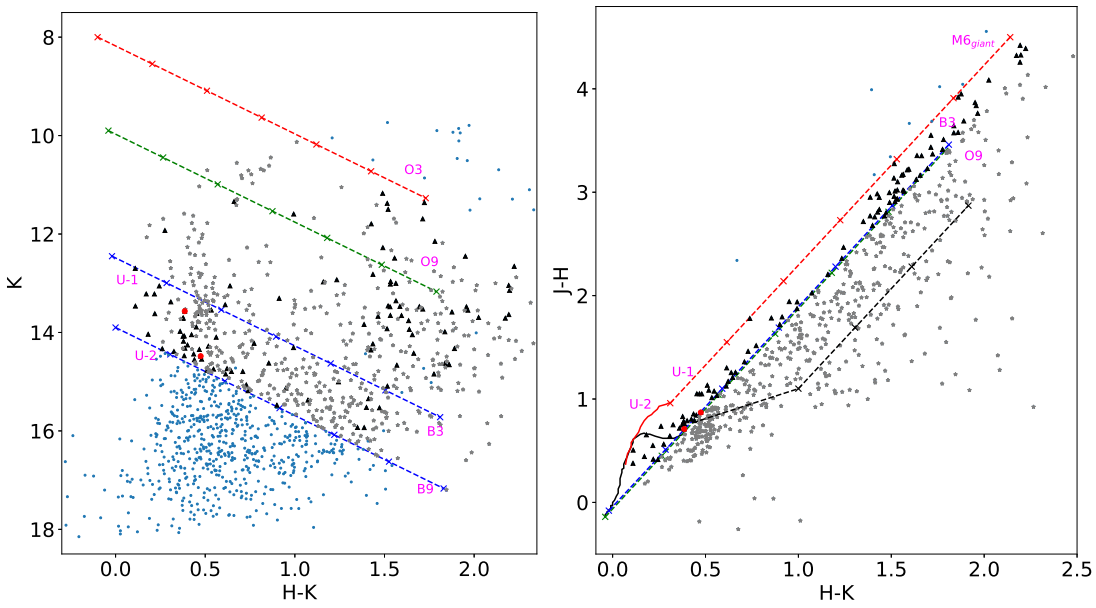

Figure 5.12: Same as Fig. 5.11 but for sources detected in the *UKIDSS Galactic Plane Survey*.

at near-infrared wavelengths on account of significant extinction. This is consistent with the overall ionizing photon flux in the H II region, which is significantly higher than that produced by a single O9 star.

5.3.6 YSOs associated with the G18.15

In order to identify YSO candidates, we have searched the *Spitzer*-GLIMPSE[6] online database within the same region (a circle of 2″ radius centered at $\alpha = 18^{\rm h}25^{\rm m}01^{\rm s}\,, \delta = -13^{\circ}16'02''$) used for searching the candidate ionizing stars and found a total of 369 mid-infrared sources inside it. Due to the nebulosity affecting the IRAC 8.0-μm band, most of the sources are not detected in all four bands of the IRAC camera. Thus, we have adopted IRAC three-band and 2MASS-IRAC five-band classification schemes as described in Gutermuth et al. (2008) to classify the YSOs. These classification schemes are based on the [4.5]–[5.8] color, as it is less contaminated by the dust extinction than the 3.6-μm emission-based colors (Hartmann et al., 2005).

[6]https://irsa.ipac.caltech.edu/data/SPITZER/GLIMPSE/

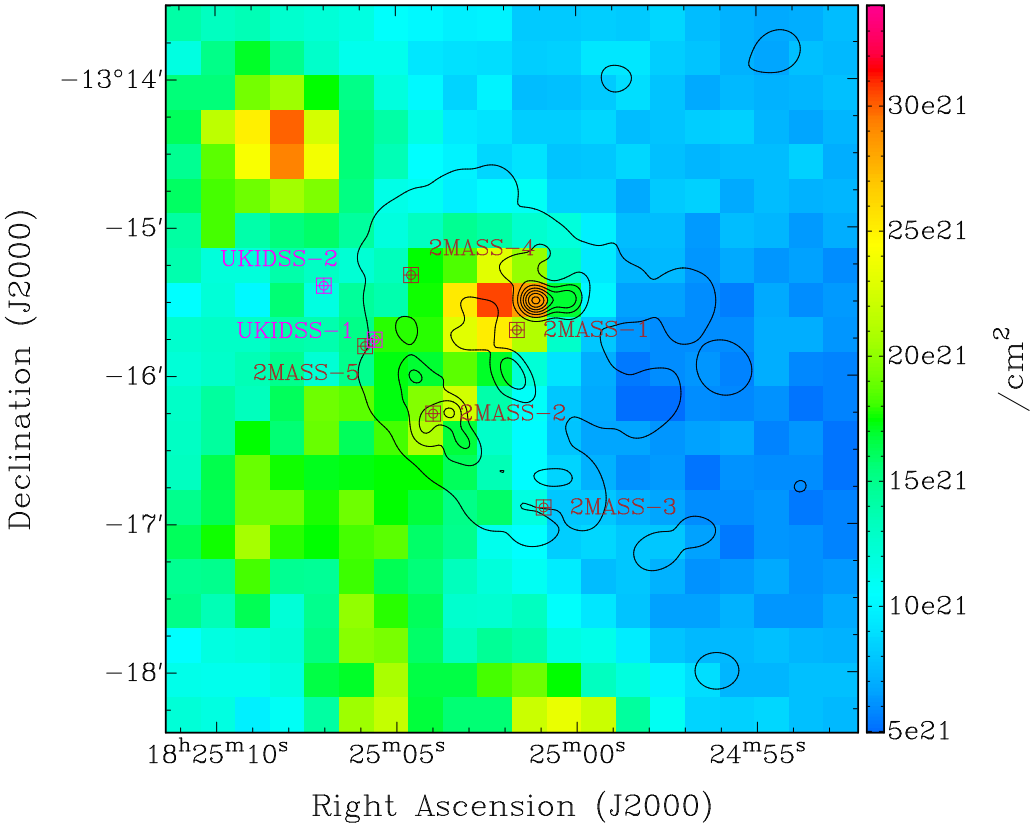

Figure 5.13: Locations of the candidate ionizing stars on the column density map estimated from the studies of cold dust.

Table 5.3: List of candidate ionizing stars detected towards G18.15

Name	Designation	α_{J2000} (deg)	δ_{J2000} (deg)	J (mag)	H (mag)	K (mag)	Spectral type	$N(H_2)^a$ ($\times 10^{22} cm^{-2}$)	$N(H_2)^b$ ($\times 10^{22} cm^{-2}$)
2MASS-1	18250164-1315414	276.257	-13.2615	12.253	10.664	9.76	B2	2.81	2.12
2MASS-2	18250397-1316152	276.267	-13.2709	14.207	13.66	13.326	O9	1.28	1.96
2MASS-3	18250091-1316532	276.254	-13.2815	12.759	12.18	11.857	B3	1.16	1.18
2MASS-4	18250457-1315191	276.269	-13.2553	14.689	13.745	13.187	B3	1.63	1.75
2MASS-5	18250585-1315478	276.274	-13.2633	14.597	13.827	13.436	B2	1.56	1.51
UKIDSS-1	438754351144	276.273	-13.262	15.666	14.885	14.430	O9	1.63	1.66
UKIDSS-2	438754352028	276.279	-13.256	14.523	13.890	13.518	B3	1.27	1.25

Note – a = estimated from eq. 5.5, b = estimated from the respective locations in Fig. 5.13.

Following the IRAC three-band classification scheme, we have detected 18 protostar candidates within G18.15, of which 2 are likely to be highly reddened Class II objects. We have also detected an additional YSO using the 2MASS-GLIMPSE five-band classification scheme. The corresponding CCDs are shown in the top and bottom panels of Fig. 5.14, respectively.

Since UKIDSS is a much deeper survey than 2MASS, we have also searched for YSOs using the NIR and MIR colors of the UKIDSS and GLIMPSE surveys, respectively. We first identified counterparts of the GLIMPSE point sources in the UKIDSS GPS using a 0.5″ matching radius. The UKIDSS colors were then converted to equivalent 2MASS colors following which the five-band classification scheme was used to identify YSOs. A total of 13 Class I or II objects are detected following this method, out of which 11 were undetected in the previous IRAC three-band and 2MASS-IRAC five-band classification schemes. Overall, we have detected 30 YSO using all three classification schemes.

The top and bottom panels of Fig. 5.15 show the de-reddened CCD using the GLIMPSE and UKIDSS surveys and locations of detected YSOs towards G18.15. We find most of the YSOs to be located towards the edges of the H II region, including the IRDC extending beyond the radio emission, with only a couple of YSOs towards the central filamentary structure. As with the case of ionizing stars, a significant fraction of YSOs in the central IRDC is likely to be undetected because of high extinction.

5.4 Discussion

5.4.1 Age of the region

The age of G18.15 can be estimated using the observed properties of the H II region. Under the assumption that the H II region is expanding into a homogeneous medium, the Strömgren radius (R_s) is given by the following expression

$$R_s = \left(\frac{3\, N_{Ly}}{4\, \pi\, n_0^2\, \alpha_B} \right)^{1/3}, \tag{5.6}$$

where α_B is the radiative recombination coefficient assumed to be 2.6 $\times$ 10^{-13} cm^3 s^{-1} (Osterbrock, 1989), and n_0 is the number density of atomic hydrogen, which can be derived from the column density map following $n_0 = 3N(\mathrm{H_2})/2R$. Here, R is the radius of the ionized clump. We can estimate the dynamical age, t_{dyn}, of the H II region based on a simple model of an expanding H II region in a homogeneous medium as (Dyson & Williams,

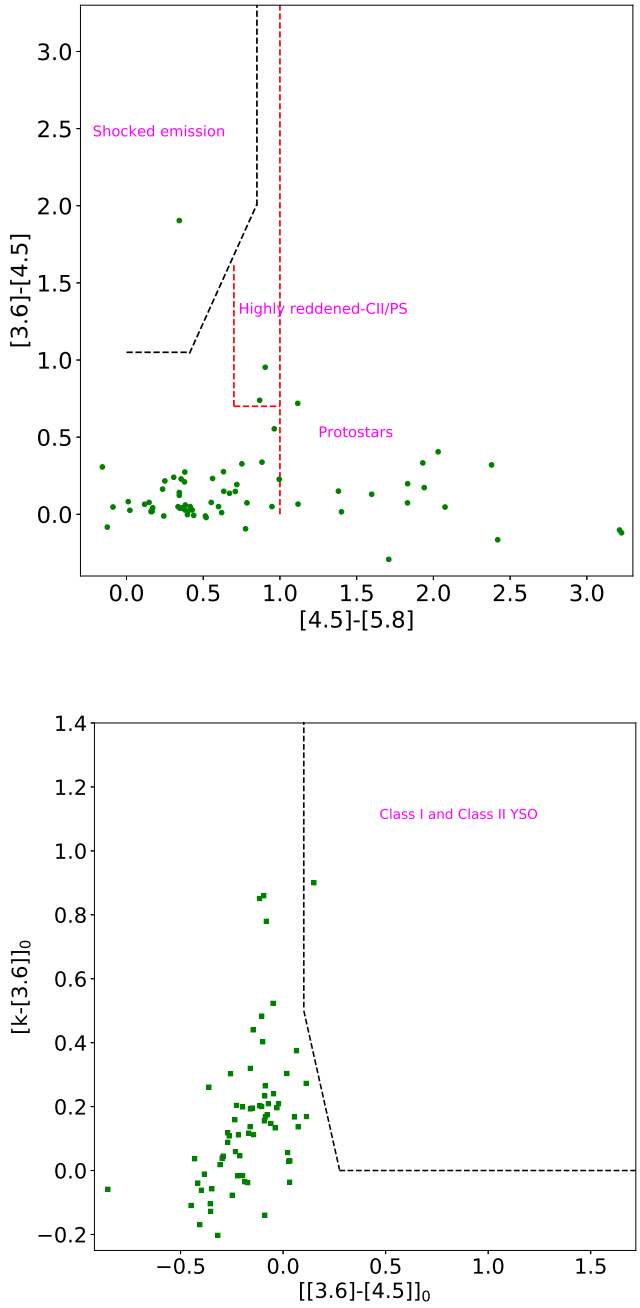

Figure 5.14: The top panel shows the color-color diagram of the *Spitzer*-GLIMPSE point sources within the searching radius centered at G18.15. Sources that are detected in the IRAC bands at 3.6, 4.5, and 5.8 μm simultaneously are plotted in the diagram. Regions belonging to different classes of objects are shown following the color conditions given in Gutermuth et al. (2008). The bottom panel shows the color-color diagram of the *Spitzer*-GLIMPSE point sources detected in the J, H, and K bands of the 2MASS survey along with 3.6 and 4.5-μm IRAC bands simultaneously.

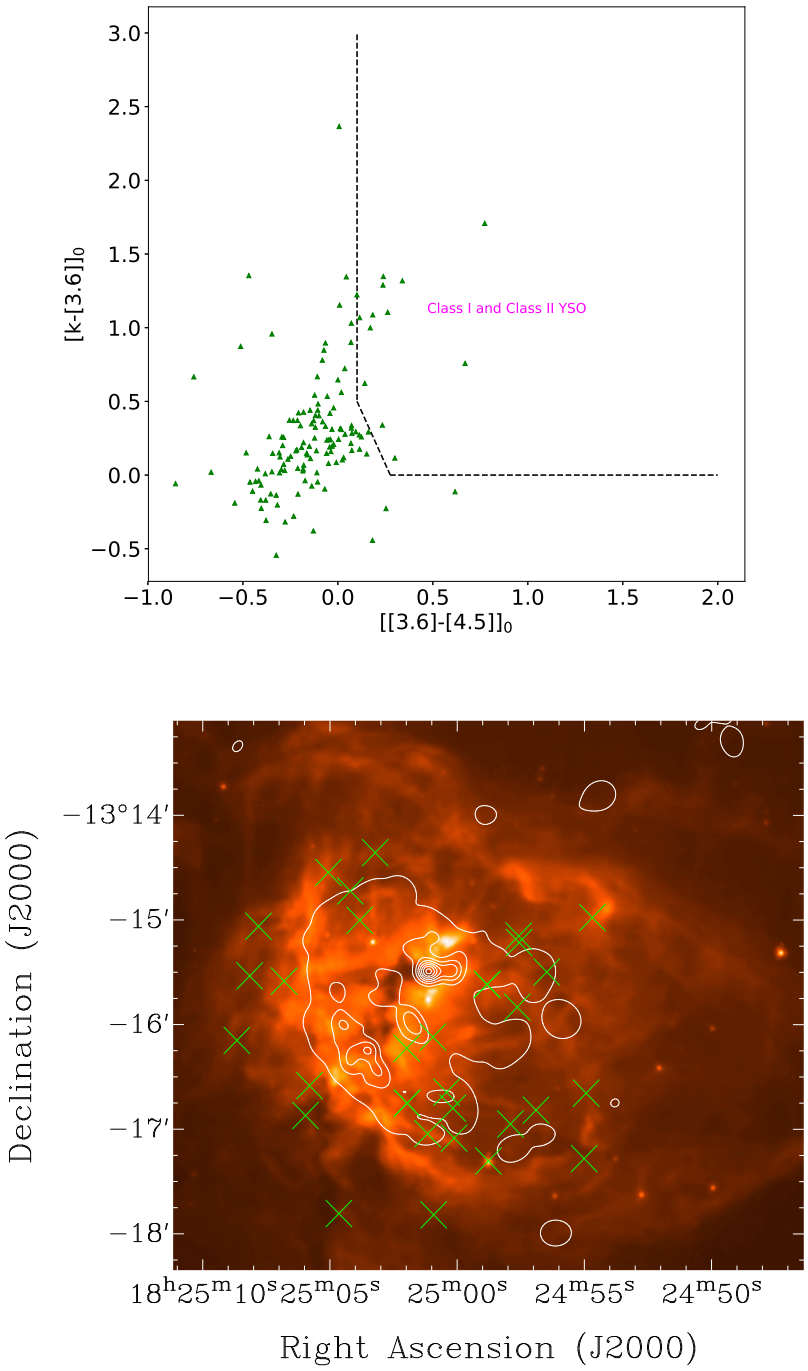

Figure 5.15: (Top) The panel shows the color-color diagram of the *Spitzer*-GLIMPSE point sources detected in the J, H, and K bands of UKIDSS along with 3.6 and 4.5 μm bands of IRAC simultaneously. The JHK-colors of UKIDSS are converted to the JHK-colors of 2MASS following Carpenter (2001) before constructing the color-color diagram. (Bottom) The panel shows the locations of the YSOs (green crosses) that are detected from the GLIMPSE, 2MASS, and UKIDSS surveys on the 8-μm warm dust emission map towards G18.15.

1980):

$$t_{dyn} = \left[\frac{4}{7}\frac{R_s}{c_i}\right]\left[\left(\frac{R}{R_s}\right)^{7/4} - 1\right], \tag{5.7}$$

where c_i is the sound speed in the ionized medium and is assumed to be 10 km s^{-1}. The radius of the H II region (R) is estimated to be 1.31 pc considering the radio continuum emission above 3σ level, and the mean value of hydrogen column density calculated using the same area obtained from the radio continuum is equal to 1.43×10^{22} cm^{-2}. Consequently, n_0 and R_s are estimated to be 5.3×10^3 cm^{-3} and 0.186 pc respectively. Since the size of the H II region is larger than that of the Strömgren sphere, the expansion of G18.15 is currently pressure-driven. Using eq. 5.7, we derive the dynamical age of G18.15 to be 0.31 Myr.

5.4.2 Signatures of a CCC in G18.15

The characteristic observational features of a CCC are the overlapping distribution of the colliding clouds, the presence of two velocity components in the CO spectra (Habe & Ohta, 1992; Takahira et al., 2018), and the "broad-bridge" feature connecting the velocity peaks at the intermediate velocity range (Haworth et al., 2015). G18.15 manifests many of these characteristics that suggest that it is a site of a CCC event.

The RRL data show two distinct velocities with a region of intermediate velocity separating them spatially. In addition, the spectrum of ^{12}CO molecular emission also shows two velocity components connected by a narrow plateau-like emission profile at the intermediate velocities (Fig. 5.6). The velocity peaks of the CO emission are seen to be in close correspondence with that of the RRLs, indicating that both the CO and RRL emission are tracing the same molecular clouds.

To further test the CCC hypothesis, we have searched for the presence of a "broad-bridge" like feature connecting the two molecular clouds in the position-velocity (PV) diagram. The bottom panel of Fig. 5.16 shows the PV diagram from the COHRS data generated across the white line shown in the top panel of the exact figure wherein the bridging features are visible. An approximate location of these features is shown using a yellow ellipse on the white line. However, the observed "broad-bridge" features in the CO (J=3$-$2) PV diagram are much weaker than what is observed in the simulations of Haworth et al. (2015). This is surprising since the bridge feature must be strong at a phase where the cloud-cloud interaction has triggered star formation in the colliding clouds.

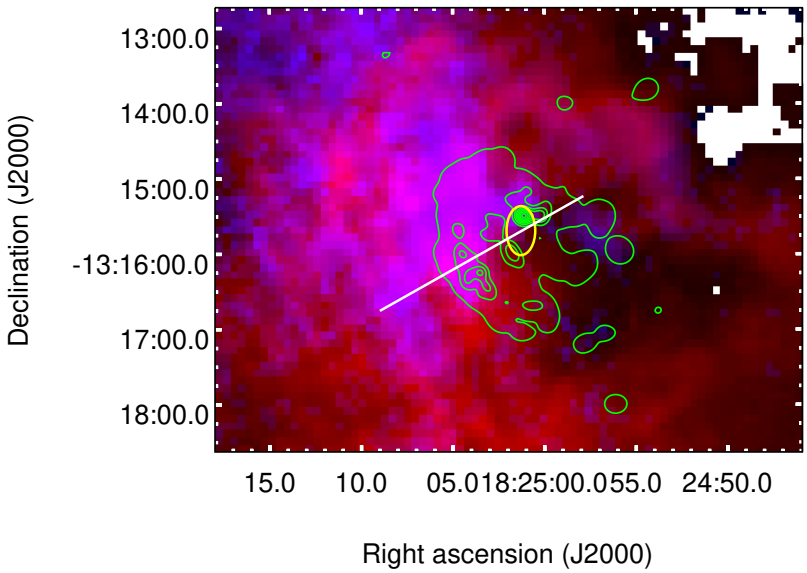

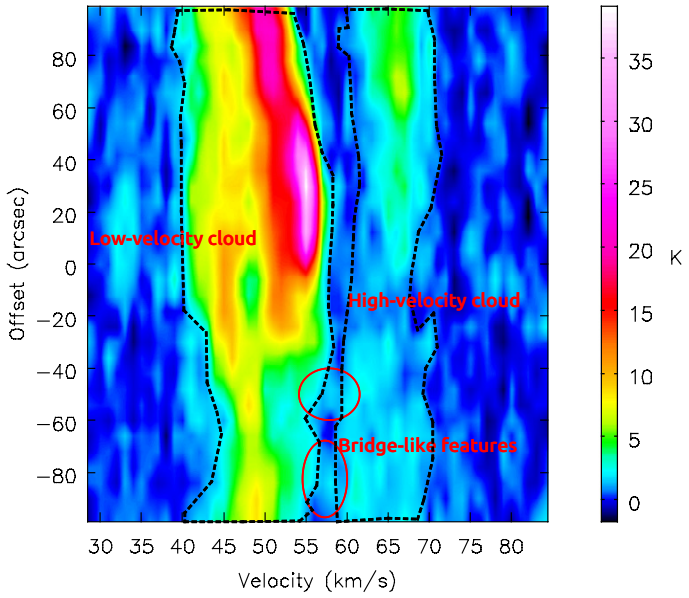

Figure 5.16: (Top) The ^{12}CO (J=3−2) intensity integrated within the velocity 39 to 55 km s^{-1} (red) and 56 to 74 km s^{-1} (blue) are shown in a two-color composite image. The white solid line shows the direction along which the position-velocity diagram is extracted. The radio continuum contours in green are identical to those in Fig. 5.3. (Bottom) The panel shows the position-velocity diagram extracted along the direction shown in the top panel. The "broad-bridge" like features are visible, and are encircled in red. An approximate position of the feature located at an offset $\approx 50''$ is shown in a yellow ellipse in the upper panel.

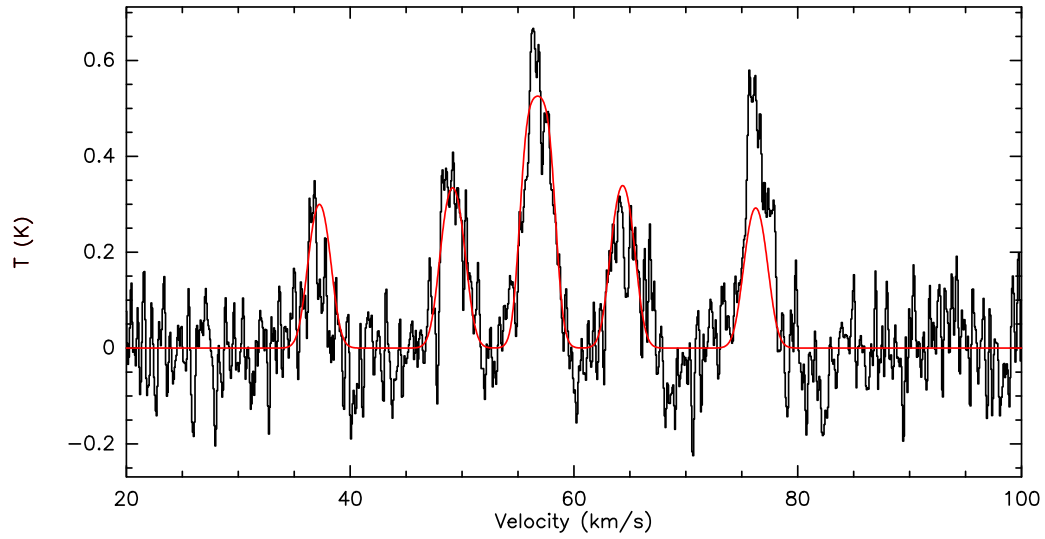

Figure 5.17: The figure shows the $NH_3(1,1)$ inversion spectrum towards G18.15. The line peaks at 56.8 $\pm$ 0.03 km s^{-1}, matching the velocity of the compressed layer.

Moreover, the J=3−2 transition of CO is expected to be a better tracer of dense, compressed gas compared to the (1−0) transition in the Haworth et al. (2015) simulations. However, the NH_3 spectrum towards the region from the *Red MSX Survey* (Urquhart et al., 2011) using the *Robert C. Byrd Green Bank telescope* shows strong emission at the intermediate velocity of 56.8 $\pm$ 0.03 km s^{-1} (Fig. 5.17). Since NH_3 is an excellent tracer of the dense gas, this strongly suggests the presence of a significant amount of dense gas in the collision interface. This agrees with the simulations of Priestley & Whitworth (2021) where molecules tracing dense gas were observed to have strongly enhanced emission in the shock-compressed layer between colliding clouds. The smooth velocity gradient in the RRL emission also suggests that the bridge feature may be visible in a PV diagram constructed from the RRL data. This is indeed the case, as seen in Fig. 5.18, wherein the bridge feature is as prominent as the component at high velocity. The prominent bridge feature in the RRL data, along with the presence of dense molecular gas at the intermediate velocity, add to the evidence of G18.15 being a possible site of a cloud-cloud collision.

Moreover, the far-infrared emission and mid-infrared absorption reveal a dense filament that passes through the central regions of G18.15, extending further to the south, and the mean magnetic field orientation is estimated to be perpendicular to the central filament within the H II region. Although the magnetic field geometry by itself cannot be taken to be evidence for a CCC, it adds to the results obtained from the PV diagram and suggests a CCC hypothesis behind the formation of G18.15.

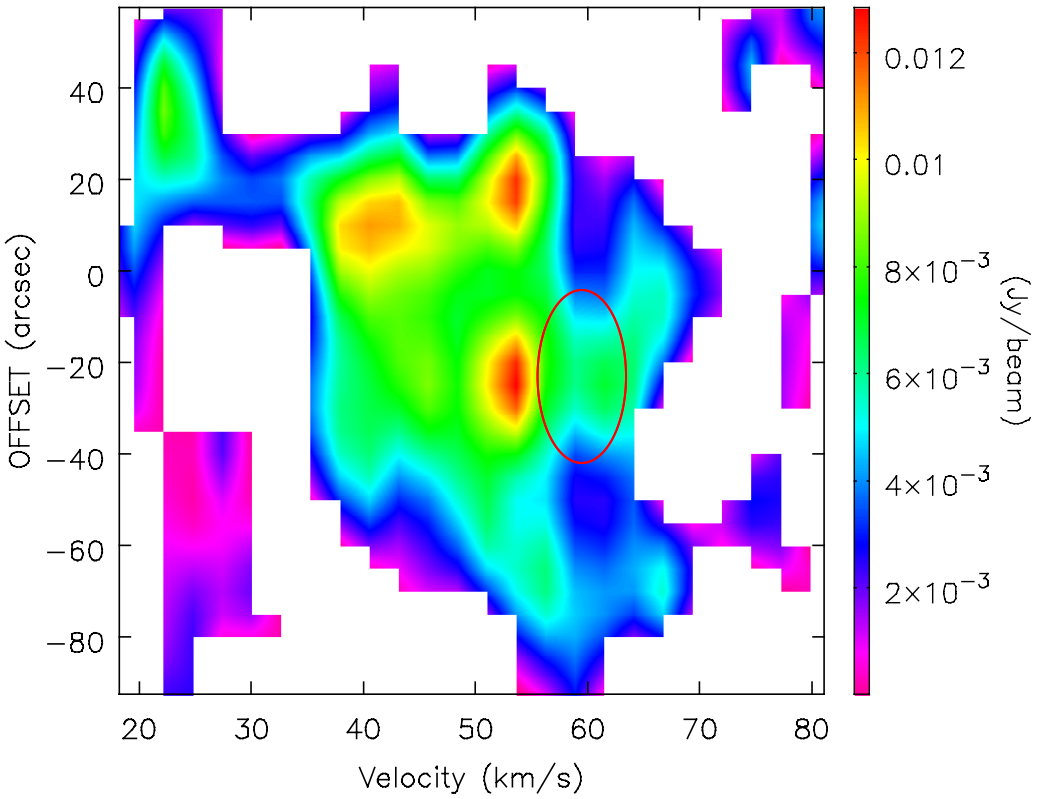

Figure 5.18: The figure shows the position-velocity diagram generated using the RRL emission towards G18.15. The diagram is extracted along the same locus as shown in the top panel of Fig. 5.16. The highlighted "broad-bridge" feature is encircled in red.

In addition to the massive stars inhabiting G18.15, the detection of several YSOs suggests that star formation is actively ongoing in the cloud complex. As mentioned earlier, the presence of extended emission at mid-infrared wavelengths and the high extinction as seen by the dark features at 8.0 μm suggest a significant undetected population of YSOs and massive stars.

5.5 Summary

In this chapter, we have performed a multi-wavelength analysis of G18.15. Our major findings are listed below:

- Using high-resolution uGMRT data, we have detected multiple radio continuum peaks within G18.15. The H169α and H170α RRLs are also detected towards G18.15 and are stacked to increase the SNR of the final map. The RRL data reveal two distinct velocity components in G18.15.

- The electron temperature is determined using the RRL and radio continuum data and is found to be 5200$-$9500 K at the location of the continuum peaks, which is consistent with the average electron temperature determined by previous studies using single-dish telescopes.

- The COHRS data reveal two molecular clouds with LSR velocities of 53.4 and 66.7 km s^{-1} respectively. A narrow plateau-like emission connects these two clouds at the intermediate velocities. The NH_3(1,1) inversion spectrum shows a strong peak at 56.8 km s^{-1} located within the intermediate velocity range.

- The position-velocity diagrams of ^{12}CO and RRL reveal the presence of "broad-bridge" features.

- The Herschel far-infrared emission and GLIMPSE 8.0 μm absorption reveal an IRDC filament with G18.15 at the northern edge.

- The mean orientation of the magnetic field lines is found to be perpendicular to the H II region.

- Using 2MASS and UKIDSS photometric data, star formation activity is investigated, and two O9 stars are identified towards G18.15. Although 30 YSOs have been detected towards this region, the extended emission at mid-infrared wavelengths and

high extinction suggest the presence of an undetected population of massive stars and YSOs.

- The dynamical age of G18.15 is estimated to be approximately 0.3 Myr.

Following the observational evidence presented in this chapter, we conclude that G18.15 is very likely to be formed due to a cloud-cloud collision event roughly 0.3 Myr ago.

Chapter 6

A multi-wavelength study of Galactic H II regions with extended emission

6.1 Introduction[1]

Massive stars emit copious amounts of Lyman-continuum photons that ionize their surroundings, creating H II regions. Initially, dense (sizes $\lesssim 0.03$ pc, density $\gtrsim 10^6$ cm^{-3}, and emission measure $\gtrsim 10^{10}$ pc cm^{-6}; Kurtz 2005) regions of ionized gas, known as HCHRs, form around the O and B-type stars, which evolve into UCHRs (sizes $\lesssim 0.1$ pc, density $\gtrsim 10^4$ cm^{-3}, and emission measure $\gtrsim 10^7$ pc cm^{-6}; Wood & Churchwell 1989; Kurtz et al. 1994; Kurtz 2005). The UCHRs continue to expand with time, eventually leading to the formation of compact and classical H II regions. Although the H II regions are generally bright at radio and infrared wavelengths, most of them are invisible at optical wavelengths because of the high degree of obscuration from the surrounding dust. The first studies of H II regions were carried out by Downes & Rinehart (1966), Mezger & Henderson (1967), and Ryle & Downes (1967) using single-dish radio telescopes to understand the nature of their continuum emission. The first large-scale interferometric survey of UCHRs was conducted by Wood & Churchwell (1989) (WC89 hereafter). They noticed that the Lyman-continuum photon rate estimated from the *Infrared Astronomical Satellite* (IRAS) fluxes is significantly higher than that obtained from the radio continuum. A similar disagreement was found by Kurtz et al. (1994), with the discrepancy being attributed to the absorption of the ionizing photons by the dust enclosed within the ionized region.

[1]This chapter is based on the published paper: Dey et al. (2024) [Jyotirmoy Dey, Jagadheep D. Pandian, and 10 co-authors, "A multi-wavelength study of Galactic H II regions with extended emission", 2024, Astronomy & Astrophysics, 689, A254]. The paper is reproduced here with minor changes.

Kurtz et al. (1994) also suggested an alternate explanation invoking the presence of a stellar cluster to explain the discrepancy above. Assuming that the mass distribution of stars in the cluster follows the typical initial mass function (e.g., Kroupa 2001), a massive star will be accompanied by a number of lower mass stars which will contribute to the infrared luminosity but not to the rate of ionizing photons. However, adopting an initial mass function from Kroupa (2001) and the mass-luminosity relation for main sequence stars (Salaris & Cassisi, 2005), the massive stars are found to account for greater than 90% of the total luminosity. Hence, the presence of a stellar cluster does not significantly alter the statistics of the discrepancy between the rate of ionizing photons inferred from radio and infrared wavelengths.

Meanwhile, later studies of Kurtz et al. (1999), Kim & Koo (2001), Ellingsen et al. (2005), and de la Fuente et al. (2020) showed that the presence of extended radio continuum emission that is directly associated with the UCHRs might also resolve the inconsistency between the Lyman-continuum photon rates. The extended emission is often undetected due to the poor sensitivity of interferometric observations to the emission on scales larger than that corresponding to the shortest baseline of the interferometer. The much larger radio continuum flux from the inclusion of extended emission gives rise to larger Lyman-continuum rates that are closer to those inferred from the infrared, thereby avoiding the need for high dust absorption as suggested by WC89 and Kurtz et al. (1994). A similar scenario may also occur for the CHRs, where the dust absorption could be overestimated due to the non-detection of extended emission surrounding the dense, compact cores (Habing & Israel, 1979). Another problem that may be addressed by including the extended emission is the "age problem" wherein the H II regions must remain in the UC phase for much longer than their sound crossing time in a homogeneous medium. The presence of extended emission surrounding the UCHRs will suggest that those regions are not as young as they appear from the observation of the UCHR alone.

In this chapter, we present results from a study of extended emission around eight CHRs and UCHRs using the *upgraded Giant Metrewave Radio Telescope* (uGMRT; Swarup 1990; Gupta et al. 2017) data covering 1.25–1.45 GHz, and 4–8 GHz data from the GLOSTAR (*A global view on star formation*) survey (Medina et al. 2019; Brunthaler et al. 2021). Both the uGMRT and GLOSTAR data are ideally suited to address the presence or absence of extended emission around CHRs and UCHRs. The uGMRT comprises a hybrid configuration of 30 antennas (shaped like a 'Y') with a central array consisting of 14 antennas within a 1 sq km region and the remaining 16 antennas on the 3 arms of the 'Y'. This gives excellent sensitivity to extended emission on scales smaller than $7'$ along with good angular

resolution ($\approx 2''$ at 1.4 GHz). The GLOSTAR survey comprises observations with the *Karl G. Jansky Very Large Array* (VLA) in its D and B-configurations along with zero spacing information from the 100-m *Effelsberg radio telescope*. The sensitivity of both uGMRT and GLOSTAR observations to extended emission allows us to carry out a comprehensive study of the role of the same in resolving outstanding questions of Galactic H II regions.

Although extended emission is frequently detected towards H II regions, it may or may not be associated with compact or ultracompact emission. Kurtz et al. (1999) proposed two methods to determine whether or not an extended emission is associated with compact or ultracompact cores. The first is to search for a discontinuity in the intensity of the continuum emission (a gap with near-zero emission). The presence of such a gap between the core and extended components would suggest that the two regions are physically distinct. However, one has to be careful applying this technique to interferometer data since a discontinuity can be created due to the filtering of large-scale emission. An alternate method is to look at the kinematics of the ionized gas using RRLs. The presence or absence of a smooth velocity distribution between the compact core and extended emission can be used to infer whether or not the two structures are physically associated. For example, Kim & Koo (2001) used H76α observations to examine (using the RRL velocity field) whether the compact and extended emission are physically connected in 16 H II regions and found physical association in all sources with one exception.

Our observations include RRLs in addition to radio continuum to establish the association of emission from the compact and extended components. Further, previous studies by Brocklehurst & Seaton (1972); Lockman & Brown (1975); Brown et al. (1978) have shown that low-density ($n_e \approx 10$ cm^{-3}) ionized gas emits more low-frequency or high-n (Hnα; n $\approx$ 150–180) RRLs compared to intermediate- or high-density gas ($n_e \approx 10^2$ cm^{-3} and $n_e \approx 10^3$ cm^{-3}), which show enhanced emission of low-n (n $\approx$ 80–120) RRLs (Fig. 1 of Brown et al. 1978). Since our uGMRT observations cover the H166–172α lines, and the GLOSTAR survey observes the H98–114α lines, we expect to be able to trace line emission from ionized gas over a range of densities, including the compact and extended regions.

This chapter is organized as follows. We describe the source selection criteria in Sect. 6.2. The radio observations with the uGMRT and subsequent data analysis using observed as well as archival data are described in Sect. 6.3. Sect. 6.4 presents the results obtained with notes on individual sources described in Sect. 6.5. In Sect. 6.6, we discuss the association of the extended emission with the H II regions and its role in resolving the outstanding problems associated with them.

6.2 Source selection

Since the primary focus of our study is to observe H II regions whose morphology at radio wavelengths comprises extended emission surrounding compact and ultracompact cores, we selected candidate sources that have an extended morphology visible from radio to mid-infrared wavelengths. First, we looked at sources classified as Galactic H II regions in the catalog of *The H I, OH, recombination line survey of the Milky Way* (THOR; Beuther et al. 2016; Wang et al. 2018). Considering the availability of calibrated images from the GLOSTAR survey at the time of the uGMRT observations, we constrained ourselves to the Galactic longitude region $18^\circ \leq l \leq 30^\circ$. The sources were selected to have a size of at least $1'$ so that the extended emission would be well detected in both the uGMRT observations and the GLOSTAR survey. Since one of our objectives is to study the dynamics of ionized gas, we also ensured that all sources have detections of RRLs in both THOR and GLOSTAR surveys. Finally, we examined the field surrounding the targets and only selected sources that are devoid of nearby bright sources, as the presence of such sources affects data calibration by contamination through the sidelobes of the primary beam. These selection criteria provided us with a sample of eight Galactic H II region candidates to observe using uGMRT (see Table 6.1). The kinematic distances to the sources range from 1.8 to 11.7 kpc (adopted from Urquhart et al. 2018 and references therein) while the angular size ranges from $1.5'$ to $3.7'$.

It is to be noted that the angular sizes in Table 6.1 translate to physical sizes ranging from 0.9 to 9.2 pc, which are much larger than those of UCHRs. This is due to the detection of extended emission by the THOR survey. The nature of the target H II regions, including whether or not the sources are bona fide UCHRs, is examined in Sect. 6.4.1.

6.3 Observations and data analysis

6.3.1 uGMRT observations and archival data

We observed the targets using the *upgraded Giant Metrewave Radio Telescope* (uGMRT; Swarup 1990; Gupta et al. 2017) with the GWB correlator as the backend (proposal codes 37_073 and 40_100; see Table 6.2 for the dates of observations). The correlator was configured to have a bandwidth of 200 MHz centered at 1350 MHz (Band-5) with 8192 channels. A total of seven RRLs (H166α – H172α) were covered in this bandwidth. At the observed frequency, uGMRT has a native resolution of $\approx 2''$ and the largest detectable angular scale

of $\approx 7'$ in Band-5. The radio sources 3C48 and 3C286 were used as the bandpass and flux calibrators according to their availability, whereas J1822−096 was used as the gain calibrator, which has a flux density of 5.6 Jy in this band. The on-source time ranged from 2 to 8 hours depending on their peak and extended flux densities, as seen in the THOR survey.

The radio data are reduced using the NRAO *Common Astronomy Software Applications* (CASA; McMullin et al. 2007) package. For the details on the radio data reduction, please refer to Sect. 4.1.2. After completing this step, the net bandwidth left for imaging the targets was around 150 MHz, considering only the line-free channels. The targets were then imaged using the `tclean` task, and the dynamic range of the continuum images was improved by self-calibration. The final 1σ noise in the continuum images is 60–70 μJy beam^{-1}, and the synthesized beam ranged from 1.7–3.2$''$. The uncertainty in flux calibration is estimated to be better than 10%, based on comparing the flux density of the gain calibrator to its standard value after applying the gain solutions. The flux densities of the target sources were also compared with that of the nearest sub-band of the THOR survey and were found to agree to better than 10%.

As shown in Table 6.2, 8192 channels were used to observe the targets, providing a native velocity resolution of ~ 5 km s^{-1}. The RRL data were imaged using the `clean` task. Since the RRLs are weak, especially in the regions of extended emission, we used a restoring beam of 25$''$ for imaging the RRLs. To further enhance the signal-to-noise ratio, four RRL images (H167α – H170α; the other lines were either affected by RFI or were located at the edges of the passband) were stacked to the observed frequency of H169α using the package `LineStacker` (Jolly et al., 2020)[2]. This results in an improvement in the signal-to-noise ratio of the line image by a factor of 2, with the final images having an rms noise of ~ 0.30 mJy beam^{-1} per 5 km s^{-1} spectral channel.

Additionally, multiple archival data are used (see Sect. 4.2) to complement our uGMRT observations. These data include near-infrared data from the 2MASS and UKIDSS surveys, mid-infrared data from the GLIMPSE and MIPSGAL surveys, far-infrared data from the Hi-GAL survey, and radio data from the MAGPIS, CORNISH, and GLOSTAR surveys.

[2]`https://github.com/jbjolly/LineStacker/releases`

Table 6.1: Properties of the target sources.

Source name	RA (J2000)[a] (hms)	DEC (J2000)[a] (dms)	d[b] (kpc)	V_{LSR}[b,c] (km s^{-1})	D (arcmin)	S_p (Jy beam^{-1})	S_{int} (Jy)
*G19.68−0.13	$18^h27^m23.40^s$	–11°49′52.78″	11.7	55.0	1.5	0.211	0.683 ± 0.015
*G20.99+0.09	$18^h29^m04.73^s$	–10°34′15.59″	1.8	18.6	1.8	0.228	1.221 ± 0.011
G22.76−0.48	$18^h34^m26.70^s$	–09°15′48.66″	4.9	74.8	3.6	0.164	1.703 ± 0.014
G24.47+0.49	$18^h34^m10.19^s$	–07°17′57.96″	5.9	99.8	2.1	0.798	3.452 ± 0.022
G25.69+0.03	$18^h38^m04.03^s$	–06°25′31.45″	11.7[d]	51.9	2.7	0.149	0.961 ± 0.017
*G27.49+0.19	$18^h40^m49.01^s$	–04°45′04.04″	2.2	32.5	3.7	0.252	1.873 ± 0.020
G28.30−0.39	$18^h44^m21.85^s$	–04°17′37.16″	9.7	85.5	1.5	0.203	0.746 ± 0.019
*G28.81+0.17	$18^h43^m16.84^s$	–03°35′27.23″	7.9	103.0	2.1	0.358	1.605 ± 0.016

Note – * = sources comprise of multiple fragments of compact emission,
a = coordinates of the H II region from the radio continuum catalog of Wang et al. (2018),
b = adopted kinematic distance from Urquhart et al. (2018) and references therein,
c = LSR velocities from Lockman (1989),
d = revised to far distance based on the H I absorption spectrum,
D = size of the UCHR (including the extended emission) using THOR data,
S_p = peak intensity at the 1.31 GHz spectral window of the THOR survey,
S_{int} = integrated intensity at the 1.31 GHz spectral window of the THOR survey.

Table 6.2: Details of our observation using uGMRT.

Parameter	Value
Observation date	2019 Dec 1, 2, 6, 10, 14 2021 Sep 14, 26, 27, 28 2021 Oct 5, and 2021 Nov 28
No. of channels	8192
Central frequency	1350 MHz
Bandwidth	200 MHz
Primary Beam	$25'$
Synthesised Beam	$\approx 2''$

6.3.2 Infrared spectral energy distribution

As mentioned in Sect. 4.5, we have used mid and far-infrared data from the GLIMPSE, MIPSGAL, and Hi-GAL surveys to construct the global SED of dust emission at these wavelengths. Before any SED modeling, The GLIMPSE and MIPSGAL images were processed (see Sect. 4.4 for the procedure) using the MOPEX package for eliminating the point sources and estimating the total flux density, including the extended emission.

We also verified the accuracy of point source removal by estimating the flux density in extended emission in two ways: first, we used the method outlined above to remove the point sources and measure the total flux density after point source removal. Alternately, we performed photometry on the region covered by the H II regions, including point sources. We then estimated the total flux density of the point sources within the aperture used for photometry using the GLIMPSE point source catalog (Benjamin et al., 2003). We then subtracted this from the total flux density to estimate the flux density from extended emission. We found both methods to agree within 3–8%, validating our approach. The mid-infrared flux densities from the GLIMPSE and MIPSGAL surveys are then combined with those from the Hi-GAL survey to construct the infrared SED of the H II regions.

To determine the infrared luminosity of our targets, we have fit the SED through radiative transfer modeling. We have used the `DustEM` package (Compiègne et al., 2011)[3] for this purpose. A sample SED, along with the best fit from `DustEM`, are shown in Fig. 6.1.

[3] `https://www.ias.u-psud.fr/DUSTEM/`

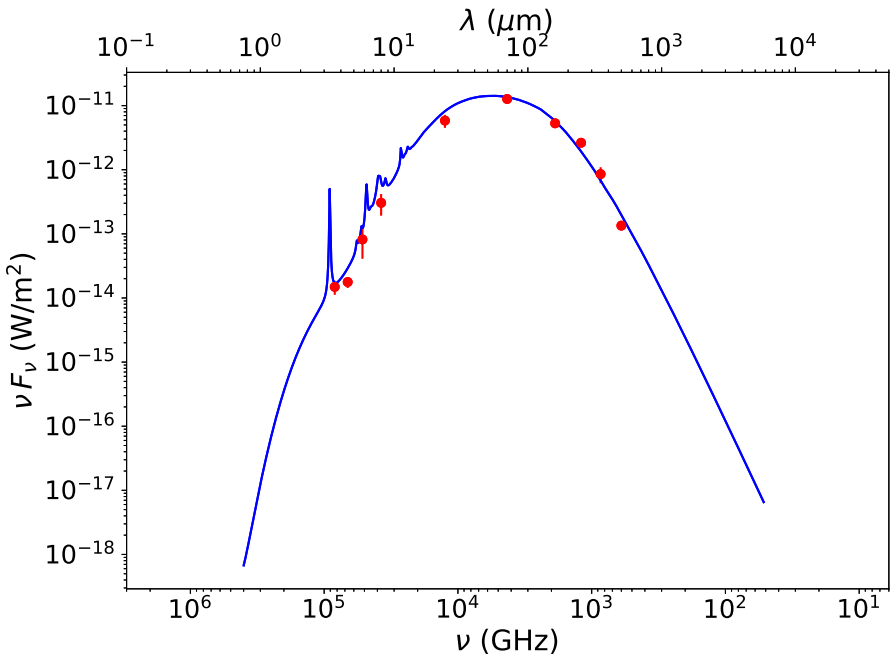

Figure 6.1: One example SED for one of our target sources fitted using DustEM.

6.3.3 Identification of candidate ionizing stars

To identify the candidate ionizing stars within the target sources, we constructed color-magnitude and color-color diagrams using photometric data of near-infrared point sources from the 2MASS and UKIDSS surveys.

First, we extracted Galactic point sources from the 2MASS and the UKIDSS GPS (sixth archival data release; UKIDSSDR6plus) catalogs using a circular search radius of $4'$ centered at the coordinates given in Table 6.1. Next, we created (see Sect. 4.6 for details) color-magnitude (CMD) and color-color diagrams (CCD) using the Bessell & Brett homogenized system (Carpenter, 2001) for both 2MASS and UKIDSS sources. We then overplotted the loci of OB-type stars in both the CMD (assuming the distance to the UCHR as per Table 6.1) and CCD using the reddening law of Bessell & Brett (1988). The Fig. 6.2 shows sample CMDs and CCDs along with reddening vectors with crosses placed at intervals of $A_V = 5$. The stars that are located in both the CMD and CCD with colors expected for OB-type stars and with the same visual extinction in both diagrams are selected as candidate ionizing stars.

6.4 Results

6.4.1 Radio emission

6.4.1.1 Radio continuum

We detected extended emission around all the sources in both uGMRT and GLOSTAR (GLOSTAR-D and GLOSTAR-D+Eff) observations. Fig. 6.3 shows an example of radio continuum emission at $2''$ resolution using the uGMRT with the $18''$ resolution GLOSTAR-D emission overlaid in contours (the images for the full sample are provided in the top panels of Fig. B.1). Notably, there are no morphological differences between the continuum images at 1.35 GHz and 5.79 GHz.

The integrated flux densities of the sources in the GLOSTAR-D+Eff maps are typically larger than that seen in GLOSTAR-D alone (Table 6.3), indicating that some emission is resolved in the latter.

6.4.1.2 Spectral index

Table 6.3 shows the in-band spectral indices from the GLOSTAR-D data around the location of the peak emission and the inter-band spectral indices estimated from the integrated flux densities of the sources in uGMRT and GLOSTAR-D. We find that the spectral index (α; $S_\nu \propto \nu^\alpha$) is close to -0.1 in all cases, indicating that the emission is thermal and optically thin at frequencies greater than 1.35 GHz.

However, the high-resolution radio continuum images show the emission to be clumpy, with several sources showing pockets of compact emission that are surrounded by diffuse extended emission. To explore the nature of compact emission, we have examined the spectral index using GLOSTAR-B data, which is only sensitive to emission on scales smaller than $4''$. We detect pockets of compact emission at the 3σ-level or greater in the GLOSTAR-B maps for four out of eight sources (G22.76$-$0.48, G24.47$+$0.49, G25.69$+$0.03, and G28.30$-$0.39). The GLOSTAR-B in-band spectral index was found to range from 1.21 to 1.97 for these pockets; however, the uncertainty in the spectral index is high (often exceeding 100%) due to the low signal-to-noise ratio. Although the high uncertainties are a caveat, a positive spectral index up to the frequency of GLOSTAR surveys requires emission measures greater than $\sim 10^8$ pc cm^{-6}, which coupled with their compact sizes ($\lesssim 0.1$ pc) is indicative of electron densities that are found in ultracompact H II regions (Kurtz, 2005).

We have also determined the inter-band spectral index for pockets of compact emission that are detected in both the uGMRT observations and the *Co-Ordinated Radio 'N' Infrared Survey for High-mass star formation* (CORNISH; Hoare et al. 2012) survey. We find the spectral index to be positive (even after accounting for uncertainties) in all cases, showing that the compact emission is optically thick thermal emission.

The results above are characteristic of hierarchical density structure in H II regions, similar to that observed by Kim & Koo (2002) and Yang et al. (2021). Although many H II regions are observed to have pockets of compact emission whose electron densities are similar to that found in UCHRs, the overall emission is dominated by the diffuse emission that is optically thin down to 1.35 GHz or lower. Thus, high-resolution observations that are not sensitive to extended emission (e.g., WC89, CORNISH, GLOSTAR-B) are dominated by the compact emission components that have a positive spectral index, whereas the spectral index from lower resolution observations (e.g., GLOSTAR-D, integrated emission from uGMRT) is close to -0.1.

6.4.1.3 Source classification

As indicated in Sect. 6.1, H II regions are classified based on their size, electron density, spectral index, and emission measure. However, the hierarchical density structure makes the classification of the H II regions in our sample challenging. Based on the detected compact emission alone (at the 3σ-level of GLOSTAR-B data and the CORNISH survey), four out of eight sources (G22.76−0.48, G24.47+0.49, G25.69+0.03, and G28.30−0.39) would be classified as UCHRs, according to their sizes ($\lesssim 0.1$ pc) and emission measures ($\gtrsim 10^7$ pc cm^{-6}), with G24.47+0.49 and G25.69+0.03 being already classified as UCHRs in the catalogs of Purcell et al. (2013) and de la Fuente et al. (2020) (see Sect. 6.5 for more details).

The compact emission from the other four sources (G19.68−0.13, G20.99+0.09, G27.49+0.19, and G28.81+0.17) is seen to be fragmented in the CORNISH maps, which is an artifact of the `CLEAN` process (during imaging of the interferometric data) when the resolution is significantly higher than the scale of extended emission. The overall size of the envelope that encompasses all the fragmented emission is found to range from 0.2 to 1.2 pc. Thus, following the 'size' criteria, these H II regions cannot be classified as UCHRs. Hence, a classification scheme based on the size and spectral index of dense emission alone would result in the sample comprising four UCHRs and four compact H II regions. However, if the extended emission is included, all eight sources would be classified as compact H II regions. It is to be noted that many early surveys that classified Galactic H II

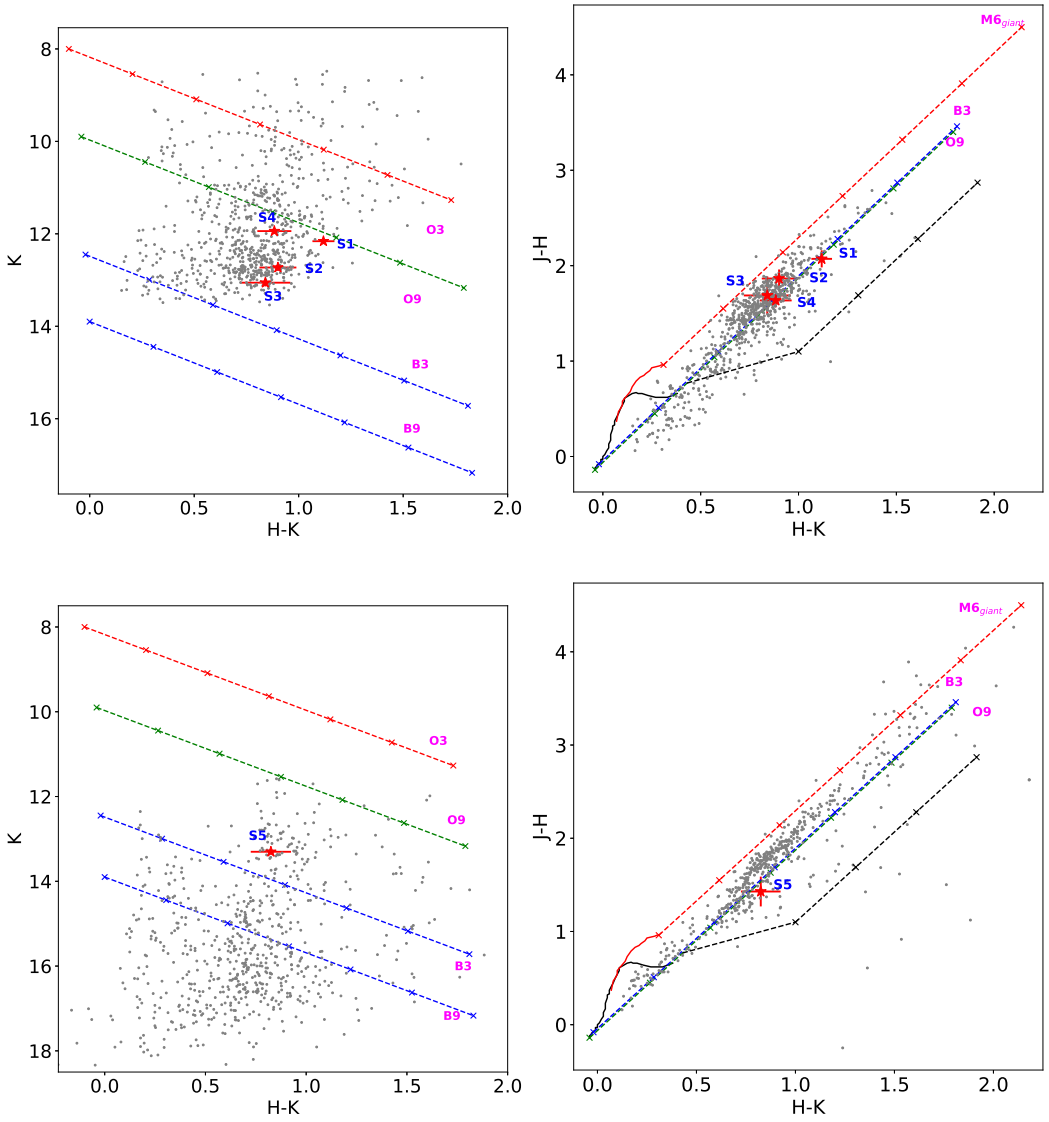

Figure 6.2: Images showing the color-magnitude and color-color diagrams of the 2MASS and UKIDSS point sources. Top left: K vs. $H-K$ color-magnitude diagram of the 2MASS near-infrared point sources within a circle of radius $4'$ centered at G19.68–0.13. The reddening vectors of the massive stars (O3–B9) are plotted on the color-magnitude diagram. Top right: $J-H$ vs. $H-K$ color-color diagram of the 2MASS point sources with spectral type earlier than B9 in the color-magnitude diagram. The solid black and red lines represent the loci of Class V (main sequence stars) and Class III (giant stars) objects respectively (Bessell & Brett, 1988; Cox, 2000). The black long-dashed line represents the locus of the T-Tauri stars (Meyer et al., 1997). The reddening vectors corresponding to the different classes are also shown using dotted lines with crosses placed at an increasing interval of $A_V = 5$. The candidate ionizing stars are shown using red '*' with respective error bars. Bottom row: same as the top row but for the point sources detected in the UKIDSS survey.

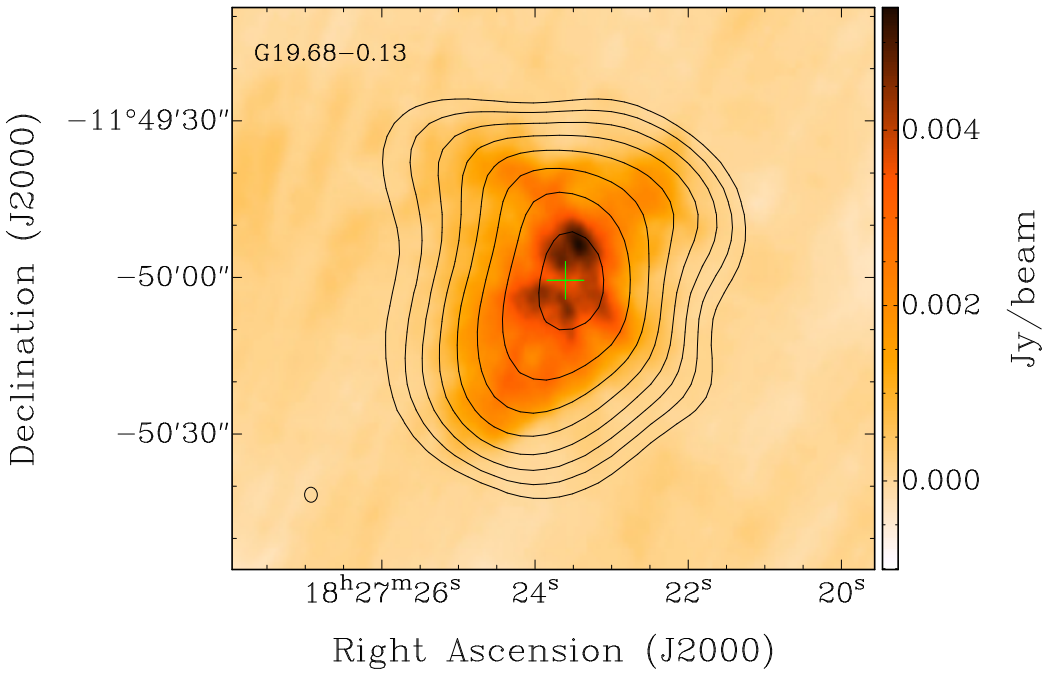

Figure 6.3: uGMRT radio continuum map of G19.68−0.13 overlaid with the radio contours from the GLOSTAR-D continuum map in black. The contours start at the 3σ-level flux and increase in steps of $\sqrt{2}$. The location of G19.68−0.13 reported in the THOR radio continuum catalog is shown using a green '+' sign. The corresponding beam size is shown at the bottom-left corner of the figure.

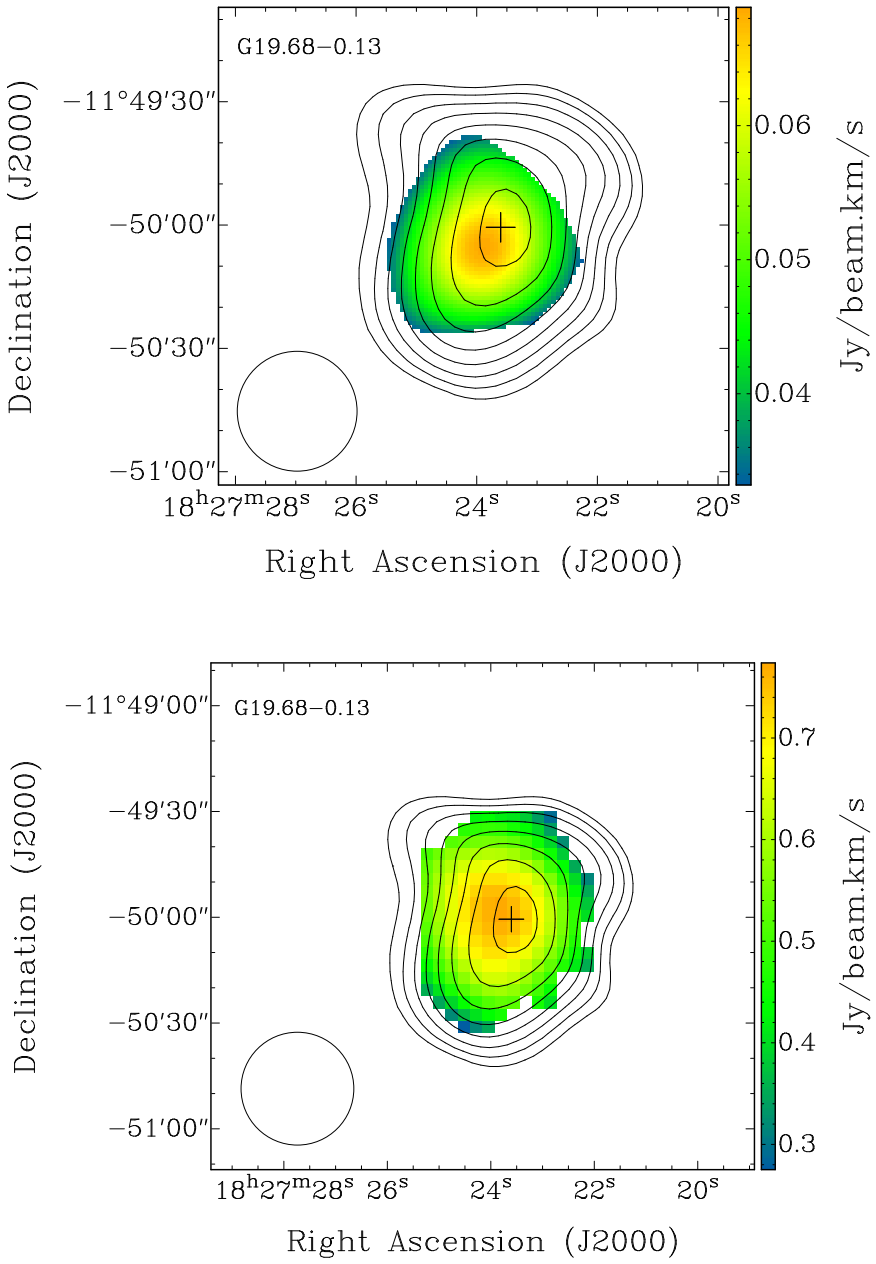

Figure 6.4: Images showing the moment-0 maps of G19.68−0.13 overlaid with the radio contours from the GLOSTAR-D continuum maps in black. Top: uGMRT, Bottom: GLOSTAR-D. The contour levels are similar to those in Fig. 6.3. The location of G19.68−0.13 reported in the THOR radio continuum catalog is shown using a black '+' sign. The respective beam sizes are shown at the bottom-left corners of the figures.

Table 6.3: Properties of the radio continuum emission using uGMRT and GLOSTAR data.

Source name	S_ν (1.35 GHz) (Jy)	S_ν (5.79 GHz) (Jy)	S_ν (5.85 GHz) (Jy)	$\log(N_{Ly})$ (1.35 GHz)	$\log(N_{Ly})$ (5.85 GHz)	ZAMS	T_e (K)	D_{UC} (pc)	α_{UC}	α_p	α
*G19.68−0.13	0.622 ± 0.012	0.481 ± 0.018	0.57 ± 0.07	$48.82\ (^{0.03}_{-0.03})$	$48.85\ (^{+0.06}_{-0.07})$	O6.5	9627	–	–	–0.070	–0.098
*G20.99+0.09	1.344 ± 0.014	0.630 ± 0.017	1.17 ± 0.10	$47.54\ (^{0.20}_{-0.35})$	$47.55\ (^{+0.19}_{-0.36})$	B0	9162	–	–	–0.132	–0.156
G22.76−0.48	1.788 ± 0.025	0.672 ± 0.013	1.81 ± 0.11	$48.56\ (^{0.05}_{-0.06})$	$48.63\ (^{0.05}_{-0.07})$	O7	8216	0.08	1.97 ± 2.19	–0.136	–0.144
G24.47+0.49	3.178 ± 0.006	3.502 ± 0.012	3.76 ± 0.15	$48.98\ (^{0.04}_{-0.05})$	$49.12\ (^{0.04}_{-0.06})$	O6	7956	0.11	1.96 ± 1.98	–0.121	–0.129
G25.69+0.03	0.883 ± 0.016	0.533 ± 0.019	0.83 ± 0.06	$49.02\ (^{0.04}_{-0.04})$	$49.06\ (^{0.05}_{-0.06})$	O6	7680	0.04	1.66 ± 0.38	–0.126	–0.137
*G27.49+0.19	1.701 ± 0.014	0.785 ± 0.011	1.47 ± 0.08	$47.87\ (^{0.13}_{-0.20})$	$47.87\ (^{0.13}_{-0.21})$	O9.5	7213	–	–	–0.139	-0.151
G28.30−0.39	0.820 ± 0.015	0.654 ± 0.010	0.71 ± 0.07	$48.80\ (^{0.04}_{-0.05})$	$48.80\ (^{0.06}_{-0.07})$	O6.5	8829	0.11	1.21 ± 5.60	–0.113	-0.132
*G28.81+0.17	1.462 ± 0.012	0.971 ± 0.014	1.30 ± 0.09	$48.89\ (^{0.04}_{-0.05})$	$48.90\ (^{0.05}_{-0.06})$	O6.5	8276	–	–	–0.125	-0.147

Note – * = sources comprise of multiple fragments of compact emission,
D_{UC} = size of the UCHR (excluding the extended emission) using the GLOSTAR-B data,
α_{UC} = spectral index of the UCHR (excluding the extended emission) using the GLOSTAR-B data,
α_p = spectral index using the in-band GLOSTAR-D flux densities within a grid of 3×3 pixels centered at the pixel with the peak emission,
α = spectral index estimated using the uGMRT and GLOSTAR-D integrated flux densities.

regions as UCHRs have been carried out at high angular resolution with relatively poor sensitivity to extended emission (e.g. WC89, CORNISH). The semantics of how to classify H II regions that have a hierarchical structure with extended emission that co-exists with compact emission is an open question. Although the presence of extended emission presents difficulties in the classification of H II regions, it plays an important role in resolving the outstanding problems associated with UCHRs, as demonstrated in Sect. 6.6.

6.4.1.4 RRL emission

In addition to the radio continuum maps, we have RRL data cubes of the target regions at an angular resolution of 25″. These cubes are used to trace the dynamics of ionized gas, effects of feedback from H II regions on the surrounding environment, the electron temperature (e.g., Quireza et al. 2006), etc. In addition, the line velocity can be used to estimate the kinematic distance to the source.

The top and bottom panels of Fig. 6.4 show the moment-0 or velocity-integrated maps of G19.68−0.18 from the uGMRT and GLOSTAR-D, respectively. Although the two datasets are expected to trace different gas densities, the distribution of RRL emission is seen to be very similar in both maps. Fig. 6.5 shows the velocity field of the ionized gas using GLOSTAR-D, obtained by fitting a Gaussian profile to the RRL line at each pixel that has a signal-to-noise ratio greater than 3. The velocity field using the uGMRT data is similar but at a lower signal-to-noise ratio due to the lower line intensities at higher Hnα transitions. Although limited by the signal-to-noise ratio, the lack of any significant differences in either the extent of RRL emission or the velocity field between uGMRT and GLOSTAR-D suggests that both datasets trace the same ionized gas. The moment-0 maps and velocity field for the full sample are shown in Fig. B.1 (bottom panels) and Fig. B.2, respectively, and the velocity fields of individual sources are discussed in Sect. 6.5. The line widths of the RRLs range from 24 to 30 km s^{-1}, which is typical of compact and ultracompact H II regions (e.g., WC89, Kim & Koo 2001).

6.4.2 Electron temperature

We have used the RRL line-to-radio continuum ratio to estimate the electron temperature (T_e) in the target H II regions (see Appendix A for details on the methodology). The T_e in our sample ranges from 7200 K to 9600 K (see Table 6.3). A visual inspection of the data shows an increasing T_e with an increase in the galactocentric distance of our sample. Our results are broadly consistent (within 300–400 K) with the relation between T_e and

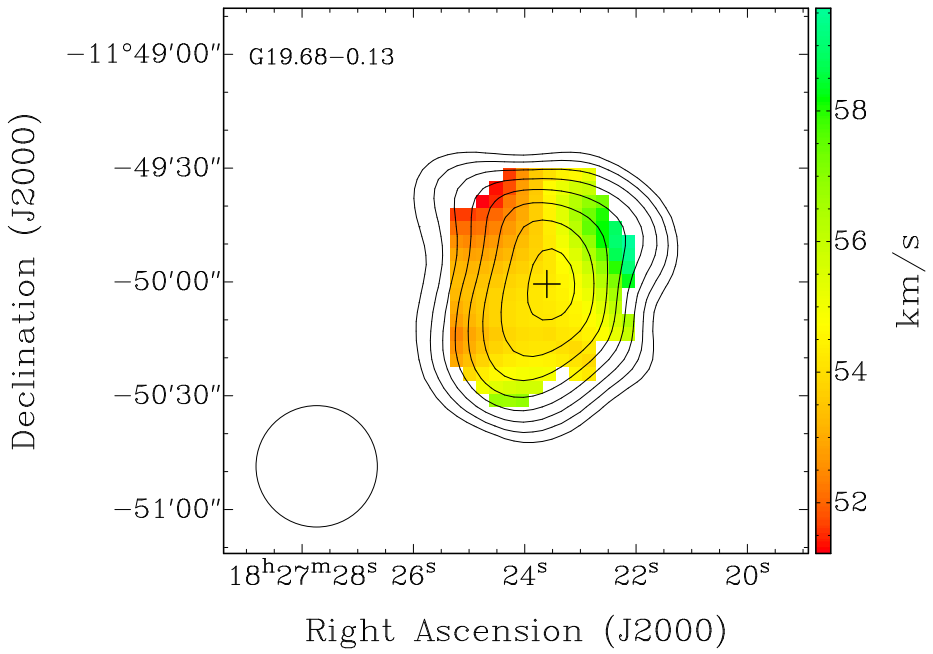

Figure 6.5: RRL peak velocity distribution map of G19.68−0.13 from the GLOSTAR-D data overlaid with the GLOSTAR-D radio continuum contours in black. The contour levels are similar to those in Fig. 6.3. The location of G19.68−0.13 reported in the THOR radio continuum catalog is shown using black '+', and the corresponding beam size is shown at the bottom-left corner of the figure.

galactocentric radius (e.g., Quireza et al. 2006) that is a consequence of the metallicity of the Galactic disk decreasing with galactocentric radius. However, for G19.68−0.13 and G27.49+0.19, our estimated T_e values are within 900–1000 K of the relation given in Quireza et al. (2006).

6.4.3 Energetics of the target H II regions

The Lyman-continuum photon rate can be inferred from the measured radio flux density using the following equation (Schmiedeke et al., 2016):

$$N_{Ly} \geq 4.76 \times 10^{42}\ \nu^{0.1}\ d^2\ S_\nu\ {T_e}^{-0.45}, \tag{6.1}$$

where S_ν is the flux density in Jy, ν is the frequency in GHz, d is the distance to the source in pc, and T_e is the electron temperature of the ionized gas in K. The Lyman-continuum photon rates computed from uGMRT and GLOSTAR-D+Eff are shown in Table 6.3. There is good agreement between the Lyman-continuum photon rates computed from the two surveys, with the rate inferred from GLOSTAR-D+Eff being slightly larger than that from

uGMRT in a few sources. This confirms that both observations mostly trace the same optically thin diffuse emission. It also shows the efficiency of uGMRT in picking extended emission due to its central array comprising 14 antennas within a 1 sq km region.

Assuming that all the ionizing radiation comes from a single main sequence star, one can estimate the spectral type of the ionizing star. We have used the Lyman-continuum photon rate from the GLOSTAR-D+Eff observations and the formalism in Martins et al. (2005) for this estimation (7th column of Table 6.3). We have also determined the candidate ionizing stars in each H II using the NIR CCD and CMD (see Sect. 6.3.3), the locations of which are shown in Fig. 6.6 (see Fig. B.3 for the full sample). We see that the ionizing radiation comes from multiple stars for all H II regions in our sample, and we find reasonable agreement between the Lyman-continuum photon rate estimated from radio emission and the total rate from all candidate ionizing stars for our target sources (see Table 6.4). This important observation, along with the detection of diffuse radio emission, indicates that both the dense and extended emission have originated from the same group of candidate ionizing sources. Although it is well established that massive stars form in clusters, the presence of multiple candidate ionizing stars in our targets reaffirms this phenomenon.

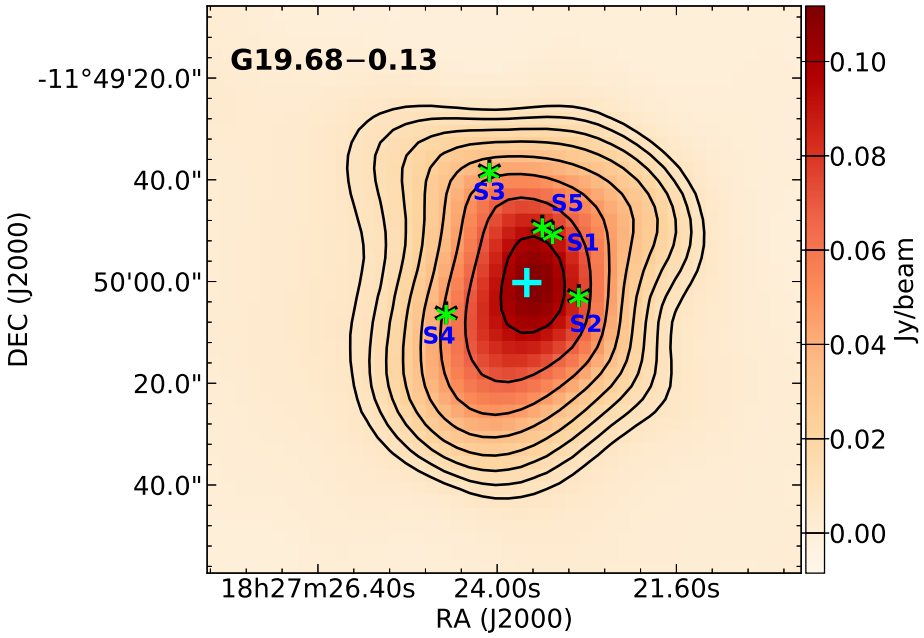

Figure 6.6: Locations of the candidate ionizing stars (labeled using an S__ format) are shown using green '*' signs for G19.68−0.13 (see Table 6.4 for details). The cyan '+' indicates the location of G19.68−0.13 reported in the THOR radio continuum catalog.

Table 6.4: Details of the candidate ionizing stars.

Source name	Spectral type[a]	No. of Stars[b]	Total $\log(N_{Ly})$[c] (lower limit)	Total $\log(N_{Ly})$[d] (upper limit)	$\log(N_{Ly})$ (D+Eff)
G19.68−0.13	$>$ O9	1	48.08	48.85	$48.85\ (^{+0.06}_{-0.07})$
	$>$ B3 but $<$ O9	4			
G20.99+0.09	$>$ B3 but $<$ O9	5	44.53	48.78	$47.55\ (^{+0.19}_{-0.36})$
	$\sim$ B3	2			
G22.76−0.48	$>$ O9	1	48.08	49.96	$48.63\ (^{0.05}_{-0.07})$
	$>$ B3 but $<$ O9	6			
	$\sim$ B3	1			
G24.47+0.49	$\sim$ O9	2	44.89	48.98	$49.12\ (^{0.04}_{-0.06})$
	$>$ B3 but $<$ O9	6			
	$\sim$ B3	10			
G25.69+0.03	$\sim$ O9	1	44.17	48.38	$49.06\ (^{0.05}_{-0.06})$
	$>$ B3 but $<$ O9	1			
	$\sim$ B3	2			
G27.49+0.19	$>$ B3 but $<$ O9	2	43.99	48.38	$47.87\ (^{0.13}_{-0.21})$
G28.30−0.39	$>$ B3 but $<$ O9	2	44.17	48.38	$48.80\ (^{0.06}_{-0.07})$
	$\sim$ B3	1			
G28.81+0.17	$>$ B3 but $<$ O9	4	44.38	48.68	$48.90\ (^{0.05}_{-0.06})$
	$\sim$ B3	1			

Note – a = spectral type range of the candidate ionizing stars including uncertainty in magnitudes and colors,
b = the total number of candidate ionizing stars in each spectral type category,
c = total Lyman-continuum photon rate calculated from all candidate stars considering them to be the latest spectral type in the category,
d = same as c but considering them to be the earliest spectral type in the category.

6.4.4 Infrared luminosity

As explained in Sect. 6.3.2, we have used data from the GLIMPSE, MIPSGAL, and Hi-GAL surveys to construct the SED of dust emission and modeled it using the DustEM package. The infrared luminosity (L_{IR}^{dust}) of the H II regions ranges from 6.92×10^3 to 1.95×10^5 $L_\odot$. This is consistent with the study by Cesaroni et al. (2015), who estimated the infrared luminosity (21 μm to 1.1 mm) of $\sim$ 200 young H II regions to range from 10^3 to 10^6 $L_\odot$. Similar to Sect. 6.4.3, we have determined the total luminosity from the ionizing stars and compared it with the luminosity determined by fitting the SED. We find the values to be consistent, reaffirming that the ionization in the H II regions is from a cluster of massive stars rather than a single star.

6.5 Notes on individual sources

G19.68−0.13 – We have detected arcmin scale extended emission surrounding the compact emission, which appears to be fragmented in the CORNISH radio continuum map at 5 GHz. These fragments altogether span an area of size $\approx$ 0.9 pc. A small velocity gradient (52–58 km s^{-1}) is also present from the east to west direction. Five candidate ionizing stars are also detected, with three stars, including one O9-type star, close to the reported location in Table 6.1.

G20.99+0.09 – This source exhibits diffuse emission that extends out to 1″–1.25″ from the center. The high-resolution map from uGMRT shows at least three compact emissions embedded within the extended emission. Moreover, the CORNISH 5 GHz map also shows similar morphology with their combined size $\approx$ 0.8 pc. The velocity field shows a gradient from the south-west to north-east direction. The data from the ^{12}*CO (3–2) High-Resolution Survey* (COHRS; Dempsey et al. 2013) of the molecular gas also shows similar velocity distribution, suggesting that the velocity field seen in the ionized gas is derived from that of the parent molecular cloud. We also detect several candidate ionizing stars within this H II region, indicating prior star formation activity within the parent cloud.

G22.76−0.48 – This source has a complex morphology with the extended emission reaching out to $\sim 4'$ in the GLOSTAR-D+Eff map. However, the extended emission is well within the boundary of far-infrared emission arising from the cold dust. The GLOSTAR-B radio continuum map shows a 7σ-level source near the location reported in the THOR radio continuum catalog. We have also detected a corresponding CORNISH source at this location. The spectral index is found to be positive (translates to an emission measure $\gtrsim$

10^7 pc cm^{-6}) along with the size $\leq$ 0.1 pc. These observations are consistent with this source being identified as a UC core. Moreover, the candidate ionizing stars are spread across multiple regions in the radio continuum maps, suggesting that high-mass star formation is happening in multiple groups within this H II region. An O4–O7 type star is responsible for the bulk of ionizing radiation (Messineo et al., 2014), with smaller contributions from multiple other B-type stars. We also detect a couple of young stellar objects (YSOs) near the south-west region of the radio continuum map, where no candidate ionizing stars are detected. The velocity field in this source is complex, with lower velocities being seen in the central region. Also, there is a small extension of ionized gas from the east towards the south of this H II region. However, We couldn't find any *APEX Telescope Large Area Survey of the Galaxy* (ATLASGAL; Schuller et al. 2009; Urquhart et al. 2018) clump candidates associated with this emission, whereas multiple ATLASGAL clumps (located at a similar distance) are associated with other parts of this H II region. We were also unable to find any candidate ionizing stars or YSOs in this region. This, coupled with the non-detection of any RRL emission, leads us to not consider this small extension as being associated with this source.

G24.47+0.49 – This H II region displays a fragmented shell morphology with significant extended emission detected in both uGMRT and GLOSTAR, with the UC core detected (listed in the UCHR catalog of Purcell et al. 2013) near the reported position in the THOR catalog. The GLOSTAR-B map also shows a 3σ-level source at this location matching with the criteria of a UC core. Moreover, the GLOSTAR-D and GLOSTAR-D+Eff maps show multiple bubbles surrounding the central shell-like structure, with a similar structure seen in the GLIMPSE survey at 8.0 μm. Jayasinghe et al. (2019) have identified three bubbles by fitting ellipses (major axis $\approx 1'$) to those structures, and the fragmented shell appears to have formed at the intersection point of these bubbles. However, since RRLs are not detected in these bubbles, we cannot determine whether they are directly associated with the UCHR or whether they trace an earlier generation of star formation. We have hence assumed the extent of this source to be equal to that detected using uGMRT (i.e., excluding the bubbles). The flux density measurements in the GLOSTAR-D and GLOSTAR-D+Eff maps are performed within this assumed area. We have identified two candidate O-type stars and a supergiant star (S39) using data from the 2MASS, UKIDSS, and *Panoramic Survey Telescope and Rapid Response System* (Pan-STARRS; Chambers et al. 2016) surveys. One of the candidate O-type stars is identified in one of the fragments, and a candidate B-type star is located near the center of the shell.

Table 6.5: Estimation of the fraction (f_d, f'_d, and f''_d) of Lyman-continuum photons that don't contribute to the ionization of hydrogen.

Source name	$\log(N_{Ly}^{RC})$	f_d (D+Eff)	$\log(N_{Ly}^{RC})$	f'_d (uGMRT)	$\log(N_{Ly}^{RC})$	f''_d (MAGPIS)	$\log(N_{Ly}^{IR})^*$
G19.68−0.13	$48.85\ ^{0.06}_{-0.07}$	0.12	$48.82\ ^{0.03}_{-0.03}$	0.19	$48.52\ ^{0.04}_{-0.05}$	0.59	48.91
G20.99+0.09	$47.55\ ^{0.19}_{-0.36}$	0.28	$47.54\ ^{0.20}_{-0.35}$	0.29	$47.25\ ^{0.19}_{-0.34}$	0.64	47.69
G22.76−0.48	$48.63\ ^{0.05}_{-0.07}$	0.13	$48.56\ ^{0.05}_{-0.06}$	0.26	$47.63\ ^{0.05}_{-0.06}$	0.91	48.69
G24.47+0.49	$49.12\ ^{0.04}_{-0.06}$	0.05	$48.98\ ^{0.04}_{-0.05}$	0.30	$48.76\ ^{0.04}_{-0.05}$	0.58	49.14
G25.69+0.03	$49.06\ ^{0.05}_{-0.06}$	0.09	$49.02\ ^{0.04}_{-0.04}$	0.17	$48.26\ ^{0.04}_{-0.05}$	0.85	49.10
G27.49+0.19	$47.87\ ^{0.13}_{-0.21}$	0.21	$47.87\ ^{0.13}_{-0.20}$	0.22	$47.34\ ^{0.12}_{-0.18}$	0.77	47.98
G28.30−0.39	$48.80\ ^{0.06}_{-0.07}$	0.23	$48.80\ ^{0.04}_{-0.05}$	0.24	$48.54\ ^{0.05}_{-0.07}$	0.58	48.92
G28.81+0.17	$48.90\ ^{0.05}_{-0.06}$	0.15	$48.89\ ^{0.04}_{-0.05}$	0.17	$48.68\ ^{0.05}_{-0.06}$	0.48	48.97

Note – RC = radio continuum,
IR = infrared,
f_d = fraction of Lyman-continuum photons not observed in the GLOSTAR-D+Eff radio continuum emission,
f'_d = fraction of Lyman-continuum photons not observed in the uGMRT radio continuum emission,
f''_d = fraction of Lyman-continuum photons not observed in the MAGPIS radio continuum emission,
$*$ = estimated considering the relation $f_d = 1 - (N_{Ly}^{RC}/N_{Ly}^{IR})$.

G25.69+0.03 – The extended emission shows a cometary morphology (especially in the high-resolution uGMRT map) with high-velocity ionized gas near the head of the comet. However, the UC core (identified as a 3σ-level source with size $\leq$ 0.1 pc from the GLOSTAR-B map along with a 3σ-level CORNISH counterpart) is located at the edge of the extended emission. Two candidate ionizing stars (one of which has spectral type O9) along with multiple other stars of late spectral types are also detected near the head using the 2MASS, *Naval Observatory Merged Astrometric Dataset* (NOMAD; Zacharias et al. 2004), and *The Guide Star Catalog* (Lasker et al., 2008) data. However, the Lyman-continuum photon rate estimated from the GLOSTAR-D+Eff radio continuum emission is higher than the total contribution from all detected candidate ionizing stars. This may suggest that a few more such stars are not detected in those surveys. The location of the ionizing stars significantly away from the UC core suggests that the UC core is not the source of extended emission for this region. The UC core may be a case of triggered star formation, although it requires further attention in future studies. Two more H II regions are also located towards the north. However, they are not related to our target.

G27.49+0.19 – From the radio continuum morphology, this H II region appears to be bipolar with two ionized bubbles towards the north and south direction. The ^{12}CO (3–2) molecular emission data from the COHRS survey shows emission surrounding these ionized bubbles. However, Li et al. (2018) have not detected any molecular outflow using the COHRS survey data. The compact emission is fragmented in the high-resolution map of CORNISH over a size of $\approx$ 0.2 pc. The signal-to-noise of the RRL map allows us to construct the velocity field only in the central region, with no apparent dichotomy between the northern and southern parts. Two candidate ionizing stars are seen near this central region, located at the meeting point of those two ionized bubbles.

G28.30−0.39 – This source shows a slight offset between the peak of the moment-0 map and that of the radio continuum. There are two peaks in the far-infrared maps from Hi-GAL containing two H II regions. However, the H II region within the westwards peak is located at a different distance (Urquhart et al., 2018). Hence, the corresponding radio contours are not shown here. Three candidate ionizing stars, along with a YSO (the YSO and a candidate ionizing star are located near the compact emission), are also detected in this H II region, although none of them are at the peak of the radio emission. The location of the UC core is identified from the GLOSTAR-B and CORNISH maps (3σ level), and it is located $18''$ away from the coordinates reported in the THOR radio continuum catalog. Also, this source is very weak in both the high-resolution maps. Moreover, the Lyman-continuum photon rate inferred from the GLOSTAR-D+Eff radio continuum emis-

sion is greater than the cumulative contribution from all candidate stars detected using near-infrared wavelengths (see Table 6.4). This could be due to the non-detection of the entire population of candidate ionizing stars within this H II region.

G28.81+0.17 – At radio wavelengths, the compact emission appears to be fragmented in the CORNISH map, spanning across an area of $\approx$ 1.2 pc. There are two candidate ionizing stars near the peak of the radio emission, with another three detected in the extended emission region. Like G28.30−0.39, the GLOSTAR-D+Eff Lyman-continuum photon rate is also greater than the total contribution from all candidate stars, which can be attributed to the non-detection of a few more candidate ionizing stars. The radio source towards the north is another H II region located at a similar distance to G28.81+0.17.

6.6 Discussion

6.6.1 Nature of the extended emission

Following the methods (described in Sect. 6.1) proposed by Kurtz et al. (1999), we have found that our target sources do not show any discontinuity in the continuum emission. Moreover, the velocity field of the RRLs shows a smooth distribution in all sources. However, as discussed in Sect. 6.5, the location of the UC core in G25.69+0.03 with respect to the diffuse extended emission makes it unlikely to be the source of the extended emission. Hence, we conclude that the extended emission is physically associated with the compact emission for the entire sample except for G25.69+0.03. Thus, the gas giving rise to the diffuse emission is mostly likely to originate from the same stars responsible for the compact emission. However, a caveat in this aspect is that the velocity field is determined at a resolution of 25″, at which scale any discontinuity between the velocity of compact and extended emission can be difficult to ascertain (due to spatial smoothing). However, due to the weak strength of the RRLs, it is not possible to image the line emission at high resolution.

6.6.2 Absorption of the Lyman-continuum photons by dust

We have estimated the Lyman-continuum photon rate required to explain the radio emission using eq. 6.1, tabulated in Table 6.3. Since the infrared emission results from radiation from the central stars that has been reprocessed by dust, one can obtain an independent estimate of the Lyman-continuum photon rate from the infrared luminosity. We use the following

Table 6.6: Comparison between the integrated flux densities of a few UCHRs common in the catalogs of WC89 and GLOSTAR-D survey.

Source name	l (deg)	b (deg)	RA (J2000)	DEC (J2000)	$S_{int}^{\rm WC}$ (Jy)	$S_{int}^{\rm GLOS}$ (Jy)
G05.89–0.39	5.885	–0.392	$18^{\rm h}00^{\rm m}30.38^{\rm s}$	$-24^\circ04'00.22''$	2.087	3.106 ± 0.155
G08.14+0.23	8.139	0.226	$18^{\rm h}03^{\rm m}00.74^{\rm s}$	$-21^\circ48'08.41''$	0.184	4.875 ± 0.244
G08.67–0.36	8.669	–0.356	$18^{\rm h}06^{\rm m}19.02^{\rm s}$	$-21^\circ37'32.35''$	0.630	1.202 ± 0.060
G10.62–0.38	10.623	–0.384	$18^{\rm h}10^{\rm m}28.67^{\rm s}$	$-19^\circ55'49.48''$	1.207	4.345 ± 0.217
G11.94–0.62	11.937	–0.616	$18^{\rm h}14^{\rm m}01.01^{\rm s}$	$-18^\circ53'25.01''$	0.879	1.424 ± 0.071
G19.07–0.28	19.071	–0.280	$18^{\rm h}26^{\rm m}46.40^{\rm s}$	$-12^\circ26'26.81''$	0.183	1.352 ± 0.068
G31.41+0.31	31.413	0.306	$18^{\rm h}47^{\rm m}34.57^{\rm s}$	$-01^\circ12'43.11''$	0.382	1.080 ± 0.054
G33.92+0.11	33.915	0.110	$18^{\rm h}52^{\rm m}50.23^{\rm s}$	$00^\circ55'29.35''$	0.357	1.112 ± 0.055
G33.50+0.20	33.498	0.194	$18^{\rm h}51^{\rm m}46.72^{\rm s}$	$00^\circ35'32.29''$	0.736	0.915 ± 0.046
G35.05−0.52	35.053	–0.518	$18^{\rm h}57^{\rm m}09.04^{\rm s}$	$01^\circ39'03.33''$	0.091	0.218 ± 0.012
G41.74+0.10	41.742	0.097	$19^{\rm h}07^{\rm m}15.50^{\rm s}$	$+07^\circ52'43.86''$	0.100	0.323 ± 0.016
G43.18–0.52	43.178	–0.518	$19^{\rm h}12^{\rm m}08.68^{\rm s}$	$+08^\circ52'08.72''$	0.326	0.729 ± 0.036
G45.12+0.13	45.122	0.132	$19^{\rm h}13^{\rm m}27.84^{\rm s}$	$+10^\circ53'36.71''$	1.167	5.545 ± 0.277
G45.48+0.13	45.478	0.130	$19^{\rm h}14^{\rm m}08.81^{\rm s}$	$+11^\circ12'27.96''$	0.344	1.623 ± 0.081

Note – $S_{int}^{\rm WC}$ = integrated flux densities from WC89,
$S_{int}^{\rm GLOS}$ = integrated flux densities from the GLOSTAR-D catalog.

equation from Inoue et al. (2001) for this purpose:

$$\left(\frac{L_{IR}^{dust}}{L_{\odot}}\right)\left(\frac{5.63\times10^{43}\,\mathrm{s}^{-1}}{N_{Ly}}\right)=\frac{1-0.28f}{f}, \tag{6.2}$$

where L_{IR}^{dust} is the integrated infrared luminosity from $8-1000$ μm, and f is the fraction of Lyman-continuum photons that contribute to the ionization of hydrogen. The values of f_d $(=1-f)$ for our sample are tabulated in Table 6.5.

As mentioned in Sect. 6.1, initial interferometric studies of UCHRs showed significantly larger Lyman-continuum photon rates from the infrared compared to what was deduced from radio emission (WC89; Kurtz et al. 1994). Since dust is an efficient absorber of high energy photons, which in turn reduces the number of photons that can contribute to the ionization of the surrounding gas, WC89 inferred that UCHRs have significant amounts of dust that can absorb up to 99% of the ionizing photons from the massive stars. Later studies suggested that a large fraction of the discrepancy in Lyman-continuum photon rates between radio and infrared studies was due to the presence of extended diffuse radio emission that was undetected in the early interferometer observations (e.g., Kurtz et al. 1999; de la Fuente et al. 2020). Using the GLOSTAR-D+Eff data, we find that the fraction of Lyman-continuum photons that are absorbed by dust ($f_d = 1 - f$) is within $5-28\%$ for our entire sample. These values are much smaller than the value of f_d in WC89. This clearly highlights the role of extended emission in resolving the discrepancy in the Lyman-continuum photon rate between infrared and high-angular resolution radio studies. High-resolution radio observations are only sensitive to the compact emission, while the infrared emission originates from a much larger region that encompasses the extended emission. Even in sources like G25.69+0.03, where the UCHR is probably not responsible for the extended emission, the Lyman-continuum photon rate inferred from infrared would be significantly overestimated, leading to an incorrect interpretation of f_d to be very high.

To further examine the role of sensitivity of interferometer observations, we have used data from *The Multi-Array Galactic Plane Imaging Survey* (MAGPIS; Helfand et al. 2006). The MAGPIS is a radio survey of the first Galactic quadrant at 6 cm and 20 cm using the VLA in its B, C, and D-configurations. This survey has an angular resolution of $\sim 6''$ and sensitivity of $1-2$ mJy at 20 cm. We have used the 20-cm radio continuum data with VLA in its B-configuration to calculate the Lyman-continuum photon rate, which in turn is used to calculate f'' using eq. 6.2. We have chosen the B-configuration of the VLA since the antennas are much more extended in this configuration, with much poorer sensitivity to extended emission compared to the GLOSTAR-D+Eff and uGMRT. As can be seen in

Table 6.5, the values of f''_d ($= 1 - f''$) are much larger than f_d and f'_d (going up to 91% for G22.76−0.48). This conclusively establishes the role of sensitivity to extended emission at radio wavelengths in inferring the fraction of Lyman-continuum photons absorbed by dust.

Although we have demonstrated the role of extended emission in significantly reducing the need for absorption of Lyman-continuum photons by dust in our sample, one also needs to address the question of the fraction of the overall population H II regions in the Galaxy that have compact cores surrounded by associated extended emission. While we reserve a systematic study for future work, a preliminary attempt can be made by comparing the integrated flux density of UCHRs reported by WC89 that were measured from observations at very high angular resolution ($\sim 0''.4$) with that of GLOSTAR-D which has much better sensitivity to extended emission. We find 14 UCHRs from the sample of WC89 that are present in the GLOSTAR-D survey catalog (Medina et al. 2019, 2024). We also find two UCHRs (G23.96−0.15 and G41.71+0.11) in WC89 that are not detected in both GLOSTAR-D and THOR radio continuum maps, although their flux densities are much higher than the sensitivity of both surveys. These could be artifacts in the radio continuum maps of WC89, as we see a few bright sources near their positions.

Considering the 14 sources that are common between WC89 and GLOSTAR-D, we find that all sources have larger integrated flux densities in the GLOSTAR-D, with the ratio of flux density in GLOSTAR-D to that in WC89 ranging from 1.25 to 26.5 (see Table 6.6). This is similar to the finding of Ellingsen et al. (2005), who found that 8 out of 10 sources had an integrated flux density larger than 10% when observed with the *Australia Telescope Compact Array* (ATCA) in the compact configuration (750D) compared to the more extended 6A configuration. Although the sample size is small, these results suggest that most H II regions have a larger flux density at radio wavelengths than what is detected in high-resolution observations, and the presence of extended emission around these regions is one of the likely solutions to resolve the mismatch between the Lyman-continuum photon rates estimated from the radio and infrared observations. There may also be examples such as G25.69+0.03, where the UCHR is not directly responsible for extended emission but lies at the edge of a larger H II region, wherein the Lyman-continuum photon rate inferred from infrared is significantly overestimated due to the infrared emission arising from the entire region.

6.6.3 The "age problem" of UCHRs

The number of UCHRs discovered by early radio surveys of such sources (WC89; Kurtz et al. 1994) was much greater than what was predicted in our Galaxy. This requires UCHRs to survive longer than their sound crossing times. This inconsistency is known as the "age problem" of UCHRs. One of the possible solutions to this problem may be the presence of extended emission surrounding the UC cores. The following example illustrates this.

Following WC89, the initial radius of a Strömgren sphere, r_i, will be ~ 0.051 pc for a typical UCHR (excited by an O6 star) without dust. Now, if dust absorbs 90% (i.e., f_d = 0.9) of the Lyman-continuum photons, then r_i will be reduced by a factor of $(1 - f_d)^{1/3} = 0.46$, resulting in an initial Strömgren radius of ~ 0.023 pc for f_d = 0.9 (WC89). Following the balance between photoionization and recombination, the UCHR continues to expand due to the pressure difference between the UCHR and the ambient neutral medium. When the expanding ionized gas achieves pressure equilibrium, the final Strömgren radius, r_f, reaches

$$r_f = r_i \left(\frac{2T_e}{T_0} \right)^{2/3}, \tag{6.3}$$

where T_e is the electron temperature of the ionized gas, and T_0 is the temperature of the neutral molecular gas (WC89). For a typical H II region, taking T_e = 10^4 K and T_0 = 25 K we will get r_f = 86 r_i. Thus, the UCHR will have a diameter of $\sim$ 2 pc at pressure equilibrium.

The time it takes for the UCHR to achieve r_f can be estimated using the expansion rate under the strong shock approximation (Dyson & Williams, 1980):

$$r_f(t) = r_i \left(1 + \frac{7\, c_i\, t}{4\, r_i} \right)^{4/7}, \tag{6.4}$$

where c_i is the sound speed ($\sim$ 10 km s^{-1}) inside the ionized medium. Now, following eq. 6.4, the expanding UCHR will reach a size of 0.1 pc (which is the limit of a UHCR as per the classification of WC89; Kurtz et al. 1994) in a timescale of 1.5×10^4 years. Since the main sequence lifetime of an O6 star is 2.4×10^6 years (Maeder & Meynet, 1987), a H II region will be in its UC phase for roughly 0.6% of its entire lifetime. However, the observations of Kim & Koo (2001); Hoare et al. (2007); de la Fuente et al. (2020) show a much larger number of detections of UCHRs than what is anticipated given its lifetime in the UC phase.

However, observations show that H II regions have hierarchical density structures with

compact emission co-existing with diffuse extended emission. While the exact mechanism for the formation of a H II region with hierarchical structure is not clear (see, for example, Fig. 8 of Kim & Koo 2001), it is clear that simple analytical models such as that described above cannot be used to determine the age of H II regions since the models assume the density to be uniform within the H II region. If the extended emission is produced by leakage of ionizing photons selectively through lower-density regions within the hierarchical structure, the lifetime of the UCHR can be significantly larger than what is predicted by eq. 6.4 using an r_f of 0.1 pc. Thus, the co-existence of extended and compact radio emission could resolve the age problem of UCHRs, although a definitive conclusion in this regard requires simulations of an expanding H II region in a medium with a hierarchical density structure.

6.6.4 Characteristics of the extended emission

As discussed in Sect. 6.4.1.2, the extended emission significantly influences the physical properties of H II regions, including electron density, emission measure, and related characteristics, particularly on larger spatial scales. Accordingly, we have estimated the electron densities, n_e, for the H II regions within our sample using the following equation provided by Schmiedeke et al. (2016):

$$\left(\frac{n_e}{\mathrm{cm^{-3}}}\right) = 2.576 \times 10^6 \left(\frac{F_\nu}{\mathrm{Jy}}\right)^{0.5} \left(\frac{T_e}{\mathrm{K}}\right)^{0.175} \left(\frac{\nu}{\mathrm{GHz}}\right)^{0.05} \left(\frac{\theta}{\mathrm{arcsec}}\right)^{-1.5} \left(\frac{d}{\mathrm{pc}}\right)^{-0.5}. \quad (6.5)$$

where F_ν is the flux density of the H II region, T_e is the electron temperature, ν is the frequency, θ is the angular diameter of the H II region, and d is the distance to the source. Now considering the values of these parameters (for the GLOSTAR-D maps) from Table 6.1 and Table 6.3, we have found that the n_e of our sample varies within the range of $\simeq$ 40 to $\simeq$ 260 cm^{-3} (see Table 6.7), with a median value of 97 cm^{-3}.

In a related study, Goldsmith et al. (2015) derived n_e for 149 positions within the Galactic Plane through surveys employing the fine structure lines of ionized nitrogen, [N II]. Their findings revealed n_e values ranging from approximately 10 to 100 cm^{-3}, with a mean value of 29 cm^{-3}. These values were significantly higher than those typically associated with the standard warm ionized medium, which has electron densities $\sim$ 0.1 cm^{-3}, yet substantially lower than those characteristic of compact and ultracompact H II regions ($\sim$ 10^3 cm^{-3} and $\sim$ 10^4 cm^{-3}, respectively; Kurtz 2005). To account for these intermediate n_e values, the authors proposed that the warm ionized medium may contain multiple-density

Table 6.7: Derived values of electron densities for the H II regions in our samples

Source name	θ (arcsec)	n_e (cm^{-3})
G19.68−0.13	104	84
G20.99+0.09	168	119
G22.76−0.48	212	52
G24.47+0.49	116*	266
G25.69+0.03	174	39
G27.49+0.19	180	103
G28.30−0.39	116	91
G28.81+0.17	114	124

Note – $*$ = As discussed in Sect. 6.5, we have assumed the extent of this source to be equal to that detected using uGMRT (i.e., excluding the bubbles).

components or the H II regions could include physically associated low-density extended envelopes. Although our median n_e value is at least three times greater than the mean n_e value reported in Goldsmith et al. (2015), there is a significant overlap between our obtained electron densities and those derived by Goldsmith et al. (2015). In a similar context, Anantharamaiah (1986) conducted a radio survey (H272α line emission at 325 MHz) of 29 well-known H II regions by using the *Ooty Radio Telescope* and estimated n_e to be $\sim$ 10 cm^{-3}, which is much lower than those derived by us. However, the linear sizes derived by Anantharamaiah (1986) range from 30 to 300 pc, which are significantly larger than those of our H II regions. This suggests that their survey traced more diffuse ionized gas compared to ours.

Thus, the derived values of n_e in this study highlight the need for future surveys focusing on the extended envelopes of a larger sample of Galactic H II regions. Such surveys would provide more accurate estimates of their physical properties, particularly electron densities. Additionally, these studies could offer insights into whether the warm ionized medium of the Galactic ISM comprises multiple density components while also advancing our understanding of the interaction between the low-density extended envelopes of H II regions and warm ionized medium of our Galaxy.

6.7 Summary

In this chapter, we investigate the role of extended emission surrounding H II regions in resolving the discrepancies between the Lyman-continuum photon rates derived from the

radio and infrared emission. For this purpose, we have used radio observations of eight compact and ultracompact H II regions using the uGMRT and data from the GLOSTAR survey along with complementary infrared data from the Hi-GAL, MIPSGAL, GLIMPSE, 2MASS, and UKIDSS surveys. We have listed our main findings below.

- We have detected arcmin-scale extended continuum emission surrounding all of our target H II regions. These detections significantly boost the rate of Lyman-continuum photons at radio wavelengths compared to what would have been detected using high angular resolution observations. However, we find one example where we find the UCHR is located at the edge of the extended emission, where the Lyman-continuum photon rate may be over estimated.

- Besides radio continuum, we have also detected RRLs toward our targets. The RRL velocity maps show continuous velocity distributions across the target regions, also indicating a physical association between the compact core(s) and extended emission. The line widths of the RRLs (24 to 30 km s^{-1}) are in agreement with what is expected for compact and ultracompact H II regions.

- The in-band (GLOSTAR-D) and inter-band (uGMRT and GLOSTAR-D) spectral indices of the sources of our target sample are close to –0.1, which indicates the radio emission is optically thin. However, this is in contrast to the spectral indices of the compact emission, which is consistent with optically thick thermal emission. Thus, the extended emission dominates the properties of H II regions at large scales.

- Near-infrared data from the 2MASS and UKIDSS surveys reveal multiple candidate ionizing stars within the target sources. We find that the Lyman-continuum photon rate estimated from the radio emission and the total rate from all candidate ionizing stars are within reasonable agreement. This indicates that the emissions from dense and diffuse components have originated from the same group of ionizing sources. This discovery also showcases the formation of massive stars in clusters.

- The inclusion of extended emission indicates that a much smaller fraction of Lyman-continuum photons is absorbed by dust than what would be inferred from just the dense emission. In addition to reducing the estimated quantity of dust in H II regions, the presence of extended emission may resolve the "age problem" of the UCHRs.

The results of our work highlight the importance of sensitivity to detect extended emission, which is one of the key highlights of the full GLOSTAR survey.

Chapter 7

Conclusions and future work

7.1 Conclusions

This thesis has presented a detailed multi-wavelength study of high-mass star formation, focusing on the evolution of Galactic H II regions and the role of extended emission in resolving key problems related to ionizing photon rates. We have put effort into addressing a few long-standing problems associated with the Galactic H II regions by integrating data across a broad spectrum of wavelengths, from radio to infrared.

In Chapter 5, we focus on a specific case study: the UCHR, G18.15. Through high-resolution radio data from the uGMRT, we detected multiple radio continuum peaks within G18.15, along with RRLs, that revealed two distinct velocity components. This, along with evidence from molecular line data, suggests that G18.15 likely formed as a result of a cloud-cloud collision event approximately 0.3 Myr ago. This finding is supported by the detection of 'broad-bridge' features in position-velocity diagrams, a hallmark of cloud-cloud collision scenarios. Furthermore, the identification of two O9 stars and 30 YSOs toward this region indicates ongoing massive star cluster formation. Despite the detection of these point sources, the high extinction and extended mid-infrared emission suggest the existence of an undetected population of massive stars, further highlighting the complexity of this region.

The results from G18.15 provide crucial insights into the formation mechanisms of massive stars, particularly in environments that are influenced by external triggering processes such as cloud-cloud collisions. This study underscores the need for detailed, high-resolution studies of individual H II regions, as each region can offer unique clues about different pathways through which massive stars can form.

In Chapter 6, we have analyzed a broader sample of eight CHRs and UCHRs. The primary goal of this study was to investigate the role of extended radio continuum emission

in resolving inconsistencies between the ionizing photon rates inferred from radio and infrared observations. Historically, radio observations have often reported significantly lower ionizing photon rates compared to those derived from infrared data, with previous studies attributing this discrepancy to high dust absorption within the ionized regions. However, our observations have shown that extended emission, which is often undetected in high-resolution interferometric data due to limitations in sensitivity to larger spatial scales, plays a crucial role in bridging this gap.

Using a combination of uGMRT and GLOSTAR radio data, along with complementary infrared data from the Hi-GAL, MIPSGAL, and GLIMPSE surveys, we successfully detected arcmin-scale extended radio emission surrounding all eight H II regions in our sample. This extended emission significantly boosts the ionizing photon rates measured at radio wavelengths, bringing them into much closer agreement (5–28%) with the photon rates inferred from infrared data. In addition to the radio continuum, we also detected RRLs, which showed continuous velocity distributions across the target regions, which confirms the physical association between the compact cores and the extended emission. This finding is particularly important, as it indicates that the dense cores and their surrounding diffuse ionized envelopes likely share the same ionizing sources, further corroborated by the identification of multiple candidate ionizing stars within each region.

One of the key findings from this chapter is that the inclusion of extended emission suggests a much lower fraction of ionizing photons are absorbed by dust than previously thought. This has significant implications for our understanding of the evolution of CHRs and UCHRs, particularly with regard to the so-called "age problem." The age problem refers to the apparent mismatch between the inferred ages of UCHRs and the lifetimes of their ionizing stars, with previous estimates suggesting that these regions should dissipate much more quickly than observed. Our results suggest that much of the ionizing radiation from these regions is, in fact, escaping into their surroundings, which could allow them to persist for longer periods than initially thought. This extended emission, therefore, offers a potential solution to the age problem by accounting for the missing ionizing flux.

This study also investigates the electron densities (n_e) of Galactic H II regions, comparing results with previous surveys. Our estimates show that the values of n_e are between $\simeq 40$ and $\simeq 260$ cm^{-3} with a median value of 97 cm^{-3}. Whereas Goldsmith et al. (2015) found n_e values within the 10–100 cm^{-3} range with a mean value of 29 cm^{-3} in the Galactic Plane using [N II] fine structure lines. Moreover, Anantharamaiah (1986) detected H272α emission towards multiple lines of sights piercing through the Galactic plane with an even lower $n_e \sim 10$ cm^{-3}. These lower n_e values may be attributed to the larger linear scales

surveyed in these previous observations, and they highlight the requirement of future observations with a large sample of Galactic H II regions to better constrain the origin of such low-density ionized emission.

Another important outcome of our study is the discovery of spectral index variations between the compact and extended components of the H II regions. The in-band and inter-band spectral indices of the extended emission are close to -0.1, indicating optically thin radio emission, while the compact cores exhibit optically thick thermal emission. This difference highlights the dominant role of extended emission in shaping the observed properties of H II regions at larger scales that further emphasizes the importance of including these diffuse components in any comprehensive analysis of massive star-forming regions.

Our findings also underscore the clustered nature of massive star formation. The detection of multiple ionizing stars within each region supports the idea that massive stars form in groups rather than in isolation. This has important implications for the dynamics of star-forming regions and the feedback processes that shape their evolution. The radiation, winds, and outflows from these stars interact with their surrounding environments, contributing to the overall structure and dynamics of the ISM.

The results presented in this thesis not only advance our understanding of massive star formation but also contribute to broader questions about the role of massive stars in galactic evolution, the lifecycle of the ISM, and the processes that regulate star formation in galaxies. By resolving the discrepancies in ionizing photon rates and highlighting the importance of extended emission, this work provides a foundation for future studies that will further unravel the complex interplay between massive stars and their environments.

7.2 Future work

The H II regions studied in this thesis work have extended emission associated with them, showcasing the presence of hierarchical density structures. Although the exact mechanisms for the formation of extended emission are not clear, a simulation by Wood et al. (2005) indicates that the extended emission may have been produced by the leakage of ionizing photons selectively through lower-density regions within the hierarchical structures. On the other hand, a work by Williams et al. (2000) suggests that the hierarchical nature of molecular clouds leads to the clumpy, non-uniform density structures seen in H II regions as ionizing photons permeate these clouds. Despite the uncertainty in their formation mechanism, as explained in chapter 3, the H II regions, along with their extended emission, expand into the neutral medium around them. However, this expansion cannot last forever,

and at one point, the pressure balance will be achieved, confining the extended emission within a finite region. Otherwise, the extended emission will be so diluted that it will go beyond the detection limits of the radio interferometers. Clearly, this is not the case for the H II regions in our sample. Hence, in continuation of the work done in this thesis, we plan to further study the mechanisms that confine the extended emission in the future. Here, we furnish some initial results from this study.

Before the creation of H II regions, molecular hydrogen (H_2) begins to dissociate into atomic hydrogen (H I) when the temperature exceeds several thousand Kelvin due to the formation of protostars. The H I is further ionized by UV photons emanating from the massive stars in their main-sequence phase. This process creates a cavity within the distribution of atomic hydrogen, as the abundance of H I decreases with time due to the ionization. This is followed by the two expansion phases (first ionization-driven and second pressure-driven) of the H II regions, out of which the pressure-driven phase sweeps up the neutral material outward. Subsequently, the expanding ionized gas reaches up to the inner wall of the cavity formed within the neutral gas (mostly H I) and obtains pressure equilibrium, which prevents the extended ionized gas from further expansion.

We also expect to observe similar phenomena in our sample H II regions, which ultimately will lead to the confinement of the extended ionized emission. For this purpose, we have generated the column density maps of atomic hydrogen toward our targets by utilizing the H I line emission data from the *VLA Galactic Plane Survey* (VGPS; Stil et al. 2006). We have followed the methodologies described in Saha et al. (2018) to create the column density maps, and the steps taken are briefly described here.

Considering an isothermal cloud of atomic hydrogen hosting a target H II region, its H I column density N(H I) may be written as (Kulkarni & Heiles, 1988; Dickey & Lockman, 1990):

$$N(\mathrm{H\,I}) = 1.823 \times 10^{18}\ \mathrm{cm}^{-2} \int T_s\, \tau\, dV, \tag{7.1}$$

where the spin temperature, T_s, is in K, the optical depth τ can be inferred from absorption studies towards suitable continuum sources, the velocity interval dV is in km s^{-1}, and the integration is taken over the velocity range that only includes the cloud of interest, as the line of sight toward our target also includes multiple Galactic atomic hydrogen clouds at different velocities. We can also derive T_s by combining the brightness temperature, T_B and τ by using the following expression

$$T_B = T_s\,[1 - \exp(-\tau)], \tag{7.2}$$

where T_B can be measured from the H I line emission studies. Now, using eq. 7.2, we can rewrite eq. 7.1 as

$$N(\mathrm{H\,I}) = 1.823 \times 10^{18}\ \mathrm{cm}^{-2} \int \frac{\tau\, T_B}{[1 - \exp(-\tau)]}\, dV. \tag{7.3}$$

For the optically thin limit ($\tau \ll 1$), this equation can be further simplified into

$$N(\mathrm{H\,I}) = 1.823 \times 10^{18}\ \mathrm{cm}^{-2} \int T_B\, dV. \tag{7.4}$$

Thus, under the isothermal and optically thin assumption, one can use eq. 7.4 to estimate the atomic hydrogen column density of a cloud from its emission studies.

Fig. 7.1 shows the atomic hydrogen column density map for one of our target sources.

From this figure, it is apparent that the ionizing photons have carved out a cavity within the H I column density, and the 3σ-level radio continuum emission (extended) is confined by the inner wall of this cavity. Other sources of our sample also show a similar type of behavior (see Fig. B.4). However, for the sources, G24.47+0.48 and G27.49+0.19, the observed (radio) bubble-like structures are not confined by the cavities within the H I column density. As mentioned in sect. 6.5, we have not detected any RRL emission toward these bubbles, questioning their direct association with the respective H II regions. Thus, the results from our initial H I study may indicate that these bubbles are actually not associated with G24.47+0.48 and G27.49+0.19 H II regions.

In sum, from our initial analysis, we found a mechanism that could potentially halt the expansion of the extended emission. However, a more detailed analysis is required in terms of the value of spin temperature used (eq. 7.2) and other parameters that go into the determination of N(H I) before commenting further on this. In this preliminary analysis, we have assumed the clouds to be optically thin following Dickey & Lockman (1990), where the authors have argued that if the peak value of T_B is only a few tens of Kelvin or less, which is the case for our H I clouds, the optically thin assumption is acceptable. Nonetheless, for a full estimation of N(H I), one has to consider the values of τ derived from absorption studies. Furthermore, a study of the pressure difference between the H I gas and the edge of the H II region can also be carried out to validate the pressure equilibrium scenario.

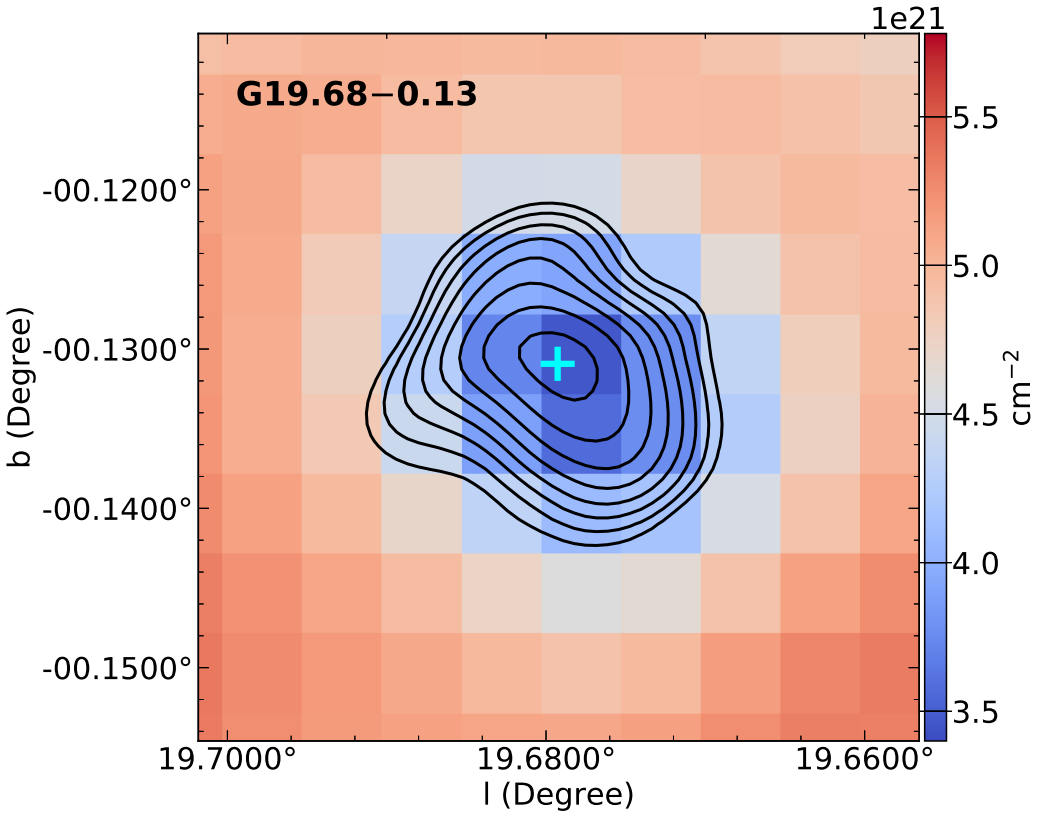

Figure 7.1: Atomic hydrogen (H I) column density map of G19.68−0.13 overlaid with the radio contours from the GLOSTAR-D continuum map in black. The contours have started at the 3σ-level flux and have increased in steps of $\sqrt{2}$. The location of G19.68−0.13 reported in the THOR radio continuum catalog is shown using a cyan '+' sign. Blue indicates regions with lower column density, whereas red indicates the vice versa.

Bibliography

Altenhoff, W. J. 1961, Veroeffentlichungen des Astronomisches Institute der Universitaet Bonn, 59, 1

Anantharamaiah, K. R. 1986, Journal of Astrophysics and Astronomy, 7, 131

Anathpindika, S. V. 2010, MNRAS, 405, 1431

André, P. 2002, in EAS Publications Series, Vol. 3, EAS Publications Series, ed. J. Bouvier & J.-P. Zahn, 1–38

André, P. 2015, in Encyclopedia of Astrobiology, ed. M. Gargaud, W. M. Irvine, R. Amils, I. Cleaves, Henderson James (Jim), D. L. Pinti, J. C. Quintanilla, D. Rouan, T. Spohn, S. Tirard, & M. Viso, 2308–2313

Aniano, G., Draine, B. T., Gordon, K. D., & Sandstrom, K. 2011, PASP, 123, 1218

Ao, Y., Yang, J., Tatematsu, K., et al. 2018, AJ, 156, 210

Arce, H. G., & Sargent, A. I. 2006, ApJ, 646, 1070

Baug, T., Dewangan, L. K., Ojha, D. K., & Ninan, J. P. 2016, ApJ, 833, 85

Baumgardt, H., & Klessen, R. S. 2011, MNRAS, 413, 1810

Beltrán, M. T., & Rivilla, V. M. 2018, in Astronomical Society of the Pacific Conference Series, Vol. 517, Science with a Next Generation Very Large Array, ed. E. Murphy, 249

Benjamin, R. A., Churchwell, E., Babler, B. L., et al. 2003, PASP, 115, 953

Bertoldi, F., & McKee, C. F. 1992, ApJ, 395, 140

Bessell, M. S., & Brett, J. M. 1988, PASP, 100, 1134

Beuther, H., Churchwell, E. B., McKee, C. F., & Tan, J. C. 2007a, in Protostars and Planets V, ed. B. Reipurth, D. Jewitt, & K. Keil, 165

Beuther, H., Leurini, S., Schilke, P., et al. 2007b, A&A, 466, 1065

Beuther, H., Linz, H., Henning, T., Feng, S., & Teague, R. 2017, A&A, 605, A61

Beuther, H., Sridharan, T. K., & Saito, M. 2005, ApJ, 634, L185

Beuther, H., Zhang, Q., Sridharan, T. K., Lee, C. F., & Zapata, L. A. 2006, A&A, 454, 221

Beuther, H., Bihr, S., Rugel, M., et al. 2016, A&A, 595, A32

Bohlin, R. C., Savage, B. D., & Drake, J. F. 1978, ApJ, 224, 132

Bonnell, I. A. 2002, in Astronomical Society of the Pacific Conference Series, Vol. 267, Hot Star Workshop III: The Earliest Phases of Massive Star Birth, ed. P. Crowther, 193

Bonnell, I. A., & Bate, M. R. 2006, MNRAS, 370, 488

Bonnell, I. A., Bate, M. R., & Zinnecker, H. 1998, MNRAS, 298, 93

Bonnell, I. A., Clarke, C. J., Bate, M. R., & Pringle, J. E. 2001, MNRAS, 324, 573

Bradley, L., Sipőcz, B., Robitaille, T., et al. 2023, astropy/photutils: 1.8.0, 1.8.0, Zenodo

Brand, J., & Wouterloot, J. G. A. 1995, A&A, 303, 851

Briggs, D. S. 1995, in American Astronomical Society Meeting Abstracts, Vol. 187, American Astronomical Society Meeting Abstracts, 112.02

Brocklehurst, M., & Seaton, M. J. 1972, MNRAS, 157, 179

Bronfman, L., Alvarez, H., Cohen, R. S., & Thaddeus, P. 1989, ApJS, 71, 481

Brown, R. L., Lockman, F. J., & Knapp, G. R. 1978, ARA&A, 16, 445

Brunthaler, A., Menten, K. M., Dzib, S. A., et al. 2021, A&A, 651, A85

Brussaard, P. J., & van de Hulst, H. C. 1962, Reviews of Modern Physics, 34, 507

Carey, S. J., Noriega-Crespo, A., Mizuno, D. R., et al. 2009, PASP, 121, 76

Carpenter, J. M. 2001, AJ, 121, 2851

Carpenter, J. M., Snell, R. L., & Schloerb, F. P. 1990, ApJ, 362, 147

Castor, J., McCray, R., & Weaver, R. 1975, ApJ, 200, L107

Cesaroni, R. 2005, in IAU Symposium, Vol. 227, Massive Star Birth: A Crossroads of Astrophysics, ed. R. Cesaroni, M. Felli, E. Churchwell, & M. Walmsley, 59–69

Cesaroni, R., Pestalozzi, M., Beltrán, M. T., et al. 2015, A&A, 579, A71

Chambers, K. C., Magnier, E. A., Metcalfe, N., et al. 2016, arXiv e-prints, arXiv:1612.05560

Churchwell, E. 2002, ARA&A, 40, 27

Churchwell, E., Povich, M. S., Allen, D., et al. 2006, ApJ, 649, 759

Compiègne, M., Verstraete, L., Jones, A., et al. 2011, A&A, 525, A103

Condon, J. J., Cotton, W. D., Greisen, E. W., et al. 1998, AJ, 115, 1693

Corradi, R. L. M., Aznar, R., & Mampaso, A. 1998, MNRAS, 297, 617

Cox, A. N. 2000, Allen's astrophysical quantities

Crowther, P. A., Schnurr, O., Hirschi, R., et al. 2010, MNRAS, 408, 731

de la Fuente, E., Porras, A., Trinidad, M. A., et al. 2020, MNRAS, 492, 895

Deharveng, L., Schuller, F., Anderson, L. D., et al. 2010, A&A, 523, A6

Dempsey, J. T., Thomas, H. S., & Currie, M. J. 2013, ApJS, 209, 8

Desert, F. X., Boulanger, F., & Shore, S. N. 1986, A&A, 160, 295

Dewangan, L. K., & Ojha, D. K. 2017, ApJ, 849, 65

Dewangan, L. K., Sano, H., Enokiya, R., et al. 2019, ApJ, 878, 26

Dickel, J. R., Dickel, H. R., & Wilson, W. J. 1978, ApJ, 223, 840

Dickey, J. M., & Lockman, F. J. 1990, ARA&A, 28, 215, doi: 10.1146/annurev.aa.28.090190.001243

Dobbs, C. L., Krumholz, M. R., Ballesteros-Paredes, J., et al. 2014, in Protostars and Planets VI, ed. H. Beuther, R. S. Klessen, C. P. Dullemond, & T. Henning, 3–26

Dokara, R., Gong, Y., Reich, W., et al. 2023, A&A, 671, A145

Downes, D., & Rinehart, R. 1966, ApJ, 144, 937

Dyson, J. E., & Williams, D. A. 1980, Physics of the interstellar medium

Dzib, S. A., Yang, A. Y., Urquhart, J. S., et al. 2023, A&A, 670, A9

Edgar, R., & Clarke, C. 2004, MNRAS, 349, 678

Ellingsen, S. P. 2004, in IAU Symposium, Vol. 221, Star Formation at High Angular Resolution, ed. M. G. Burton, R. Jayawardhana, & T. L. Bourke, 133

Ellingsen, S. P., Shabala, S. S., & Kurtz, S. E. 2005, MNRAS, 357, 1003

Elmegreen, B. G. 1994, ApJ, 433, 39

Fatuzzo, M., & Adams, F. C. 2002, ApJ, 570, 210

Fazio, G. G., Hora, J. L., Allen, L. E., et al. 2004, ApJS, 154, 10

Ferrière, K. M. 2001, Reviews of Modern Physics, 73, 1031

Figer, D. F. 2005, Nature, 434, 192

Franco, J., Tenorio-Tagle, G., & Bodenheimer, P. 1990, ApJ, 349, 126

Fukui, Y., & Kawamura, A. 2010, ARA&A, 48, 547

Fukui, Y., Ohama, A., Hanaoka, N., et al. 2014, ApJ, 780, 36

Fukui, Y., Torii, K., Ohama, A., et al. 2016, ApJ, 820, 26

Furukawa, N., Dawson, J. R., Ohama, A., et al. 2009, ApJ, 696, L115

Garay, G., & Lizano, S. 1999, PASP, 111, 1049

Goldberg, L. 1966, ApJ, 144, 1225

Goldsmith, P. F., Yıldız, U. A., Langer, W. D., & Pineda, J. L. 2015, ApJ, 814, 133

Griffin, M. J., Abergel, A., Abreu, A., et al. 2010, A&A, 518, L3

Gupta, Y., Ajithkumar, B., Kale, H., et al. 2017, Current Science, 707

Gutermuth, R. A., Myers, P. C., Megeath, S. T., et al. 2008, ApJ, 674, 336

Güver, T., & Özel, F. 2009, MNRAS, 400, 2050

Habe, A., & Ohta, K. 1992, PASJ, 44, 203

Habing, H. J., & Israel, F. P. 1979, ARA&A, 17, 345

Hartmann, L., Megeath, S. T., Allen, L., et al. 2005, ApJ, 629, 881

Haworth, T. J., Tasker, E. J., Fukui, Y., et al. 2015, MNRAS, 450, 10

Helfand, D. J., Becker, R. H., White, R. L., Fallon, A., & Tuttle, S. 2006, AJ, 131, 2525

Hennebelle, P., Pérault, M., Teyssier, D., & Ganesh, S. 2001, A&A, 365, 598

Heyer, M. H., Carpenter, J. M., & Snell, R. L. 2001, ApJ, 551, 852

Hoare, M. G., Kurtz, S. E., Lizano, S., Keto, E., & Hofner, P. 2007, in Protostars and Planets V, ed. B. Reipurth, D. Jewitt, & K. Keil, 181

Hoare, M. G., Purcell, C. R., Churchwell, E. B., et al. 2012, PASP, 124, 939

Inoue, A. K., Hirashita, H., & Kamaya, H. 2001, ApJ, 555, 613

Inoue, T., & Fukui, Y. 2013, ApJ, 774, L31

Issac, N., Tej, A., Liu, T., & Wu, Y. 2020, MNRAS, 499, 3620

Jayasinghe, T., Dixon, D., Povich, M. S., et al. 2019, MNRAS, 488, 1141

Jolly, J.-B., Knudsen, K. K., & Stanley, F. 2020, MNRAS, 499, 3992

Kennicutt, R. C., & Evans, N. J. 2012, ARA&A, 50, 531

Kessler, M. F., Steinz, J. A., Anderegg, M. E., et al. 1996, A&A, 315, L27

Keto, E. 2002, ApJ, 580, 980

Keto, E., & Wood, K. 2006, ApJ, 637, 850

Keto, E., Zhang, Q., & Kurtz, S. 2008, ApJ, 672, 423

Khan, S., Rugel, M. R., Brunthaler, A., et al. 2024, A&A, 689, A81

Kim, K.-T., & Koo, B.-C. 2001, ApJ, 549, 979

Kim, K. T., & Koo, B. C. 2002, in Astronomical Society of the Pacific Conference Series, Vol. 267, Hot Star Workshop III: The Earliest Phases of Massive Star Birth, ed. P. Crowther, 373

Kratter, K. M., & Matzner, C. D. 2006, MNRAS, 373, 1563

Kroupa, P. 2001, MNRAS, 322, 231

Krumholz, M. R., Klein, R. I., McKee, C. F., Offner, S. S. R., & Cunningham, A. J. 2009, Science, 323, 754

Kulkarni, S. R., & Heiles, C. 1988, in Galactic and Extragalactic Radio Astronomy, ed. K. I. Kellermann & G. L. Verschuur, 95–153

Kurtz, S. 2005, in Massive Star Birth: A Crossroads of Astrophysics, ed. R. Cesaroni, M. Felli, E. Churchwell, & M. Walmsley, Vol. 227, 111–119

Kurtz, S. 2005, Proceedings of the International Astronomical Union, 1, 47–56

Kurtz, S., Cesaroni, R., Churchwell, E., Hofner, P., & Walmsley, C. M. 2000, in Protostars and Planets IV, ed. V. Mannings, A. P. Boss, & S. S. Russell, 299–326

Kurtz, S., Churchwell, E., & Wood, D. O. S. 1994, ApJS, 91, 659

Kurtz, S. E., Watson, A. M., Hofner, P., & Otte, B. 1999, ApJ, 514, 232

Lada, C. J., & Lada, E. A. 2003, ARA&A, 41, 57

Lada, C. J., & Shu, F. H. 1990, Science, 248, 564

Larson, R. B. 2003, Reports on Progress in Physics, 66, 1651

Lasker, B. M., Lattanzi, M. G., McLean, B. J., et al. 2008, AJ, 136, 735

Lawrence, A., Warren, S. J., Almaini, O., et al. 2007, MNRAS, 379, 1599

Li, P. S., & Klein, R. I. 2019, MNRAS, 485, 4509

Li, Q., Zhou, J., Esimbek, J., et al. 2018, ApJ, 867, 167

Liu, T., Li, P. S., Juvela, M., et al. 2018, ApJ, 859, 151

Lockman, F. J. 1989, ApJS, 71, 469

Lockman, F. J., & Brown, R. L. 1975, ApJ, 201, 134

Loren, R. B. 1976, ApJ, 209, 466

—. 1977, ApJ, 215, 129

Luna, A., Bronfman, L., Carrasco, L., & May, J. 2006, ApJ, 641, 938

Mac Low, M.-M., van Buren, D., Wood, D. O. S., & Churchwell, E. 1991, ApJ, 369, 395

Maeder, A., & Meynet, G. 1987, A&A, 182, 243

Magnani, L., Blitz, L., & Mundy, L. 1985, ApJ, 295, 402

Makovoz, D., & Marleau, F. 2005, Publications of the Astronomical Society of the Pacific, 117, 1113

Marti, J., Rodriguez, L. F., & Reipurth, B. 1993, ApJ, 416, 208

Martins, F., Schaerer, D., & Hillier, D. J. 2005, A&A, 436, 1049

Massi, F., Weiss, A., Elia, D., et al. 2019, A&A, 628, A110

McKee, C. F., & Ostriker, E. C. 2007, ARA&A, 45, 565

McKee, C. F., & Ostriker, J. P. 1977, ApJ, 218, 148

McKee, C. F., & Tan, J. C. 2002, Nature, 416, 59

—. 2003, ApJ, 585, 850

McMullin, J. P., Waters, B., Schiebel, D., Young, W., & Golap, K. 2007, in Astronomical Society of the Pacific Conference Series, Vol. 376, Astronomical Data Analysis Software and Systems XVI, ed. R. A. Shaw, F. Hill, & D. J. Bell, 127

Medina, S. N. X., Urquhart, J. S., Dzib, S. A., et al. 2019, A&A, 627, A175

Medina, S. N. X., Dzib, S. A., Urquhart, J. S., et al. 2024, A&A, 689, A196

Messineo, M., Menten, K. M., Figer, D. F., et al. 2014, A&A, 569, A20

Meyer, M. R., Calvet, N., & Hillenbrand, L. A. 1997, AJ, 114, 288

Mezger, P. G., Altenhoff, W., Schraml, J., et al. 1967, ApJ, 150, L157

Mezger, P. G., & Henderson, A. P. 1967, ApJ, 147, 471

Molinari, S., Swinyard, B., Bally, J., et al. 2010, A&A, 518, L100

Motogi, K., Hirota, T., Machida, M. N., et al. 2019, ApJ, 877, L25

Motte, F., Bontemps, S., & Louvet, F. 2018, ARA&A, 56, 41

Myers, P. C., & Benson, P. J. 1983, ApJ, 266, 309

Myers, P. C., & Fuller, G. A. 1992, ApJ, 396, 631

Nagakura, T., Hosokawa, T., & Omukai, K. 2009, MNRAS, 399, 2183

Nomura, H., & Millar, T. J. 2004, A&A, 414, 409

Ohama, A., Dawson, J. R., Furukawa, N., et al. 2010, ApJ, 709, 975

Oka, T., Hasegawa, T., Sato, F., et al. 2001, ApJ, 562, 348

Ossenkopf, V., & Henning, T. 1994, A&A, 291, 943

Osterbrock, D. E. 1989, Astrophysics of gaseous nebulae and active galactic nuclei

Palla, F., & Stahler, S. W. 1993, ApJ, 418, 414

Pandian, J. D., Chatterjee, R., Csengeri, T., et al. 2024, ApJ, 966, 54

Park, G., Currie, M. J., Thomas, H. S., et al. 2023, ApJS, 264, 16

Peretto, N., & Fuller, G. A. 2009, A&A, 505, 405

Peters, T., Banerjee, R., Klessen, R. S., et al. 2010, ApJ, 711, 1017

Pillai, T., Wyrowski, F., Carey, S. J., & Menten, K. M. 2006, A&A, 450, 569

Planck Collaboration, Ade, P. A. R., Aghanim, N., et al. 2015, A&A, 576, A104

Poglitsch, A., Waelkens, C., Geis, N., et al. 2010, A&A, 518, L2

Predehl, P., & Schmitt, J. H. M. M. 1995, A&A, 500, 459

Price, S. D., Egan, M. P., Carey, S. J., Mizuno, D. R., & Kuchar, T. A. 2001, AJ, 121, 2819

Priestley, F. D., & Whitworth, A. P. 2021, MNRAS, 506, 775

Purcell, C. R., Hoare, M. G., Cotton, W. D., et al. 2013, ApJS, 205, 1

Quireza, C., Rood, R. T., Bania, T. M., Balser, D. S., & Maciel, W. J. 2006, ApJ, 653, 1226

Rathborne, J. M., Jackson, J. M., & Simon, R. 2006, ApJ, 641, 389

Rieke, G. H., & Lebofsky, M. J. 1985, ApJ, 288, 618

Rieke, G. H., Young, E. T., Engelbracht, C. W., et al. 2004, ApJS, 154, 25

Rosen, A. L., Li, P. S., Zhang, Q., & Burkhart, B. 2019, ApJ, 887, 108

Russeil, D., Schneider, N., Anderson, L. D., et al. 2013, A&A, 554, A42

Ryle, M., & Downes, D. 1967, ApJ, 148, L17

Saha, P., Roy, N., & Bhattacharya, M. 2018, MNRAS, 480, L126

Salaris, M., & Cassisi, S. 2005, Evolution of Stars and Stellar Populations

Salpeter, E. E. 1955, ApJ, 121, 161

Schilke, P. 2015, in EAS Publications Series, Vol. 75-76, EAS Publications Series, 227–235

Schmiedeke, A., Schilke, P., Möller, T., et al. 2016, A&A, 588, A143

Schuller, F., Menten, K. M., Contreras, Y., et al. 2009, A&A, 504, 415

Sewilo, M., Churchwell, E., Kurtz, S., Goss, W. M., & Hofner, P. 2004, ApJ, 605, 285

Shu, F. H. 1977, ApJ, 214, 488

—. 1992, The physics of astrophysics. Volume II: Gas dynamics.

Shu, F. H., Adams, F. C., & Lizano, S. 1987, ARA&A, 25, 23

Shull, J. M. 1980, ApJ, 238, 860

Simon, R., Jackson, J. M., Rathborne, J. M., & Chambers, E. T. 2006, ApJ, 639, 227

Skrutskie, M. F., Cutri, R. M., Stiening, R., et al. 2006, AJ, 131, 1163

Sridharan, T. K., Beuther, H., Schilke, P., Menten, K. M., & Wyrowski, F. 2002, ApJ, 566, 931

Stahler, S. W., & Palla, F. 2004, The Formation of Stars

Stahler, S. W., Palla, F., & Ho, P. T. P. 2000, in Protostars and Planets IV, ed. V. Mannings, A. P. Boss, & S. S. Russell, 327–352

Stark, A. A., & Lee, Y. 2006, ApJ, 641, L113

Stil, J. M., Taylor, A. R., Dickey, J. M., et al. 2006, AJ, 132, 1158

Swarup, G. 1990, Indian Journal of Radio and Space Physics, 19, 493

Takahira, K., Shima, K., Habe, A., & Tasker, E. J. 2018, PASJ, 70, S58

Takahira, K., Tasker, E. J., & Habe, A. 2014, The Astrophysical Journal, 792, 63

Tan, J. C. 2006, Proceedings of the International Astronomical Union, 2, 258–264

Tan, J. C., Beltrán, M. T., Caselli, P., et al. 2014, in Protostars and Planets VI, ed. H. Beuther, R. S. Klessen, C. P. Dullemond, & T. Henning, 149–172

Tan, J. C., Kong, S., Butler, M. J., Caselli, P., & Fontani, F. 2013, ApJ, 779, 96

Tenorio-Tagle, G. 1979, A&A, 71, 59

Tielens, A. G. G. M. 2005, The Physics and Chemistry of the Interstellar Medium

Torii, K., Hasegawa, K., Hattori, Y., et al. 2015, ApJ, 806, 7

Torii, K., Hattori, Y., Hasegawa, K., et al. 2017, ApJ, 835, 142

Urquhart, J. S., Morgan, L. K., Figura, C. C., et al. 2011, MNRAS, 418, 1689

Urquhart, J. S., König, C., Giannetti, A., et al. 2018, MNRAS, 473, 1059

Wang, K., Zhang, Q., Wu, Y., & Zhang, H. 2011, ApJ, 735, 64

Wang, Y., Bihr, S., Rugel, M., et al. 2018, VizieR Online Data Catalog, J/A+A/619/A124

Ward-Thompson, D., Kirk, J. M., André, P., et al. 2010, A&A, 518, L92

Whittet, D. C. B. 1992, Dust in the galactic environment

Williams, J. P., Blitz, L., & McKee, C. F. 2000, in Protostars and Planets IV, ed. V. Mannings, A. P. Boss, & S. S. Russell, 97

Wilson, T. L., Rohlfs, K., & Hüttemeister, S. 2009, 319–328

Wolfire, M. G., & Cassinelli, J. P. 1987, ApJ, 319, 850

Wood, D. O. S., & Churchwell, E. 1989, ApJS, 69, 831

Wood, K., Haffner, L. M., Reynolds, R. J., Mathis, J. S., & Madsen, G. 2005, ApJ, 633, 295

Yang, A. Y., Urquhart, J. S., Thompson, M. A., et al. 2021, A&A, 645, A110

Yang, A. Y., Dzib, S. A., Urquhart, J. S., et al. 2023, A&A, 680, A92

Yorke, H. W. 1986, ARA&A, 24, 49

Yu, N.-P., & Wang, J.-J. 2013, Research in Astronomy and Astrophysics, 13, 28

Zacharias, N., Monet, D. G., Levine, S. E., et al. 2004, in American Astronomical Society Meeting Abstracts, Vol. 205, American Astronomical Society Meeting Abstracts, 48.15

Zhang, C.-P., Yuan, J.-H., Xu, J.-L., et al. 2017, Research in Astronomy and Astrophysics, 17, 057

Zhang, Y., & Tan, J. C. 2015, ApJ, 802, L15

Zinnecker, H., McCaughrean, M. J., Rayner, J. T., Wilking, B. A., & Moneti, A. 1993, Reviews in Modern Astronomy, 6, 191

Zinnecker, H., & Yorke, H. W. 2007, ARA&A, 45, 481

Zweibel, E. G. 2002, ApJ, 567, 962

List of Publications

Refereed Journals

1. Jyotirmoy Dey, Jagadheep D. Pandian, and Dharam Vir Lal, “Gas Dynamics in the Star-forming Region G18.148–0.283: Is It a Manifestation of Two Colliding Molecular Clouds?", 2022, The Astrophysical Journal, 925, 60

2. Jyotirmoy Dey, Jagadheep D. Pandian, and 10 co-authors, “A multi-wavelength study of Galactic H II regions with extended emission", 2024, Astronomy & Astrophysics, 689, A254

Refereed Conferences

1. Jyotirmoy Dey, Jagadheep D. Pandian, and 9 co-authors, “A Study of Ultra- compact H II Regions with Extended Emission: their Importance, Origin, and Evolution", 2024, Bull. Soc. R. Sci. Liège, 93(2), 572–581

Appendix A

Estimating the electron temperature

We derive the electron temperature under the local thermodynamic equilibrium (LTE) conditions. Under LTE and Rayleigh-Jeans limit, the observed specific intensity takes the following form

$$I_{cont}(\nu) = \frac{2\,k_B\,T_e\,\nu^2}{c^2}\,\left(1 - e^{\tau_{cont}(\nu)}\right), \tag{A.1}$$

where ν is the frequency, k_B is the Boltzmann constant, T_e is the electron temperature, and $\tau_{cont}(\nu)$ is the optical depth of the medium for continuum emission. Rearranging the terms, equ. A.1 can also be written as

$$\tau_{cont}(\nu) = -\ln\left(1 - \frac{c^2\,I_{cont}(\nu)}{2\,k_B\,T_e\,\nu^2}\right), \tag{A.2}$$

Now, from the definition of brightness temperature, the continuum temperature (T_{cont}) can be estimated as

$$T_{cont} = \frac{c^2\,I_{cont}(\nu)}{2\,k_B\,\nu^2}. \tag{A.3}$$

Similarly, the brightness temperature of the spectral line (T_{line}) is

$$T_{line} = \frac{c^2\,I_{line}(\nu)}{2\,k_B\,\nu^2} \tag{A.4}$$

for any given pixel in the image. Thus, the line-to-continuum intensity ratio in a single pixel is

$$\frac{I_{line}(\nu)}{I_{cont}(\nu)} = \frac{I(\nu) - I_{cont}(\nu)}{I_{cont}(\nu)} = \frac{I(\nu)}{I_{cont}(\nu)} - 1, \tag{A.5}$$

where $I(\nu)$ is the total intensity. Now, we can rewrite equ. A.5 in terms of T_{cont}, T_{line}, $\tau_{cont}(\nu)$ and $\tau_{line}(\nu)$ as follows:

$$\frac{T_{line}}{T_{cont}} = \frac{e^{-\tau_{cont}(\nu)}\left[1 - e^{-\tau_{line}(\nu)}\right]}{\left[1 - e^{-\tau_{cont}(\nu)}\right]}. \tag{A.6}$$

From equ. A.6, $\tau_{line}(\nu)$ can be expressed as

$$\tau_{line}(\nu) = -\ln\left(1 - \frac{T_{line}}{T_{cont}}\, e^{\tau_{cont}(\nu)}\, \left[1 - e^{-\tau_{cont}(\nu)}\right]\right). \tag{A.7}$$

Using equ. A.2 and equ. A.7, one can determine $\tau_{cont}(\nu)$ and $\tau_{line}(\nu)$ for each pixel. The value of $\tau_{cont}(\nu)$ along a line of sight (LOS) can also be related to the properties of the H II region using the Altenhoff approximation (Altenhoff, 1961):

$$\tau_{cont}(\nu) \approx 8.235 \times 10^{-2} \left(\frac{T_e}{\mathrm{K}}\right)^{-1.35} \left(\frac{\nu}{\mathrm{GHz}}\right)^{-2.1} \left(\frac{EM}{\mathrm{pc.cm^{-6}}}\right), \tag{A.8}$$

where EM is the emission measure. Similarly, following Wilson et al. (2009), the line optical depth is

$$\tau_{line}(\nu) \approx 1.92 \times 10^{3} \left(\frac{T_e}{\mathrm{K}}\right)^{-2.5} \left(\frac{\Delta\nu}{\mathrm{KHz}}\right)^{-1} \left(\frac{EM}{\mathrm{pc.cm^{-6}}}\right) \tag{A.9}$$

for the recombination lines in the radio frequency domain. Here $\Delta\nu$ is the FWHM of the RRLs in KHz. Following equ. A.8 and equ. A.9 we get

$$\frac{\tau_{line}(\nu)}{\tau_{cont}(\nu)} = 23.315 \times 10^{3} \left(\frac{T_e}{\mathrm{K}}\right)^{-1.15} \left(\frac{\Delta\nu}{\mathrm{KHz}}\right)^{-1} \left(\frac{\nu}{\mathrm{GHz}}\right)^{2.1}. \tag{A.10}$$

Since the optical depth of the line and continuum are measured from the data, we can use equ. A.10 to estimate pixel-to-pixel T_e values for the entire region under the LTE conditions. It is to be noted that equ. A.2 is not completely independent. We have to provide a T_e to derive a $\tau_{cont}(\nu)$ value. When the continuum is optically thin, the continuum optical depth is inversely proportional to T_e, and one can use equ. A.6 and A.10 to derive T_e. However, since the relation between the continuum optical depth and T_e is non-linear for moderate optical depth, we adopt an iterative procedure, wherein an initial guess of the electron temperature is provided in equ. A.2 following which the electron temperature is re-computed using equ. A.10. This is repeated until the value of electron temperature converges.

Goldberg (1966) showed that the intensities of the observed RRLs could only be ex-

plained using departures from LTE, similar to the anomalous intensities of optical lines from nebulae and stellar atmospheres. Following Goldberg (1966), the excitation temperature (T_{ex}) of an electronic transition is not equal to the T_e of the ionized gas inside a H II region, and is thus corrected using

$$e^{-h\nu/k_BT_{ex}} = \frac{b_n}{b_{n-1}}\ e^{-h\nu/k_BT_e}, \tag{A.11}$$

where b_n, the departure coefficient, is the ratio of the actual population of atoms in the n-th state to the population that would be there if the ionized gas was in the LTE at the temperature T_e. Under the condition $h\nu \ll k_BT_e$, the corrected or non-LTE value of the line absorption coefficient (κ_{line}) for the line n $\rightarrow$ n–1 is found to be (Goldberg, 1966; Brocklehurst & Seaton, 1972):

$$\kappa_{line} = \kappa^*_{line}\, b_{n-1}\, \beta, \tag{A.12}$$

where κ^*_{line} is the LTE value of the line absorption coefficient, and the correction factor (β) is approximated by Brocklehurst & Seaton (1972) for RRL transitions with $\Delta n \approx 1$. If the values of $|\tau_{line}|$ and τ_{cont} are less than 1, we can approximate the exponential terms in equ. A.6 to the second order to get

$$T_{line} \approx T^*_{line}\, b_n \left(1 - \frac{\tau_{cont}}{2}\beta\right), \tag{A.13}$$

under the condition $h\nu \ll k_BT_e$. Again, T^*_{line} is the LTE value of the line temperature. Now, using the non-LTE value, i.e., T_{line} in equ. A.7 and following equ. A.10, we can get the non-LTE electron temperature of the ionized gas.

Appendix B

Figures

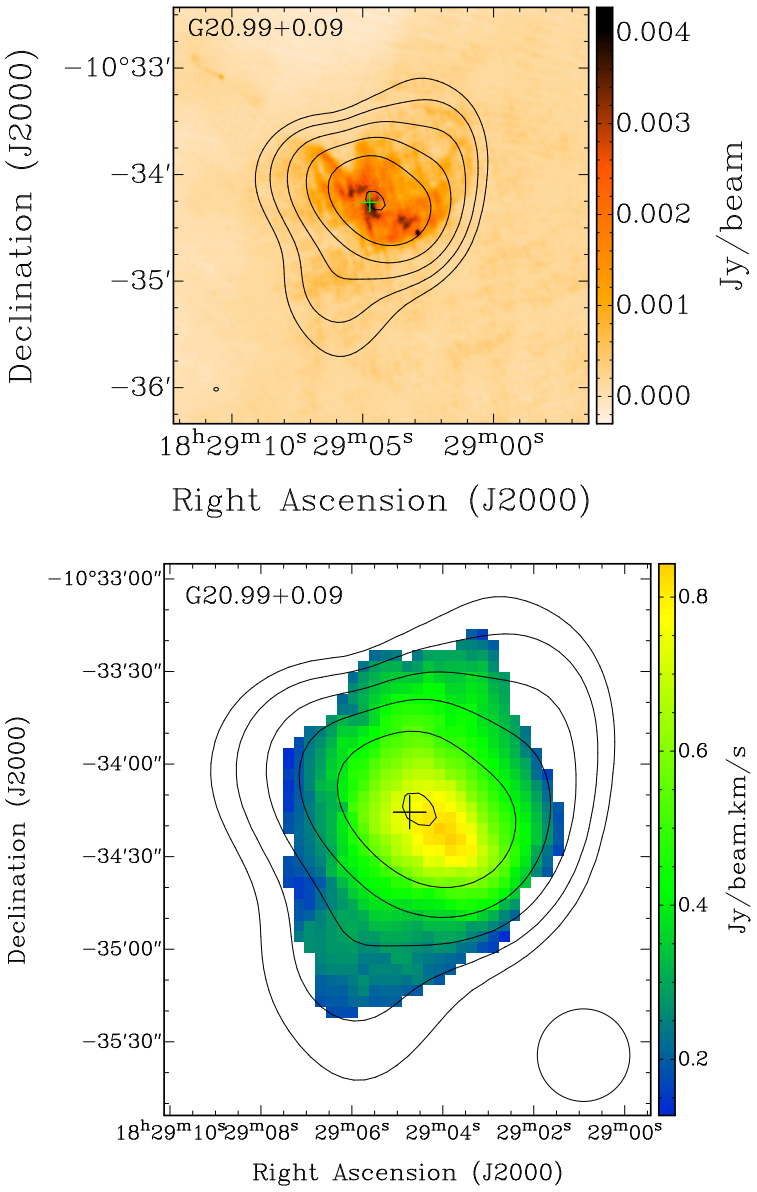

Figure B.1: uGMRT radio continuum (top) and GLOSTAR-D moment-0 (bottom) maps of individual H II regions overlaid with the radio contours from the GLOSTAR-D continuum maps in black. The contours have started at the 3σ-level flux and have increased in steps of $\sqrt{3}$. The coordinates reported in the THOR radio continuum catalog are shown using the green/black '+' signs, while the locations of the UC cores (from the GLOSTAR-B and CORNISH surveys) are shown using the blue '$*$' signs. The respective beam sizes are shown at the bottom-left/bottom-right corners of the figures.

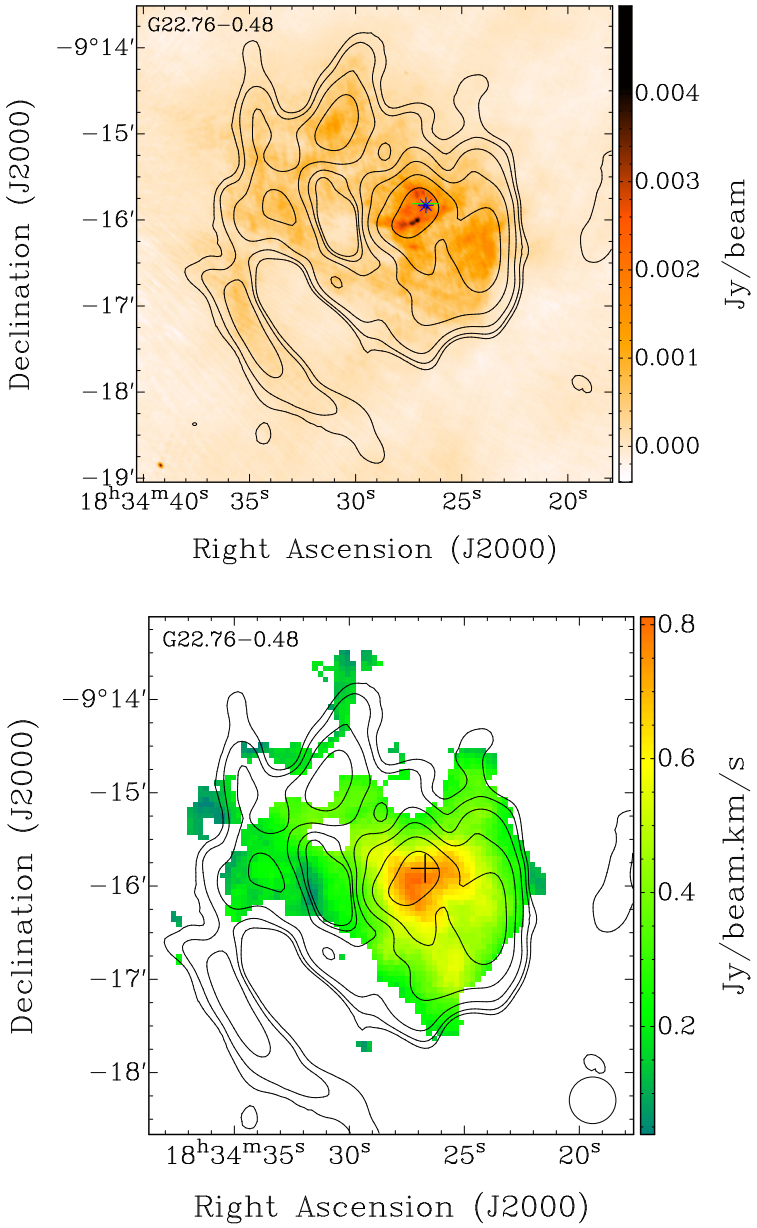

Figure B.1: Same as before, but the contours have started at the 3σ-level flux and have increased in steps of 2.

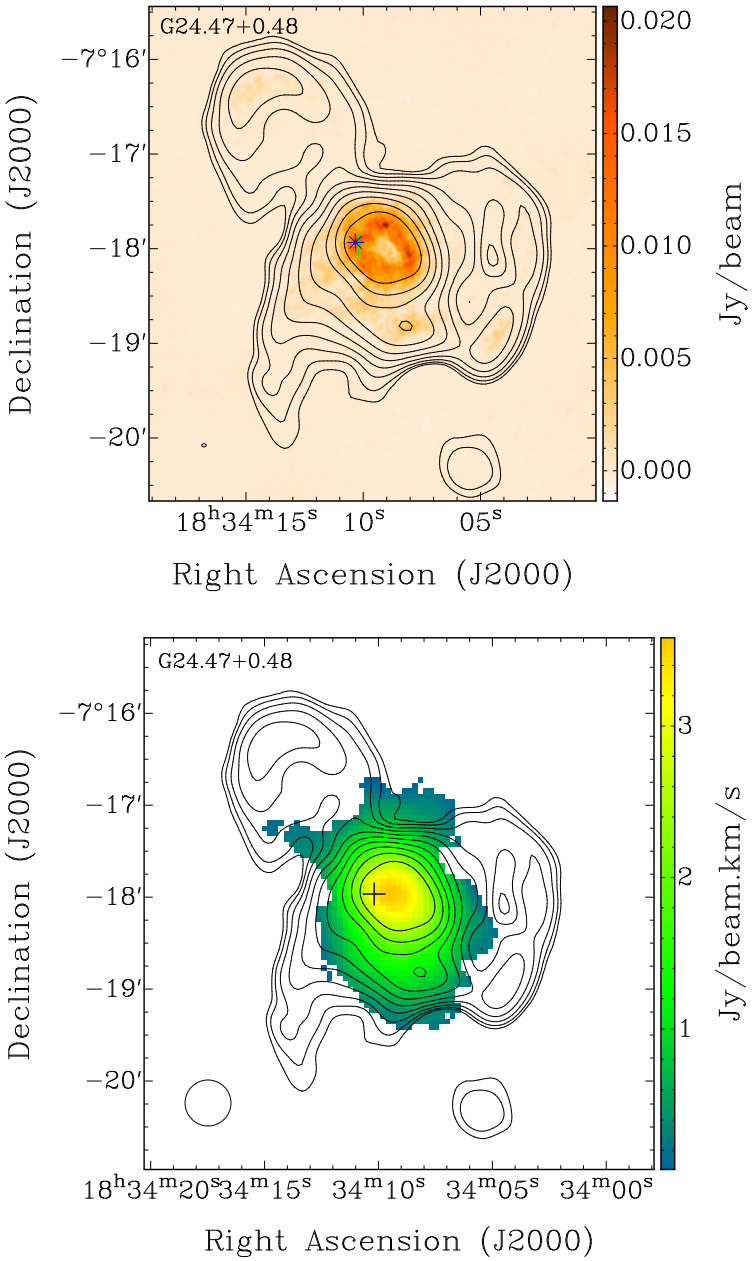

Figure B.1: Same as before, but the contours have started at the 3σ-level flux and have increased in steps of and $\sqrt{3}$.

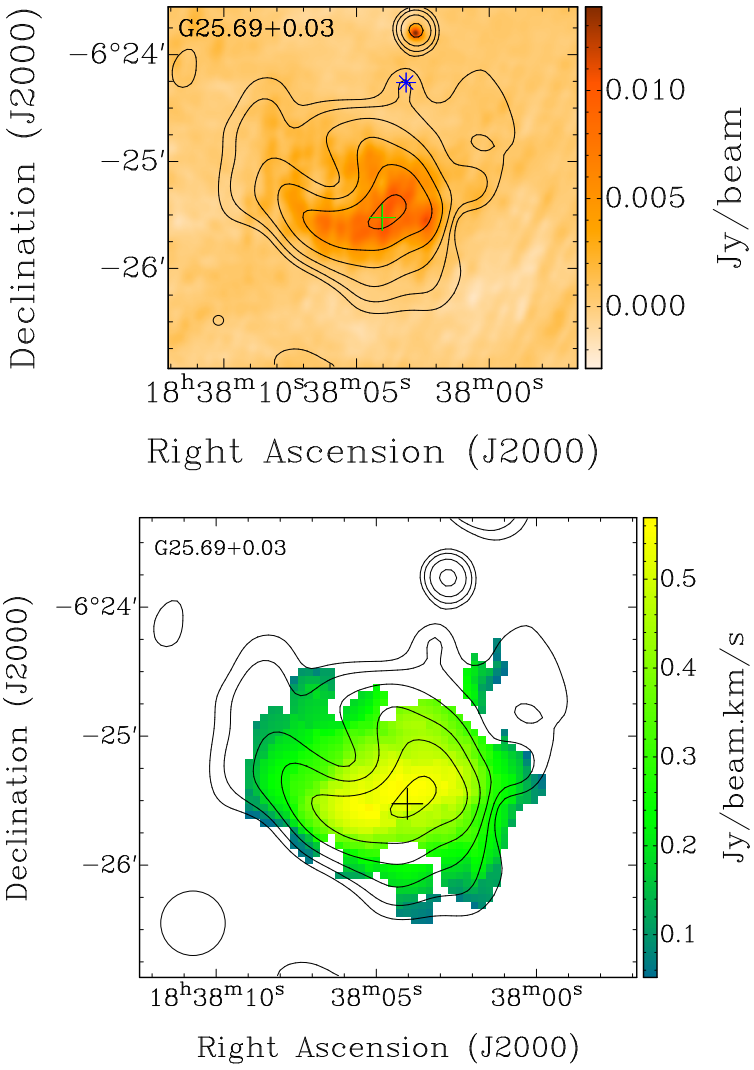

Figure B.1: Same as before, but the contours have started at the 3σ-level flux and have increased in steps of $\sqrt{3}$.

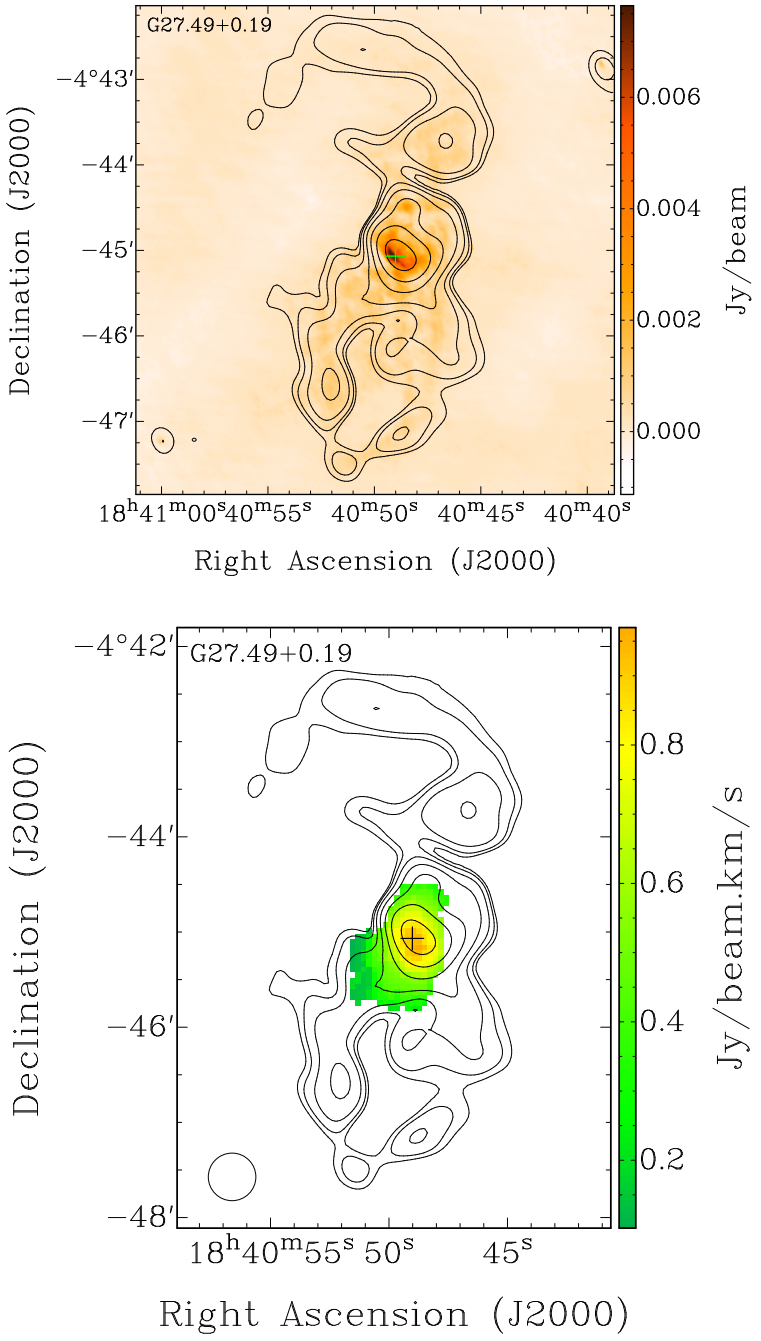

Figure B.1: Same as before, but the contours have started at the 3σ-level flux and have increased in steps of 2.

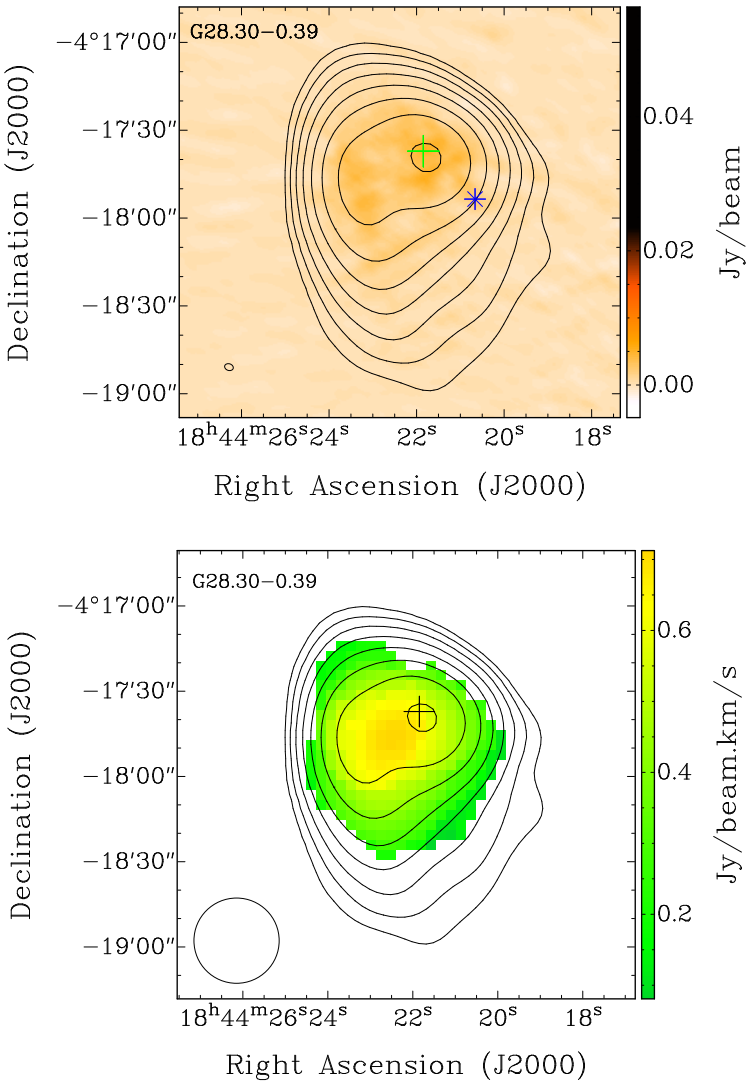

Figure B.1: Same as before, but the contours have started at the 3σ-level flux and have increased in steps of $\sqrt{3}$.

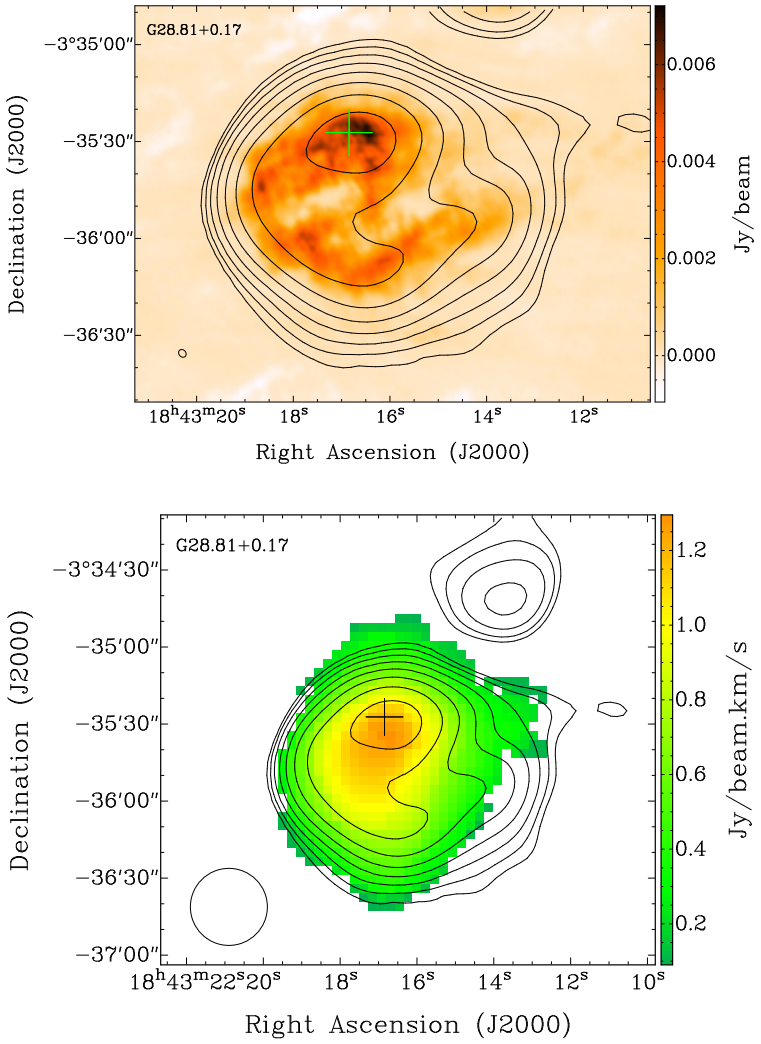

Figure B.1: Same as before but the contours have started at the 3σ-level flux and have increased in steps of $\sqrt{3}$.

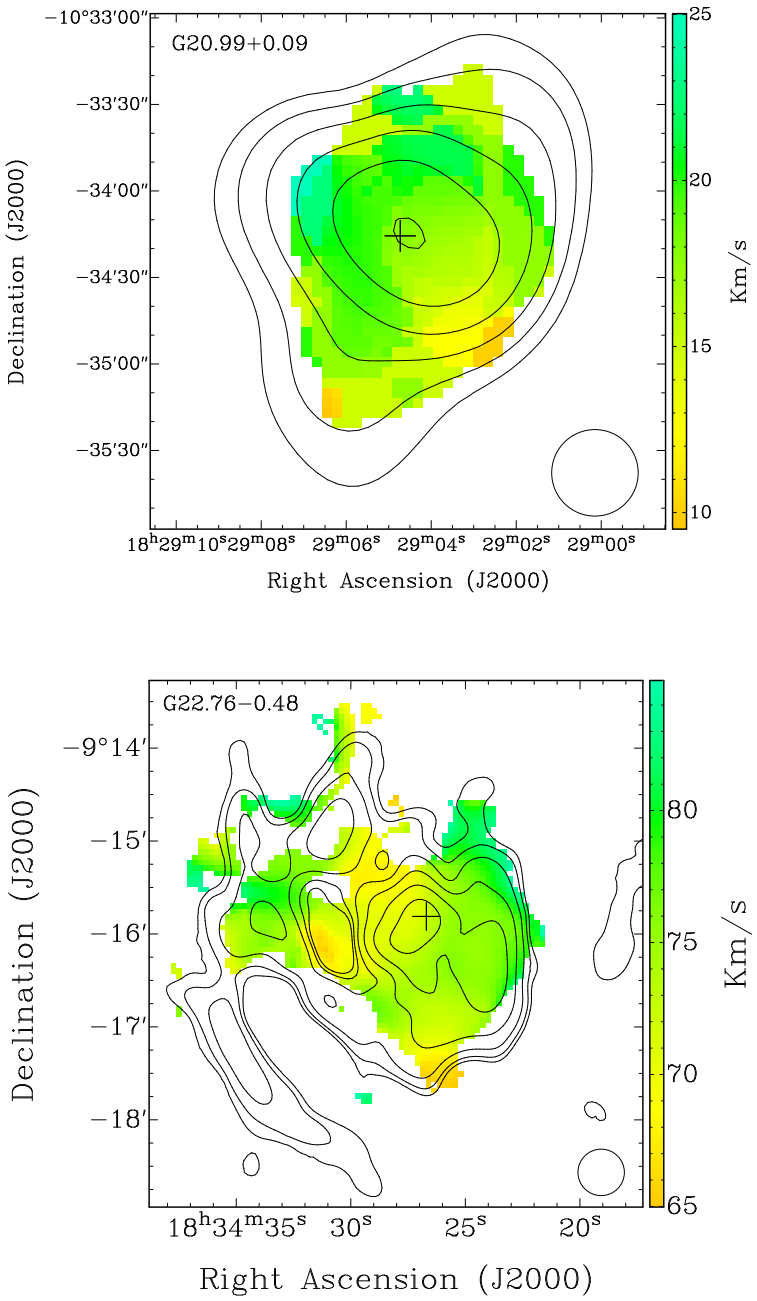

Figure B.2: RRL peak velocity distribution maps from the GLOSTAR-D data overlaid with the GLOSTAR-D radio continuum contours in black. Starting from the 3σ-level, the radio contours increase in the multiplicative steps of $\sqrt{3}$ (top) and 2 (bottom), respectively. The coordinates reported in the THOR radio continuum catalog are shown using black '+' signs, and the respective beam sizes are shown at the bottom-left/bottom-right corner of the figures.

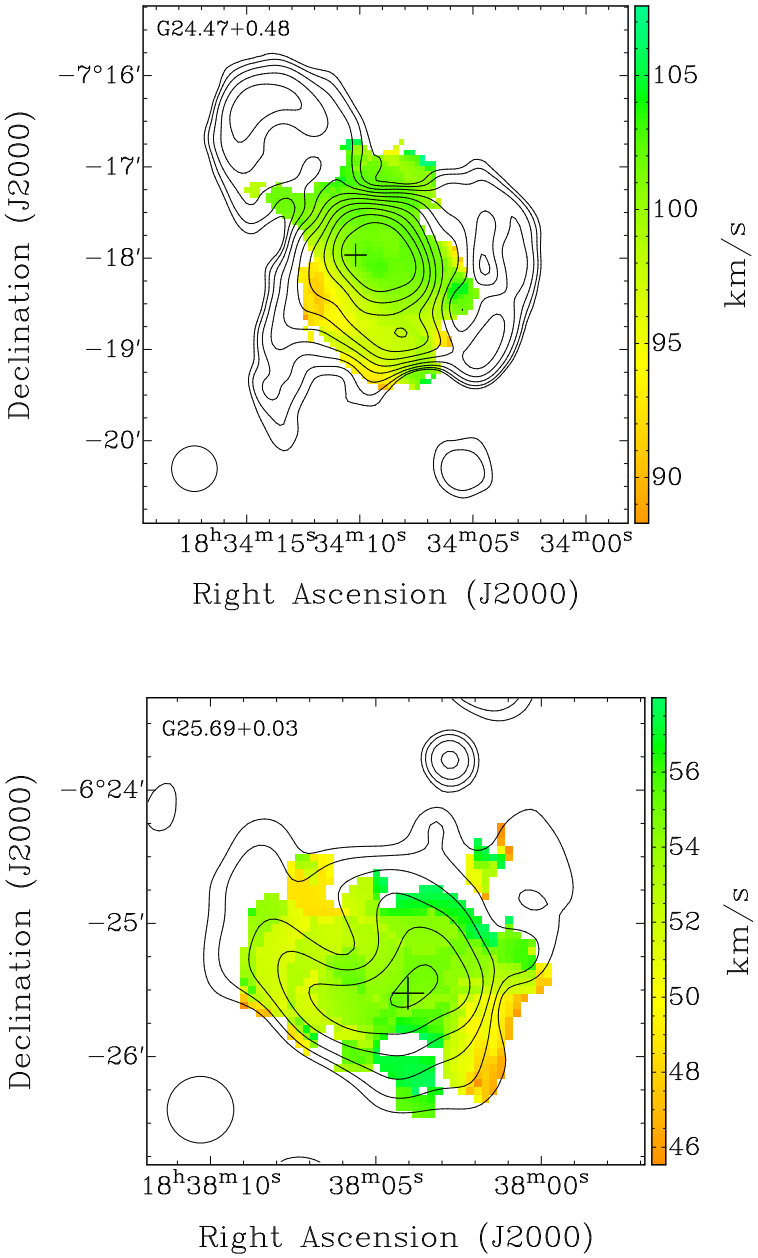

Figure B.2: Same as before, but the radio contours have started at the 3σ-level flux and have increased in steps of $\sqrt{3}$ (top) and $\sqrt{3}$ (bottom), respectively

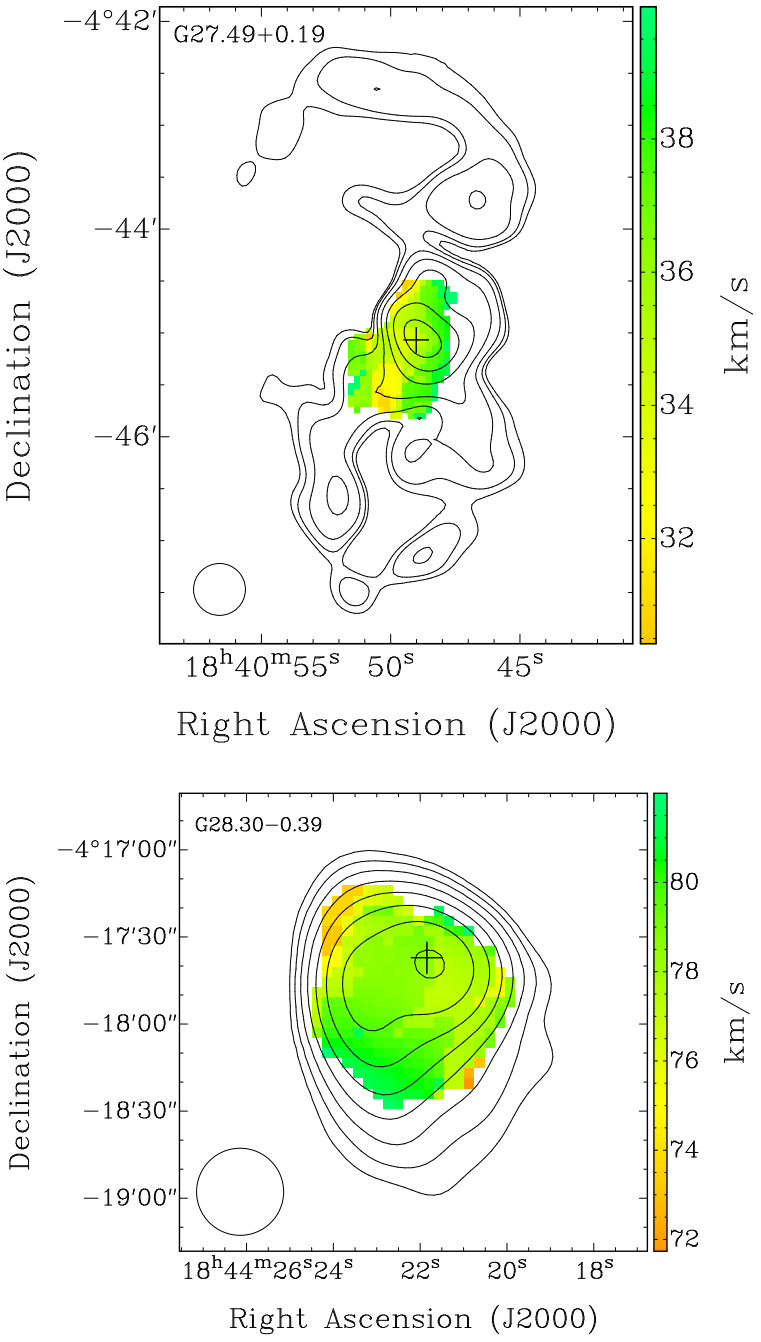

Figure B.2: Same as before, but the radio contours have started at the 3σ-level flux and have increased in steps of 2 (top) and $\sqrt{3}$ (bottom), respectively.

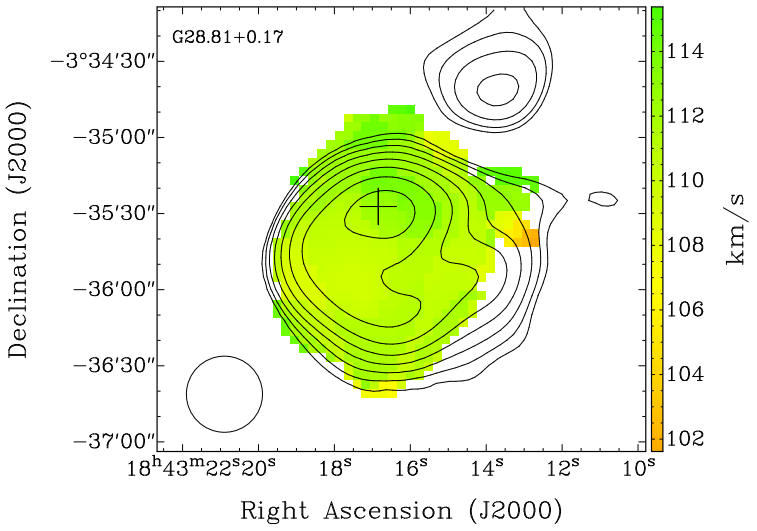

Figure B.2: Same as before, but the radio contours have started at the 3σ-level flux and have increased in steps of $\sqrt{3}$.

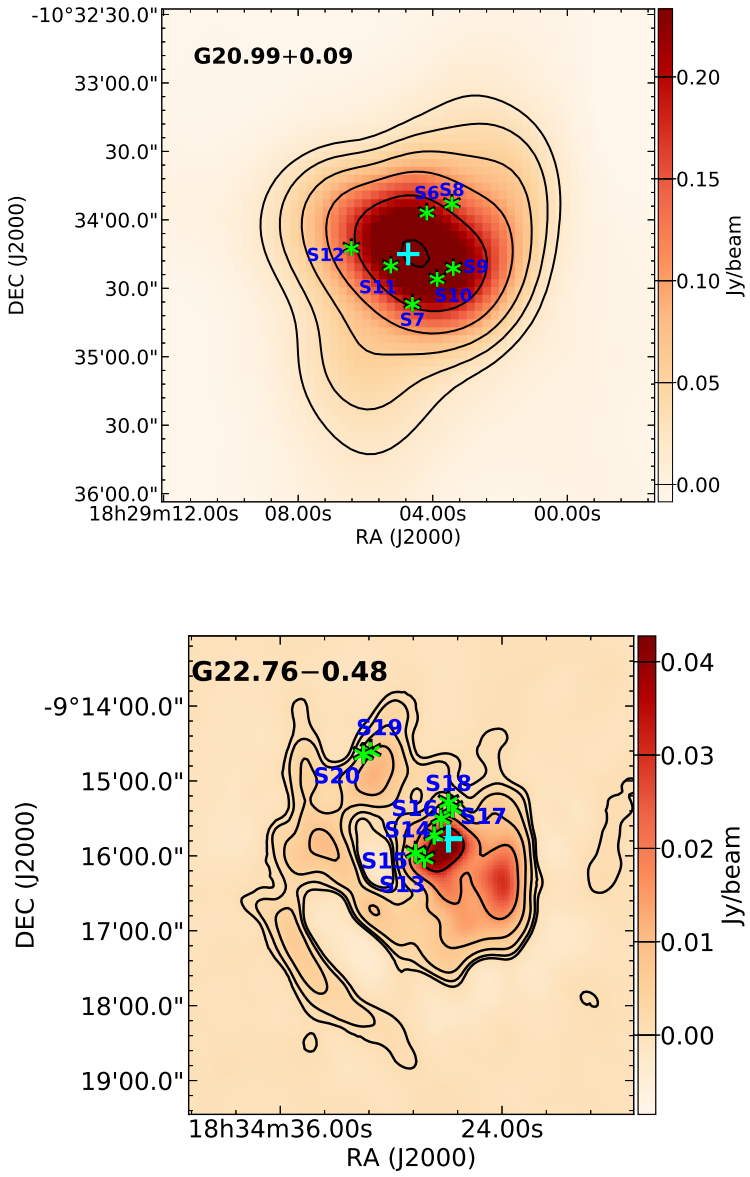

Figure B.3: Locations of the candidate ionizing stars (labeled using an S__ format) are shown using green '*' signs for the individual H II regions (see Table 6.4 for details). The cyan '+' signs indicate the coordinates reported in the THOR radio continuum catalog.

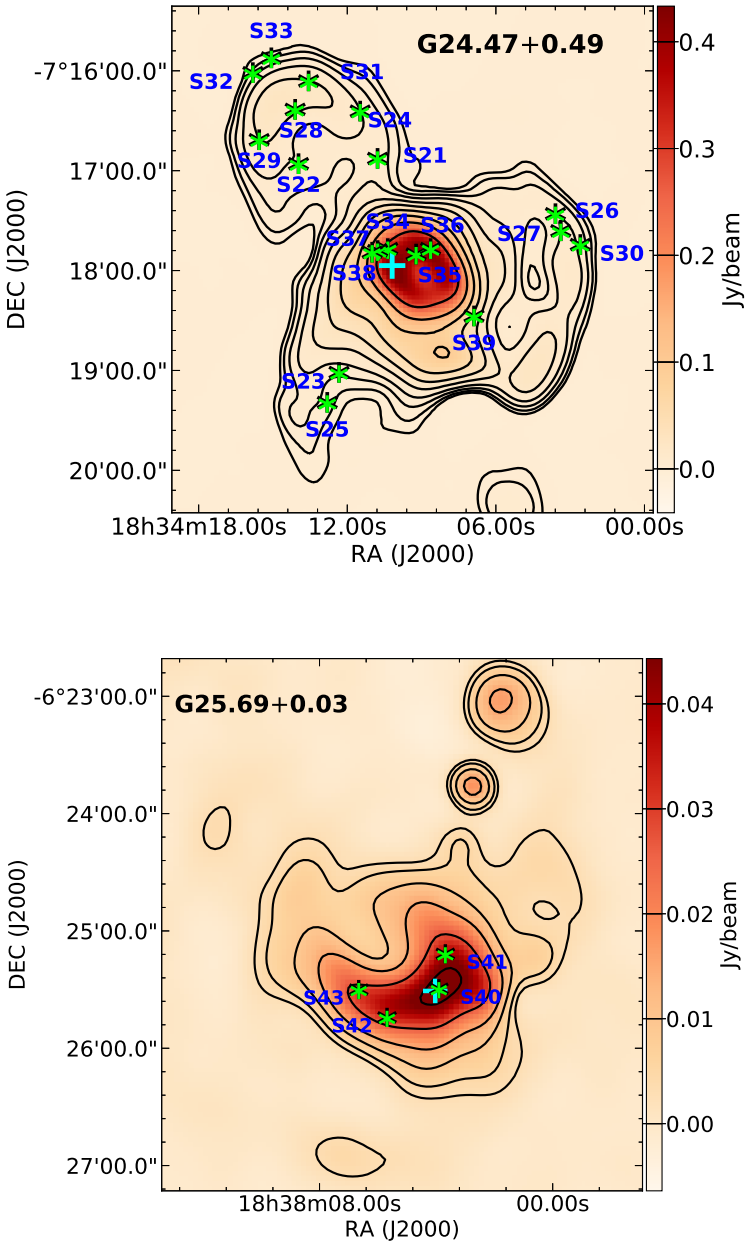

Figure B.3: Continued

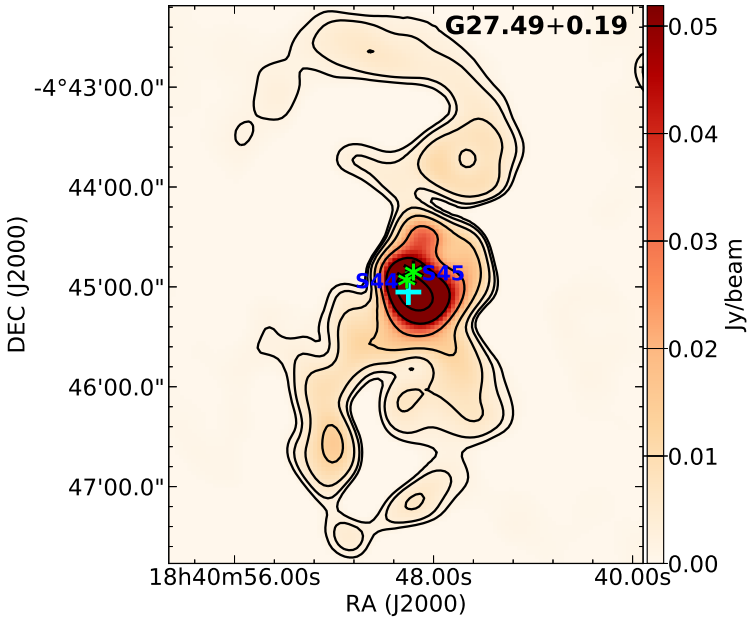

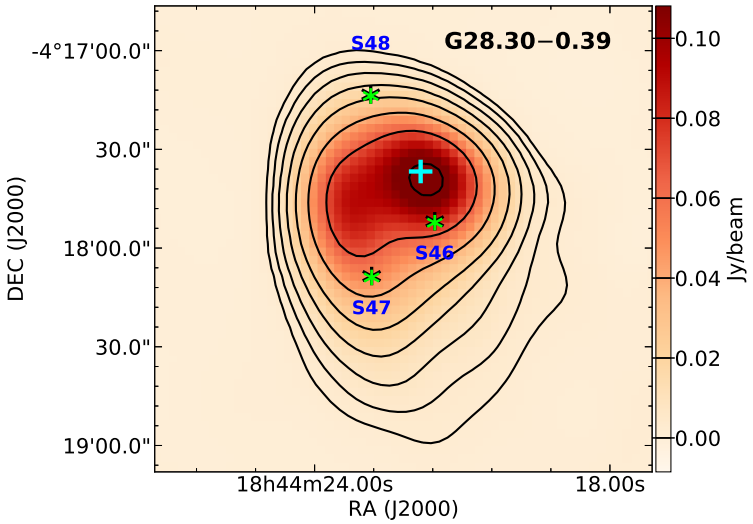

Figure B.3: Continued

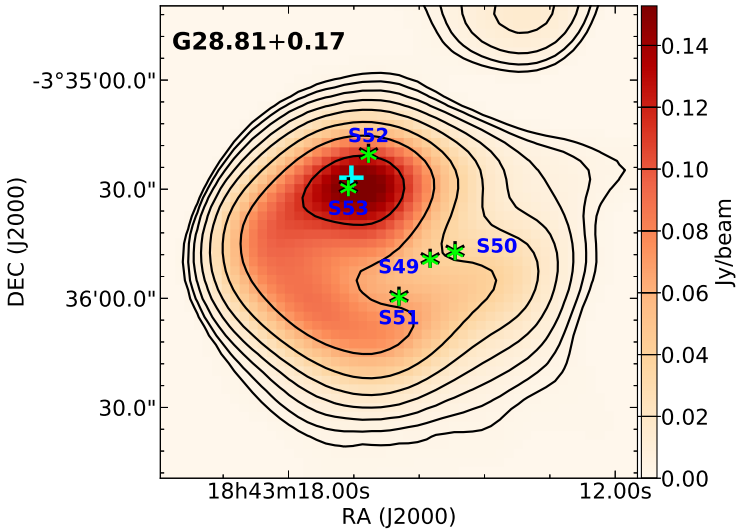

Figure B.3: Continued

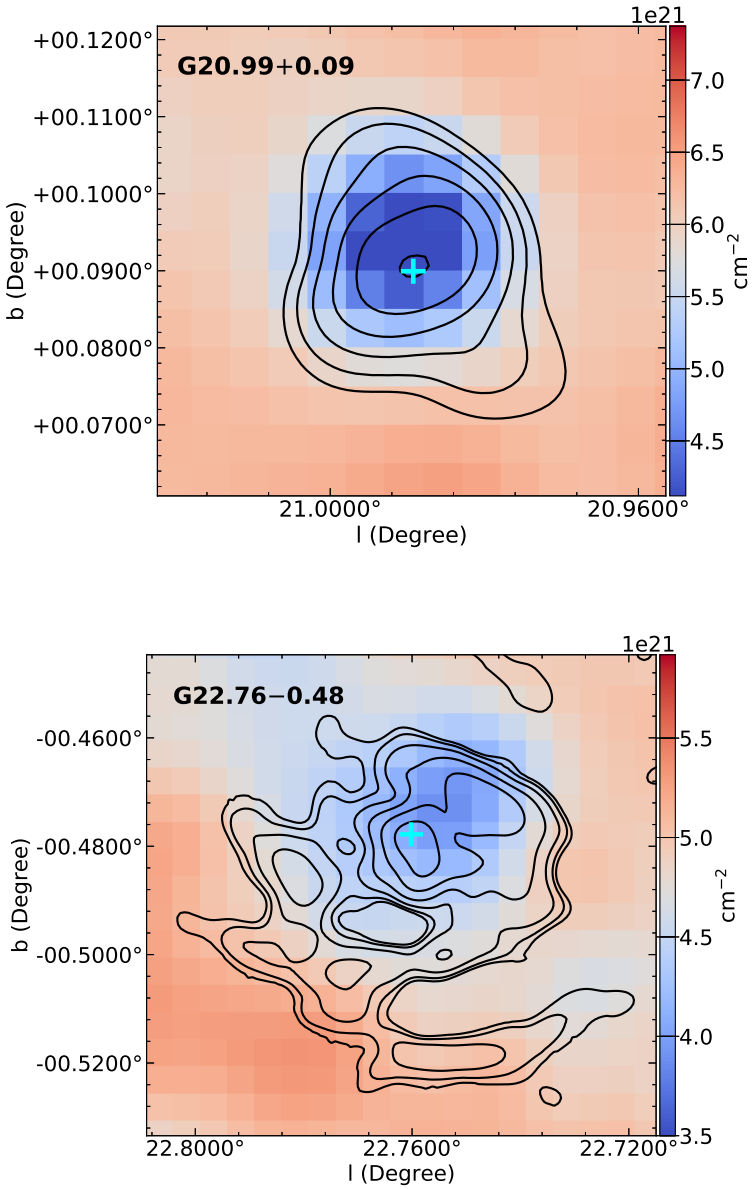

Figure B.4: H I column density maps generated using the VGPS data overlaid with the GLOSTAR-D radio continuum contours in black. Starting from the 3σ-level, the radio contours increase in the multiplicative steps of $\sqrt{3}$ (top) and 2 (bottom), respectively. The coordinates reported in the THOR radio continuum catalog are shown using cyan '+' signs.

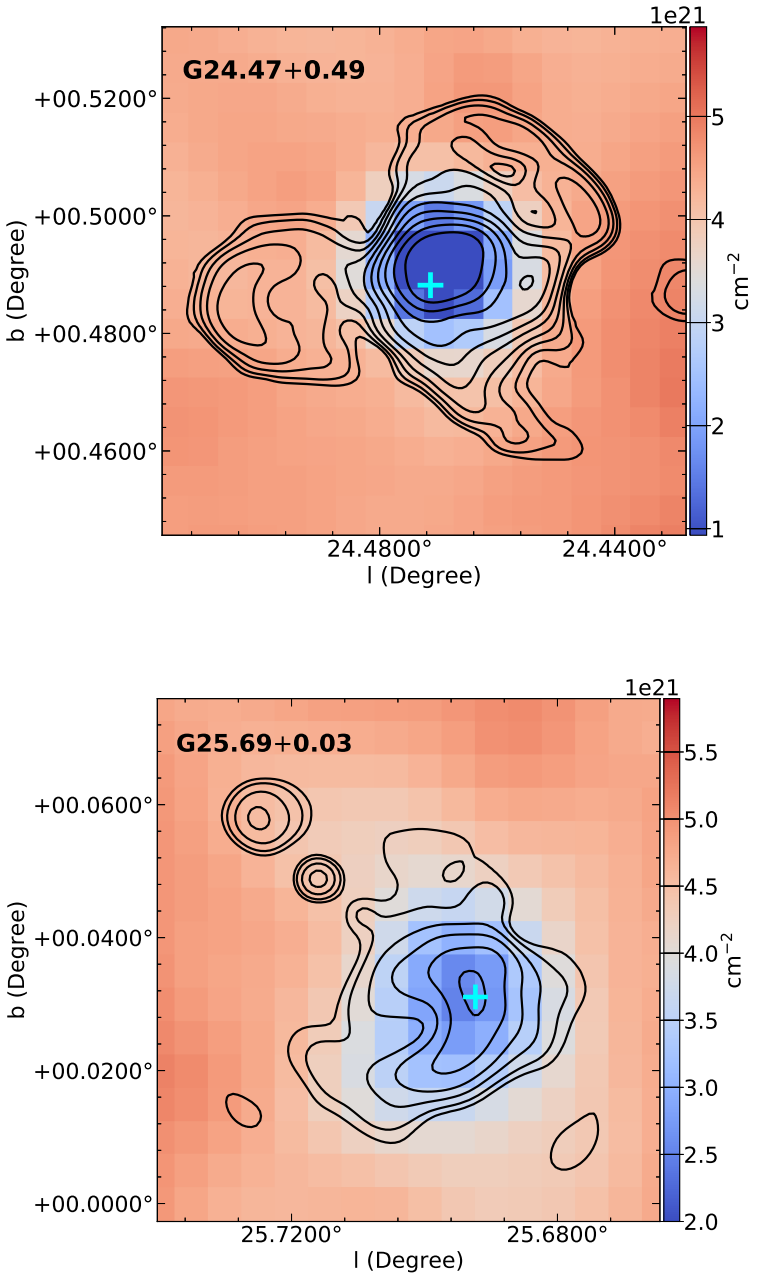

Figure B.4: Same as before, but the radio contours have started at the 3σ-level flux and have increased in steps of $\sqrt{3}$ (top) and $\sqrt{3}$ (bottom), respectively

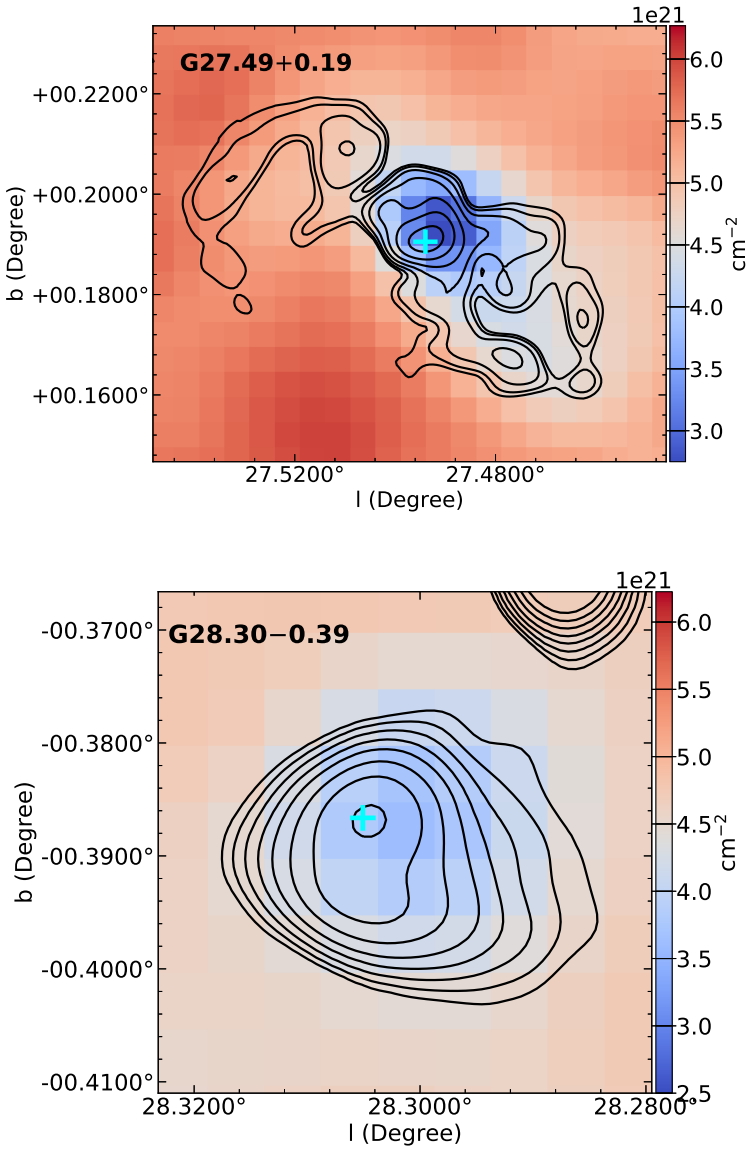

Figure B.4: Same as before, but the radio contours have started at the 3σ-level flux and have increased in steps of 2 (top) and $\sqrt{3}$ (bottom), respectively.

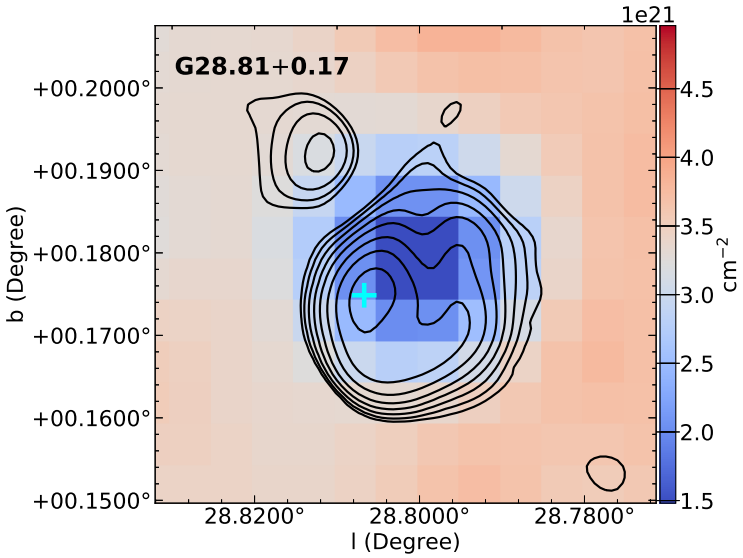

Figure B.4: Same as before, but the radio contours have started at the 3σ-level flux and have increased in steps of $\sqrt{3}$.